SVC

Heuréka!
Post-Deadline Recent Developments Session

SOCIETY of VACUUM COATERS

Electromechanics of a Highly Flexible Transparent Conductor for Display Applications

J. Lewis, S. Grego, B. Chalamala, E. Vick, and D. Temple,
MCNC Research and Development Institute, Research Triangle Park, NC

Key Words: OLEDs, Polymer substrates, Transparent/conductive coatings, Flexible displays

ABSTRACT

Multilayer ITO-Ag-ITO (IMI) stacks on polymer substrates were evaluated as transparent conductors for flexible organic light-emitting diode (OLED) displays. The IMI samples exhibited significantly reduced sheet resistance over ITO and slightly improved optical transmission. In addition, the IMI structures showed dramatically improved mechanical properties when subjected to bending both as a function of radius of curvature as well as number of cycles to a fixed radius. Organic light emitting devices fabricated on IMI anodes showed improved performance compared with those made on ITO anodes at current densities greater than 1 mA/cm^2 due to the improved conductivity of the anode.

INTRODUCTION

Indium tin oxide (ITO) is the most commonly used electrode material in flat panel displays as it provides good electrical conductivity and high transparency in the visible region. Moreover, for flat panel displays based on organic light emitting diodes (OLEDs), ITO is the preferred anode material as it provides good energy level alignment for the efficient injection of holes into the organic layers [1-3]. However, with the increasing interest in the development of displays on flexible substrates, there is a great need for a more mechanically robust flexible transparent conductor as ITO interconnects fail under lower mechanical strain than the other device layers [4,5]. Alternatives to ITO include conductive polymers and carbon nanotube composites [6,7]. While both conductive polymers and polymer composites have been shown to be mechanically robust, the combination of sufficient conductivity and optical transmission required for displays has been difficult to achieve.

Another alternative to a simple ITO film for transparent conductors is the use of dielectric-metal-dielectric (DMD) multilayers, also known as IMI when ITO is used instead of dielectric cladding layers. These structures are typically composed of a thin silver layer (~10-15 nm) sandwiched between two high dielectric constant layers (~30-50 nm). In addition to ITO, DMD structures have been demonstrated with such materials as TiO_2, ZnO, and ZnS as the high index cladding [8-14]. When designed properly, the high index of refraction contrast between Ag and the dielectric layers results in efficient constructive interference and visible transparency greater than 90% can be achieved [10,11]. While these structures have been investigated in detail for applications in heat mirrors, low-e window coatings, windshields, EMI shielding [12-17], and have been suggested for improved conductivity electrodes for displays [11, 18-21], their utility as mechanically robust transparent conductive electrodes for flexible displays has not been reported.

In addition to improved electrical conductivity, IMI structures offer several advantages over ITO. As high temperature annealing is not required to achieve good electrical conductivity, the process is better suited for deposition on low temperature polymer substrates. In addition, with ITO as the surface layer, IMI electrodes offer full compatibility with existing OLED architectures. In this paper we report on the improved performance of IMI over ITO with regard to conductivity and transparency, and show that the addition of the ductile silver layer makes the structure mechanically more robust. In addition, we report that OLEDs utilizing IMI anodes showed significantly improved performance, especially at high current densities.

EXPERIMENT PROCEDURE

IMI structures were fabricated on both Corning 1737 glass and 100 μm thick Melinex® PET substrates. Top and bottom ITO films were RF magnetron sputter deposited under identical conditions from a 3" target (90% SnO_2/10% In_2O_3) at a rate of 0.2 nm/sec. Sputter conditions were optimized to provide sufficient conductivity for OLED devices on PET (<100 (Ω/sq) without the need for substrate heating, while maintaining reasonable transparency. Sputter deposition was performed with an RF power of 50W, pressure of 8 mTorr, and gas flow rates of 0.1 sccm O_2 and 99.9 sccm Ar. Ag films were deposited by electron beam evaporation at room temperature, again at a deposition rate of 0.2 nm/sec. ITO film thickness was calibrated using spectroscopic ellipsometry and Ag film thickness was monitored during deposition with a quartz crystal microbalance and calibrated using a stylus profilometer. All films were deposited sequentially without breaking vacuum. IMI samples were fabricated using 35 nm ITO for

 505/856-7188 ISSN 0737-5921

47th Annual Technical Conference Proceedings (April 24–29, 2004) Dallas, TX USA

each layer with the Ag layer sandwiched in between. The effect of Ag layer thickness on optical, electrical, and mechanical performance was studied using film thicknesses of 0, 4, 8, 12, and 15 nm.

Transmission spectra were measured using a Perkin Elmer Lambda 900 spectrometer and sheet resistance was measured using a commercial four-point probe meter. The morphology of Ag layer was measured by depositing 35 nm ITO films followed by Ag films of varying thickness. The two-layer structures were imaged using atomic force microscopy without deposition of the second ITO layer.

Measurements of the effect of bending were made by clamping the sample in a semicircle between two parallel plates. One plate was fixed to a rigid support, while the other plate was mounted to the drive shaft of a stepper motor. Samples of 50 mm length and 5 mm width were clamped between the two plates with the conductor on the outside at an initial radius of 14 mm. In this configuration, the conductive films are under tensile stress. The bending radius was approximated as half the distance between the plates. Electrical contact was made by the clamps and resistance was monitored with a multimeter. For fatigue tests, the distance between the parallel plates cycled between 28 mm and 12 mm, at a rate of 10 mm/s.

To demonstrate the effect of improved electrical performance of IMI electrodes, OLED devices with ITO and IMI anodes were fabricated on glass substrates. The ITO anode was 100 nm thick, while the IMI layer thicknesses were 35/8/35 nm (ITO/Ag/ITO). Both anodes were O_2 plasma treated prior to organic deposition, and all other device layers were deposited simultaneously for both samples. The organic materials were used as received from Eastman Kodak Company. The device layers consisted of 15 nm CuPc (copper phthalocyanine) as the hole injection layer, 40 nm NPB (N,N'-Bis(naphthalen-1-yl)-N,N'-bis(phenyl)benzidine) as the hole transport layer, and 60 nm Alq_3 (tris-(8-hydroxyquinoline) aluminum) as the electron transport/emission layer, and 0.8 nm LiF and 100 nm Al as the cathode. Devices were encapsulated in a N_2 ambient before electro-optical characterization. Current voltage measurements were performed using a Keithley 2400 SourceMeter and brightness voltage measurements were performed using a calibrated Si photodiode.

RESULTS AND DISCUSSION

Luminous transmission, T_{lum}, as a function of Ag film thickness is shown in Figure 1. T_{lum} provides a good figure of merit for display applications as it is a weighted average of the transmission by the photopic response in the 360-830 nm range [9]. ITO films on PET without an Ag layer showed T_{lum} of 74.9%, whereas IMI structures with Ag layers showed T_{lum} values between 66.1 and 77.5%. The highest T_{lum} values were obtained for Ag films with thickness in the 8-12 nm range. It is worth noting that while the transmission of the ITO in this work was not as high as can be achieved, transmission spectra for IMI multi layers were calculated from the optical constants of the films using WVase32 software from J.A. Woollam. These calculations predicted higher transmission for optimized IMI structures over ITO if the same ITO parameters were used in both structures, whether for highly transparent ITO or the less transparent ITO used in this work.

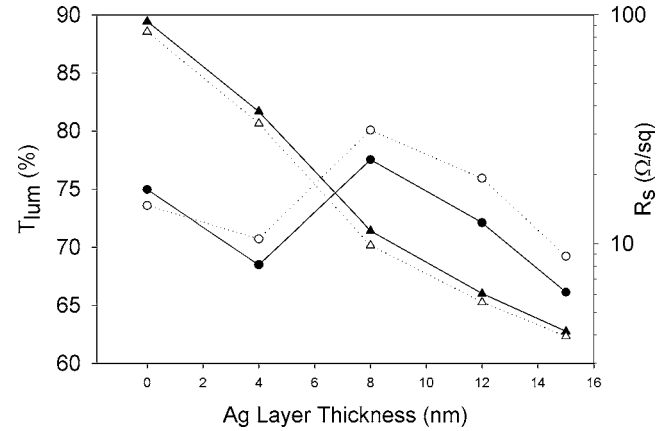

Figure 1: T_{lum} (circles) and R_s (triangles) data as a functions of Ag layer thickness for IMI structures on glass (closed markers) and PET (open markers) substrates.

With the addition of an Ag layer to the structure significant improvement in conductivity was anticipated. Sheet resistance data are shown as a function of Ag layer thickness in Figure 1. Compared to ITO films, IMI samples showed improved electrical conductivity. For example, with a 12 nm Ag film in the IMI on a PET substrate, electrical conductivity improved by over 15 times. Even for Ag films of 4 nm and 8 nm, where the film consists of lightly interconnected islands (as discussed later), significant improvement in the electrical conductivity was obtained.

Experiments to determine the effect of bending on the films were performed as a function of radius and number of cycles. We defined a 10% increase in resistance as the onset of failure, R_{10}, and the results are summarized as a function of Ag layer thickness in Table 1. As a function of curvature, the IMI samples with at least 8 nm Ag showed improved performance, with the onset of increased resistance occurring at a smaller radius of curvature. Qualitatively, it was observed that the IMI samples provided improved measurement yield from reduced damage by sample handling.

Table 1: Performance of IMI structures with different Ag thickness vs. ITO under of bending.

Ag Layer thickness (nm)	R_{10} (Std. dev.)	R/R_0 (100 cycles @ 6mm)	R/R_0 (10,000 cycles @ 6mm)
0	6.4 (0.2)	5.85	7.41
4	7.2 (0.4)	1.94	11
8	5.0 (0.5)	1.04	1.28
12	5.4 (0.2)	1.01	1.16
15	5.7 (0.2)	1.09	1.17

While bending results as a function of radius showed marked improvement, the performance of IMI structures under repeated bending showed much more dramatic improvement over ITO. The resistance data for samples bent to a radius of 6 mm as a function of the number of cycles are shown in Figure 2. The data shown for each sample type were the best achieved in our experiments. The increase in resistance after 100 and 10,000 cycles for each sample is given in Table 1. Again all samples with at least 8 nm Ag showed dramatic improvement in cycling performance. That dramatic improvement was shown for Ag layers thicknesses between 8 and 12 nm is an indication that high precision in the deposition process is not necessary.

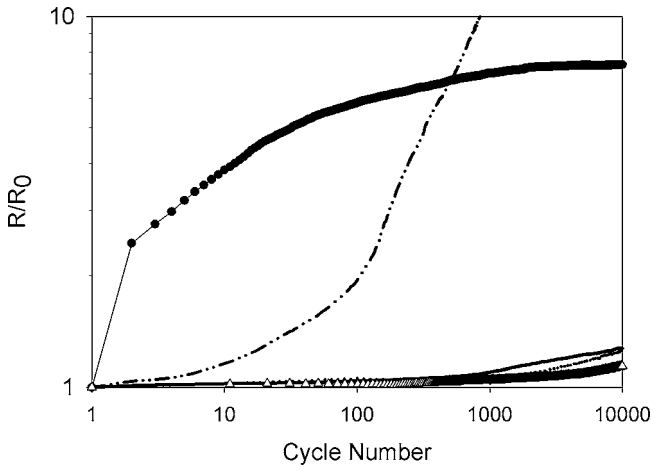

Figure 2: Change in resistance after repeated bending to r = 6mm as function of the number of cycles for ITO (solid circles) and IMI multi layers with Ag thickness of 4 nm (dotted-dashed line), 8 nm (solid line), 12 nm (open triangles), and 15 nm (dotted line).

Another advantage of the IMI structure over ITO was the recovery of electrical conductivity after large increases in resistance due to bending. Resistance was measured after relaxing each sample from a 3 mm radius of curvature back to a 14 mm radius. ITO samples increased in resistance to 10-20 times the original value. On the other hand all IMI samples with at least 8 nm Ag showed an increase of only 1.2 - 2.7 times the original value.

Atomic force microscopy was used to observe the morphology of the Ag layers as a function of thickness. The images in Figure 3 show that for an 8 nm Ag film on ITO, the Ag film is not continuous, while a 12 nm Ag film is smoother and continuous. However the transmission, sheet resistance, and mechanical bending results showed that a continuous Ag layer is not necessary to achieve the benefits of the IMI structure.

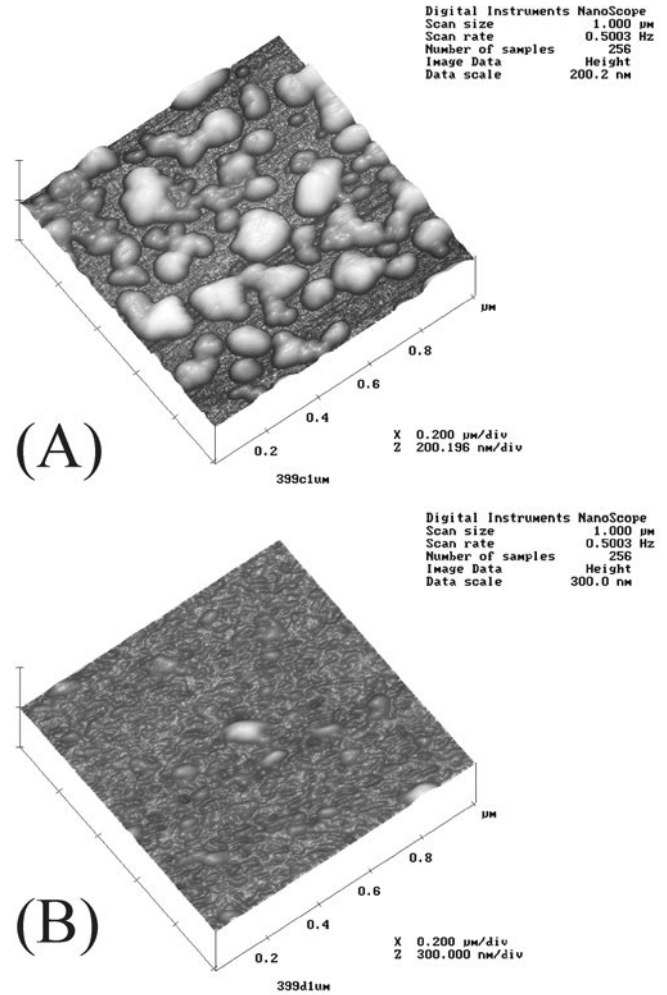

Figure 3: Atomic force microscope images of Ag films deposited on ITO, for Ag thickness of (a) 8 nm and (b) 12 nm.

The response of IMI multilayers to bending suggests that the ductility of the Ag layer provides effective electrical conductivity even after the ITO is beyond its failure strain. This is consistent with bulk Ag, which fails at elongation in the range of 4-50% depending on the preparation of the sample [22]. The sample with 4 nm Ag showed bending performance worse than that of ITO. This could be explained because a 4 nm Ag film forms a discontinuous layer with small Ag islands, while

for an 8 nm Ag film larger Ag islands and more significant inter connectivity is observed.

For integration of IMI structures into applications where ITO is currently used, patterning by wet etching must be demonstrated. Using standard photolithography and commercial etchants we were able to define features in IMI multilayers. Figure 4 shows an optical microscope image of a wet etched feature in a 35/8/35 nm (ITO/Ag/ITO) structure.

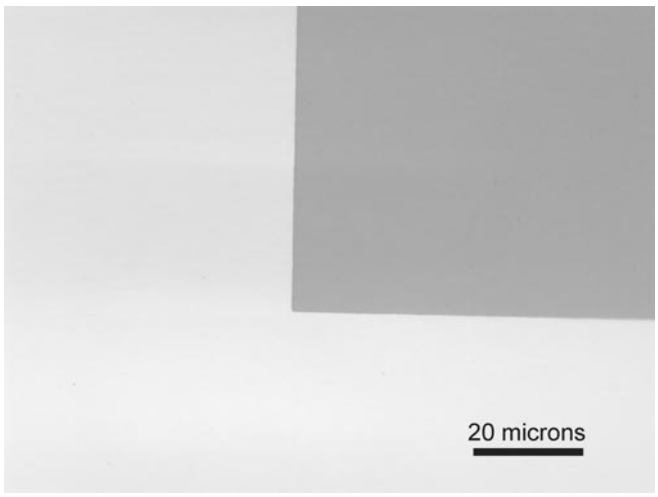

Figure 4: Optical microscope image showing lithographically defined features in (A) ITO and (B) IMI films.

To demonstrate the effect of improved electrical performance of IMI electrodes, OLED devices were fabricated on glass using both ITO and IMI anodes with all other device layers deposited on both samples in the same deposition. The brightness and current are shown as a function of voltage in Figure 5. The current data show that at low voltages the two devices behaved nearly identically, which was expected since the chemical and electrical nature of the injection layer for the two samples is identical. A significant difference between the samples appeared for current densities above 1 mA/cm2 where ohmic losses in the ITO anode become significant. At higher current densities the improved conductivity of the IMI electrodes reduced ohmic losses in the anode and resulted in improved brightness at a given voltage compared to the ITO only devices. This is especially advantageous for high-brightness and passive matrix displays where higher momentary brightness is necessary.

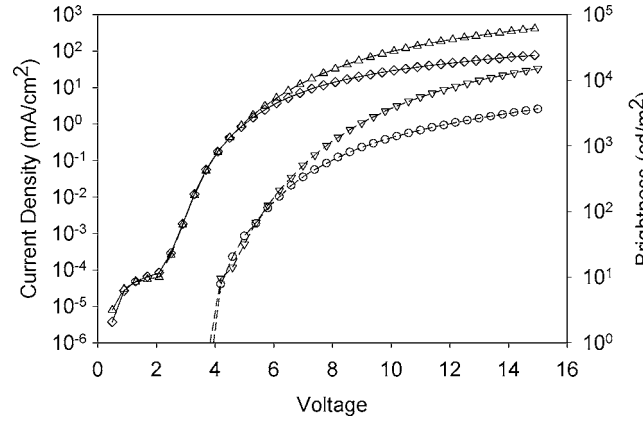

Figure 5: Brightness and current, respectively vs. voltage for OLEDs using ITO (◯, ◇) and IMI multilayers (▽, △) as the anode.

CONCLUSION

IMI structures showed promise for use as a transparent conductor in flexible displays. They provided significantly reduced sheet resistance compared to ITO, and improved bending properties both as a function of radius and as a function of cycling. Excellent performance in transmission, conductivity, and bending was obtained from an 8 to 12 nm Ag layer between 35 nm ITO layers, indicating that high precision of Ag thickness is not required. Even after severe bending to a 3 mm radius the electrical resistance of IMI structures increased by only 1.2 - 2.7 times after relaxing, making them far more robust for handling and processing. It was shown that a continuous Ag layer is not necessary to realize the benefits of the IMI structure over ITO in resistivity, transmission, and improved mechanical robustness. OLED devices fabricated on an IMI anode showed improved performance for current densities greater than 1 mA/cm^2 over similar devices using an ITO anode due to the increased conductivity of the anode.

ACKNOWLEDGMENT

We gratefully acknowledge support for this work from Army Research Laboratories contract DAAD17-01-C-0085.

REFERENCES

1. F. Nuesch, E.W. Forsythe, Q.T. Le, Y. Gao, and L.J. Rothberg, "Importance of indium tin oxide surface acido basicity for charge injection into organic materials based light emitting diodes," J. Appl. Phys., 87, (11), 7973, 2000.

2. Q.T. Le, F. Nuesch, L.J. Rothberg, E.W. Forsythe, and Y. Gao, "Photoemission study of the interface between phenyl diamine and treated indium-tin-oxide," Appl. Phys. Lett., 75, (10), 1357, 1999.

3. M.G. Mason, L.S. Hung, C.W. Tang, S.T. Lee, K.W. Wong, and M. Wang, "Characterization of treated indium-tin-oxide surfaces used in electroluminescent devices," J. Appl. Phys., 86, (3), 1688, 1999.

4. D.R. Cairns, R.P.W. II, D.K. Sparacin, S.M. Sachsman, D.C. Paine, and G.P. Crawford, "Strain-dependent electrical resistance of tin-doped indium oxide on polymer substrates," Appl. Phys. Lett., 76, (11), 1425, 2000.

5. S.K. Park, J.I. Han, D.G. Moon, and W.K. Kim, "Mechanical stability of externally deformed indium-tin-oxide films on polymer substrates," Jpn. J. Appl. Phys., 42, (Pt. 1, No. 2A), 624, 2003.

6. S. Gorkhali, D.R. Cairns, and G.P. Crawford, "Reliability of transparent conducting substrates for rollable displays: A cyclic loading investigation," SID 03 Digest, 1332, 2003.

7. D. Arthur, P. Wallis, M. Trottier, and P. Glatkowski, "Transparent electrodes and circuits from carbon nanotubes," 3rd Annual Flexible Displays and Microelectronics Conference, Phoenix, AZ, 2004.

8. J.C.C. Fan, T.B. Reed, and J.B. Goodenough, "Heat mirrors for solar-energy collection and radiation insulation," 9th Intersociety Energy Conversion Engineering Conference Proceedings, San Francisco, CA, 341, 1974.

9. G. Leftheriotis, P. Yianoulis, and D. Patrikios, "Deposition and optical properties of optimised ZnS/Ag/ZnS thin films for energy saving applications," Thin Solid Films, 306, 92, 1997.

10. X. Liu, X. Cai, J. Qiao, J. Mao, and N. Jiang, "The design of ZnS/Ag/ZnS transparent conductive multilayer films," Thin Solid Films, 441, 200, 2003.

11. X. Liu, X. Cai, J. Mao, and C. Jin, "ZnS/Ag/ZnS nano-multilayer films for transparent electrodes in flat display applications," Applied Surface Science, 183, 103, 2001.

12. S.J. Nadel, "Durability of Ag based low-emissivity coatings," J. Vac. Sci. Technol. A, 5, (4), 2709, 1987.

13. E. Kusano, J. Kawaguchi, and K. Enjouji, "Thermal stability of heat-reflective films consisting of oxide-Ag-oxide deposited by dc magnetron sputtering," J. Vac. Sci. Technol. A, 4, (6), 2907, 1986.

14. J.C.C. Fan, F.J. Bachner, H. Foley, and P.M. Zavracky, "Transparent heat-mirror films of TiO_2/Ag/TiO_2 for solar energy collection and radiation insulation," Appl. Phys. Lett., 25, (12), 693, 1974.

15. J.J. Finley, "Development of a multilayer thin-film solar control windshield," J. Vac. Sci. Technol. A, 14, (3), 739, 1996.

16. H. Ohsaki and Y. Tachibana, "Low resistance AR stack including silver layer," Thin Solid Films, 442, 153, 2003.

17. Y. Tachibana, K. Kusunoki, T. Watanabe, K. Hashimoto, and H. Ohsaki, "Optical properties of multilayers composed of silver and dielectric materials," Thin Solid Films, 442, 212, 2003.

18. M. Fahland, P. Karlsson, and C. Charton, "Low resistivity transparent electrodes for displays on polymer substrates," 3rd International Conference on Coatings on Glass, Maastricht, NL, 689, 2000.

19. M. Bender, W. Seelig, C. Daube, H. Frankenberger, B. Ocker, and J. Stollenwerk, "Dependence of film composition and thicknesses on optical and electrical properties of ITO-metal-ITO multilayers," Thin Solid Films, 326, 67, 1998.

20. Y. Aoshima, M. Miyazaki, K. Sato, Y. Akao, S. Takaki, and K. Adachi, "Development of silver-based multilayer coating electrodes with low resistance for use in flat panel displays," Jpn. J. Appl. Phys., 39, 4884, 2000.

21. K.H. Choi, J.Y. Kim, Y.S. Lee, and H.J. Kim, "ITO/Ag/ITO multilayer films for the application of a very low resistance transparent electrode," Thin Solid Films, 341, 152, 1999.

22. E.A. Brandes, "Smithells Metals Reference Book," 6th edition, Butterworth & Co., London, 1983.

Quality of Plasma Polymerized Corrosion Resistant Layers of New Materials in Large Scale Coating Machines for Car Reflectors

K. Nauenburg, P. Fiedler, W. Dicken, G. Deppisch, K. Kruse, and G. Ickes,
Leybold Optics GmbH, Alzenau, Germany

Key Words: Plasma polymerization, Corrosion resistant coatings, Mirror coatings, Polymer substrates

ABSTRACT

For more than three decades, corrosion resistant layers for automotive light reflectors were deposited by PCVD using Hexamethyldisiloxane as a common source. This siloxane is easy to evaporate due to its high vapor pressure, it is available at an acceptable price, and the plasma polymers have all the properties required to fulfill the different specifications of car manufacturers and their suppliers throughout the world. Progress in the development of modern car lights leads to light sources with a higher light output, but smaller housings with an increasing temperature impact on the thermo-plastic materials. This is why the temperature resistance of corrosion resistant layers must be improved. Another ongoing target to cut coating costs is the reduction of process times. New siloxanes and their mixtures with gases are an approach to improve corrosion resistance and increase deposition rates. The paper reports first results obtained from a series of different production machines, including evaporation batch coaters, short-cycle sputter machines such as the DynaMet family, and the new PylonMet 1V sputter system.

MOTIVATION

In the production of automotive lamps, there is a trend towards smaller housings with a higher light emission. This results in higher energy in the light source and a higher temperature impact on the plastic reflector. Thus the complete reflective layer stack has to withstand higher temperatures. This also means that the corrosion resistant plasma polymer has to remain stable under such critical conditions. Another important issue is the ongoing target of cutting coating costs by reducing process times. This can, for example, be done by increasing the deposition rate of the plasma polymer.

GOAL

The corrosion resistant plasma polymer top coat must have sufficient temperature stability and/or a higher deposition rate. The goal was to find a new siloxane monomer for the top coat. Highly cross-linked materials have a higher temperature stability. So the siloxane has to contain additional functional groups for high cross-linking. In plasma polymerization processes, high deposition rates can be reached by faster reactions and higher reaction rates. This is why the monomer has to contain functional groups with weak bonds which can be broken by a lower energy input into the plasma polymerization, or in higher numbers by the same energy input. Therefore we have to work on the evaluation of new siloxane monomers.

REQUIREMENTS

The new siloxane monomer, which we called "Glipoxan 2", and/or its mixtures with our standard monomer Glipoxan (Hexamethyldisiloxane, HMDSO) has to:

1. be non-toxic, non-corrosive, harmless
2. be non-explosive, self-igniting etc.
3. have a high vapor pressure at acceptable heating temperatures (below 60°C – gas flow controller)
4. be a liquid (for easy filling)
5. have an acceptable price, and
6. good availability.

We have to compare the new monomer "Glipoxan 2" with the normally used monomer Glipoxan (HMDSO) regarding the following process conditions:

1. plasma frequency (DC (AluMet), 40kHz (PylonMet), 13.56 MHz (DynaMet))
2. plasma power
3. deposition time
4. monomer flow rate
5. deposition pressure
6. gas phase composition (mixtures with gases and/or other monomers), and
7. geometry of the plastic parts (depth, etc.)

PYLONMET COATER DESIGN

The Inter-Pole Target (IPT) sputter cathode is an extremely powerful tool for metallizing plastic parts within a very short time with highly reflecting metal layers—mostly aluminum for automotive light reflectors, but also copper, silver, chromium, nickel-chromium or stainless steel for bezels, mirrors or decorative plastic parts. After more than 10 years of successful experience in industrial production with the short-cycle multichamber metallizers of the DynaMet family, we designed a single-chamber solution: the PylonMet.

 505/856-7188 ISSN 0737-5921
47th Annual Technical Conference Proceedings (April 24–29, 2004) Dallas, TX USA

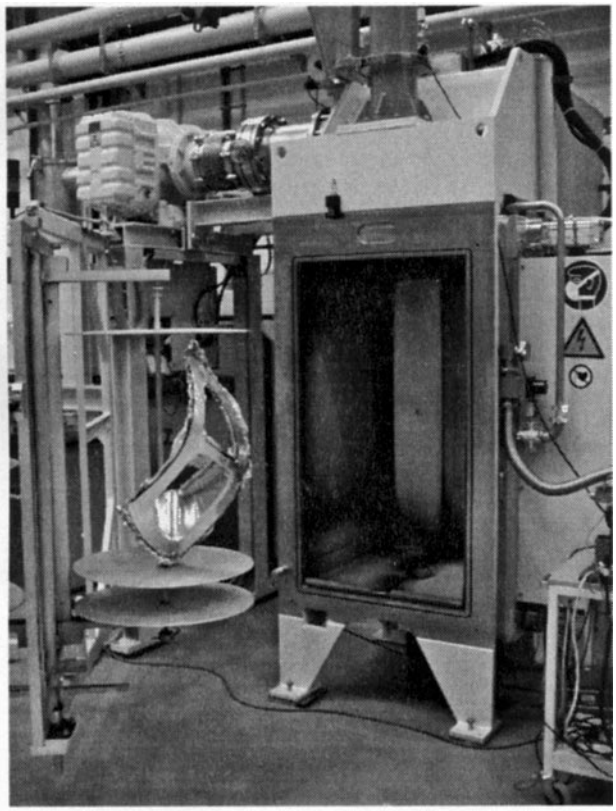

Figure 1: The PylonMet 1V coater with an example of a hard-to-coat plastic part.

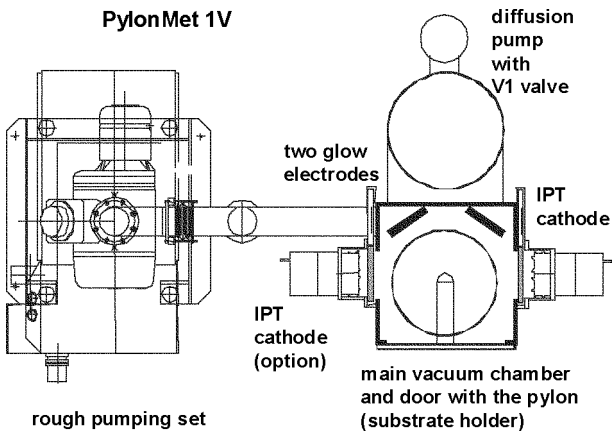

Figure 2: The PylonMet 1V coater in a schematic view.

Up to five plasma processes—sputtering, mid-frequency plasma pretreatment and several steps of polymerization—are performed to produce complete layer stacks for modern automotive reflectors within a few (normally 3 to 5) minutes. The cycle time depends on the number of required process steps. The parts are mounted on a vertical substrate holder (pylon) and can be rotated with controlled speed and direction. Thanks to the stepper motor drive, non-continuous pylon movements can be programmed as well to coat very complex parts. The bigger size of the chamber and pylon is an advantage when coating extremely long, wide and deep parts—mostly large headlights and bezels (see Figure 1).

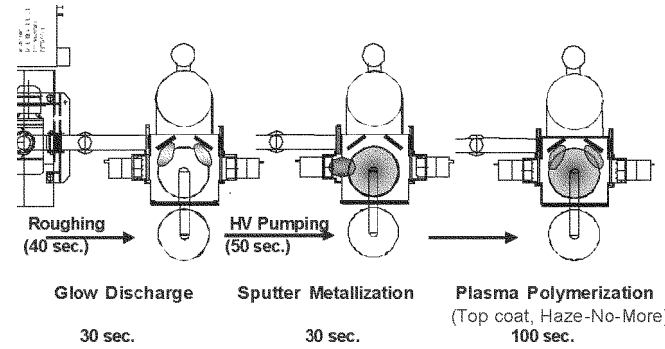

Figure 3: Sequence of processes in the PylonMet 1V coater for automotive reflectors.

The coater is pumped down with a powerful rough pumping set (SV 630 rotary pump and a frequency controlled RA 3001 roots blower) which is also used during the glow discharge pretreatment and polymerization processes (40 kHz, max. 10 kW). For best results in reflectivity and quality of sputtered aluminum layers, high vacuum pumping is done by a DIP 20000 diffusion pump, supported by a Polycold PFC 1100 system (surface area >2 m^2). The metal is sputtered with one or two high deposition rate IPT cathodes (up to 90kW power, up to 20 nm/s). The target has a high material usage (approx. 50%) and a long lifetime (2 weeks/3-shift production) and can be exchanged quickly. Sputtering is normally followed by the deposition of the top coat layers. These processes are done by plasma polymerization with glow discharge. The required vaporized monomers (one for corrosion protection, the other for our haze-no-more top coat) are controlled and supplied by the coater's monomer box. This special feature of the equipment (shown in Figure 4) contains two bottles for the liquid monomers, two monomer pipes with a pressure controller and valves, and a mass flow controller calibrated for Glipoxan (HMDSO).

The box is temperature controlled up to 60°C by a heat blower. For easy and safe handling of the monomer liquids, each of the two bottles is equipped with its own filling pipe with a special connector.

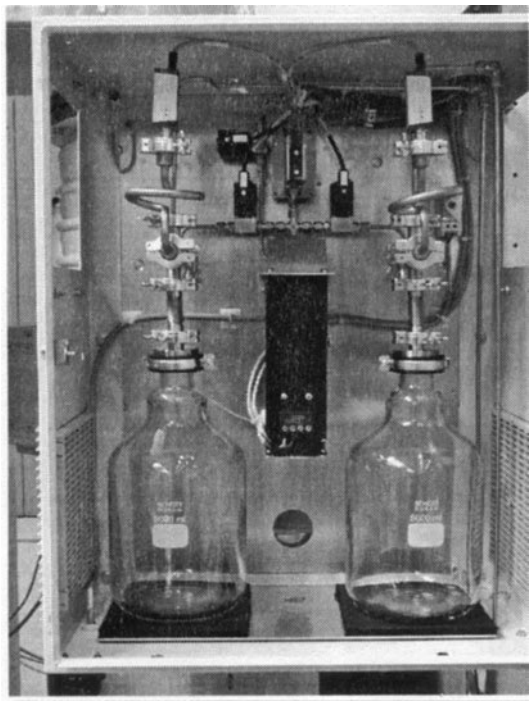

Figure 4: The PylonMet 1V monomer box.

LAYER SYSTEM PROPERTIES

To guarantee the same or even a better quality, we had to check the properties of the complete layer stacks on 3D plastic reflectors (PC).

Optical properties:

1. Reflectivity (>85%, on the real part)
2. Color (L*,a*,b*; b* <1.5)

Corrosion protection properties:

3. NaOH solution (1%; >10 min.)
4. Accelerated climate chamber (52°C, >120 h.)

Mechanical properties:

5. Adhesion: Cross hatch/Tape (Tape Tesa 4124, - no visible delamination)

We also checked the following properties of the plasma polymer coatings deposited on Si-wafers:

Optical properties:

6. Refractive index at 550nm

Mechanical properties:

7. Thickness/deposition rate

Both measured with an ellipsometer.

PLASMA POLYMERIZATION RESULTS

This evaluation was done on real plastic parts: a larger bezel (45 x 15 x 20 cm) without lacquer (directly coated), and a "normal" shaped lacquered reflector made of BMC/GF (25 x 15 x 10 cm depth) with full layer stacks. The bezels were made in a PylonMet 1V sputter coater (40 kHz), while the lacquered reflectors were made in an AluMet 900 H evaporation system (DC glow discharge). For the base coat and the corrosion protecting top coat, we took the best parameter settings we found in our experimental work. Thickness and deposition rates for pure Glipoxan and "Glipoxan 2" mixtures (A and B) were determined on Si-wafer pieces mounted in the plastic part. Results are shown below in Figures 5 and 6.

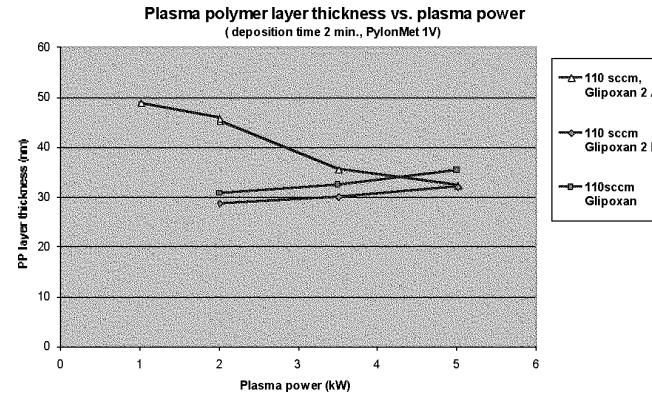

Figure 5: Results of plasma polymer layer thickness made in the PylonMet 1V.

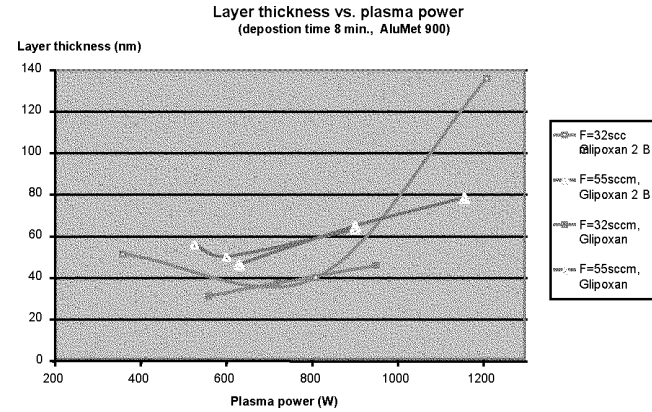

Figure 6: Results of plasma polymer layer thickness made in the AluMet 900 H.

As can be seen in Figures 5 and 6, we achieved higher deposition rates using "Glipoxan 2". However, we found haze (white silicon dioxide dust) on some parts during our tests. The dust is presumably generated by the solidified monomer in the plasma process. This phenomenon leads to an unacceptable product quality. We also found parameter settings where all optical, corrosion protection and mechanical properties of the "Glipoxan 2" monomer layers were the same as, or even better than, those of the pure Glipoxan monomer.

CONCLUSION AND OUTLOOK

1. The corrosion protection plasma polymers of the new monomer "Glipoxan 2" show properties (optical, mechanical, corrosion resistance) that are the same as, or better than, those of the well-known monomer Glipoxan.
2. Temperature tests are in progress.
3. For "simple geometries", the results show a potential to double or triple the deposition rates.
4. The parameter settings we used up to now sometimes showed dust generated by a very intense plasma polymerization process. This seems to be a "dead-end street". A second set of more promising experiments is currently being conducted and will be published later.

REFERENCES

1. R. Kukla, T. Krug, R. Ludwig, and K. Wilmes, "A highest rate self sputtering magnetron source", Vaccum, 41, 1968, 1990.

2. R. Kukla, H. Grünwald, G. Ickes, M. Jung, and U. Patz, "Just-in-time coater for 3-dimensional plastic parts", 38th Annual Technical Conference Proceedings of the Society of Vacuum Coaters, p. 340, 1995.

3. H. Grünwald, J. Henrich, J. Krempel-Hesse, W. Dicken, S. Kunkel, G. Ickes, and J. Snyder, "Rapid, high quality metallization of plastics", 40th Annual Technical Conference Proceedings of the Society of Vacuum Coaters, p. 44, 1997.

4. H. Grünwald, R. Adam, J. Bartella, M. Jung, W. Dicken, S. Kunkel, K. Nauenburg, T. Gebele, S. Mitzlaff, G. Ickes, U. Patz, and J. Snyder, "Better aluminium mirrors by intergrating plasma pretreatment, sputtering, and plasmapolymerization for large-scale car headlight production", Surface and Coating Technology, 111, 287, 1999.

4. K. Nauenburg, U. Braun, W. Dicken, G. Ickes, and M. Röder, "Large-scale production of reflectors by integrating plasma pretreatment, sputtering and plasma polymerization in an one-chamber coater", 46th Annual Technical Conference Proceedings of the Society of Vacuum Coaters, p. 636, 2003.

Stress Reduction in Sputter Deposited Thin Films Using Physically Self-Assembled Nanostructures as Compliant Layers

T. Karabacak, J.J. Senkevich, G.-C. Wang, and T.-M. Lu, Department of Physics, Applied Physics and Astronomy, Rensselaer Polytechnic Institute, Troy, NY

Key Words: Sputter deposition, Film stress, Adhesion, Self-assembly

ABSTRACT

The stress in thin films has been a major limiting factor for obtaining high quality films. We will present a new strategy of stress reduction in sputter deposited films by a nano-compliant layer at the substrate using physically self-assembled nanostructures obtained either by an oblique angle deposition technique or by a high working gas pressure process prior to the deposition of the continuous film. The technique is all in situ, does not require any lithography steps, and the nanostructures are made of the same material as the deposited thin film. The nanostructures have a lower material density and can act as a compliant layer to reduce the stress of the later deposited continuous film. By using this approach we were able to reduce stress values by approximately one order of magnitude in sputter deposited tungsten films. Our experimental results agree well with the predictions of a theoretical model that we developed to explain the stress relief through the nanostructured compliant layer. In addition, these lower stress thin films exhibit a stronger adhesion to the substrate and the delamination is avoided. This strategy leads to the growth of much thicker films with high structural reliability.

INTRODUCTION

The control of stress in physical vapor deposited thin films is of continued interest due to its close relationship to technologically important material properties. Further, thin film stress often determines its adhesive strength to the substrate [1-3], the limit of film thickness without cracking, buckling, or delamination [4-9], electrical properties [10-12], and optical properties such as distortions in x-ray masks [13].

It has been shown [14,15] that the intrinsic stress in sputtered tungsten films is correlated to Thornton's structure zone model (SZM) [16]. The SZM relates the microstructures of sputtered thin films to the most prominent deposition parameters such as working gas pressure and substrate temperature. The studies by Haghiri-Gosnet et al. [14] and Windischmann [15] have revealed that the transition from zone-1 of a porous and columnar structure to zone-T of a denser film, e.g. by passing from high to lower working gas pressures, corresponded to a dramatic change of stress from high tensile to high compressive values (i.e. from a few GPa tensile to a few GPa compressive for tungsten). The rapid change of stress with pressure allows only a narrow window of pressures that yields reasonably low stress values (i.e. ≤ a few hundred MPa for tungsten). Therefore, obtaining low-stress films by controlling the working gas pressure (at a fixed pressure during deposition) has been difficult and is not a robust method [14]. In the high-pressure part of zone-1 it is possible to produce low stress films. However, these films exhibit poor electrical properties due to the columnar microstructure.

Similarly, the stress is a sensitive function of dc bias voltage [11] and substrate temperature [14,17] near the transition between tensile and compressive values, which makes the stress control difficult. A rf-substrate biasing technique has been shown to improve the stress control over an optimum regime of cathode current, pressure, and the rf-substrate bias values [11]. On the other hand, the method is sensitive to the type of materials to be deposited, and finding the optimum parameter space can be challenging. In addition, Maier et al. studied the effect of plasma-etch surface treatment of graphite substrates before a deposition on the adhesion properties of tungsten films sputter deposited at various temperatures [9]. Their plasma treatment is a chemical method that suffers limitations of the type of substrate materials and the material to be deposited. Also, the deposition may need high substrate temperatures. Recently, Windt [18] was able to reduce the stress in sputter deposited W films using a bilayer structure of W/Cr. He adjusted the deposition conditions to give compressive and tensile stress in W and Cr layers, respectively. His results suggest that with a suitable choice of layer thicknesses for W and Cr, the net stress in the bilayer can be made to balance each other.

In the present work, it will be shown that a nanostructured compliant layer (NCL) obtained by a self-assembled growth mechanism can effectively relieve the stress of a continuous sputter deposited film. The self-assembled nanostructures will provide the single processing step of low-stress films and will avoid the lithographic steps. The compliant layer can make the stress reduction independent of the deposition parameters like pressure, temperature, and substrate biasing.

We will study two in situ methods of producing physically self-assembled NCL: 1) *Oblique angle sputter deposition* (OASD), and 2) *processing at higher working gas pressures*.

505/856-7188 ISSN 0737-5921
47th Annual Technical Conference Proceedings (April 24–29, 2004) Dallas, TX USA

OASD has been recently shown to be an effective method of fabricating nanostructures of various shapes (i.e., nanorods, nanosprings, and etc.) and sizes (i.e., from a few nanometers up to a few hundred nanometers) by a physical self-assembly mechanism [19-21]. The method is simple, easy to implement, all in situ, and can be applied to any materials that can be vaporized. Basically, in the OASD the incident flux of sputtered material impinges on a tilted substrate. The preferential growth of incident particles on the taller surface features results in the formation of slanted nanocolumns. Also, if the substrate is set to rotate with the rotational axis perpendicular to the substrate, vertical nanocolumns can be formed.

The second and perhaps a simpler way of obtaining a NCL is using the SZM of sputter deposited films themselves. A "revised SZM" study by Messier et al. [22] has shown that zone-1 of classical SZM consists of five different sub-zones of columnar "nanostructures" with typical sizes varying from 1-3 nm to 200-400 nm. At high working gas pressures, enhanced collision and scattering events result in particles that obliquely incident on the substrate surface. Therefore, the shadowing effects give rise to the formation of columnar structures. The reduced ion bombardment at high pressures slows down the adatom mobility and therefore results in less dense films. The nanocolumns are typically separated from each other by voids that are lower density regions [23]. This indicates that the low density regions can be as small as atomic scales, and also at the same time be as large as a few tens of nanometers in size.

Hence, once the nanostructured compliant layer by either one of the methods described above is formed, we can simply change the angle of incidence to normal incidence (for the method of using OASD) or decrease the working gas pressure (for the method of using higher working gas pressures) in situ to deposit the usual continuous dense layer of material. Then we can expect that the compliant layer will relieve the stress in the continuous thin film, which then results in better adhesion, larger critical thickness, and better quality films. The process can be repeated to form thick multilayer films.

EXPERIMENT

In our experiment, a dc magnetron sputtering system was used to deposit W films. The films were deposited on oxidized p-Si(100) (resistivity 12-25 Ω-cm) wafers (diameter ~7.6 cm) using a 99.95% pure W cathode (diameter ~7.6 cm). The substrates were mounted on the sample holder located at a distance of about 15 cm from the cathode. In the OASD, the substrate is tilted so that the angle θ between the surface normal of the target and the surface normal of the substrate can be large. In our present case, the angle was either 85° (for nanorods) or 50° (for continuous films). In the normal incidence sputter deposition (NISD) the tilt angle was set to 0°. The base pressure of ~2 x 10^{-6} Torr was achieved by a turbomolecular pump backed by a mechanical pump. In all the deposition experiments, the power was 200 Watts at an ultra pure Ar pressure of 2.0 mTorr (for dense films at normal incidence or nanorods at oblique angle incidence) or 15 mTorr (for columnar films at normal incidence). The deposition rates were measured to be ~12 nm/min for normal incidence deposition, ~11 nm/min at θ = 50°, and ~5 nm/min at θ = 85° for oblique angle depositions all at 2 mTorr Ar pressure. At 15 mTorr, normal incidence growth gave ~16.5 nm/min deposition rates. The thickness of a film was determined by a step-profilometer and also verified by scanning electron microscopy (SEM) cross-sectional images. In this study, we will label the very first NCL layer on the silicon substrate as n = 1, the second denser W layer as n = 2, the following NCL as n = 3, and so on.

The surface topography was investigated using optical microscopy and atomic force microscopy (AFM). We used a contact-mode AFM (Park Scientific Auto CP) where the radius of the silicon tip used was about 10 nm, and the side angle was about 12°. The scan sizes were 2 x 2 μm^2 with 512 x 512 pixels. The root mean square (RMS) roughness values were extracted from the quantitative surface height values. The crystal structure information was studied by X-ray diffraction (XRD) measurements using a Scintag diffractometer with a Cu target (λ = 1.5405 Å) operated at 50 kV and 30 mA. The diffractometer was calibrated with respect to the peak positions of a Si calibration standard.

The measurements of intrinsic thin film stress were performed by using a dual wavelength (λ_1 = 670 nm and λ_2 = 750 nm) Flexus 2320 system, which uses a wafer curvature technique. The film stress σ then was calculated using Stoney's equation [24]

$$\sigma = \frac{1}{6R}\frac{E}{(1-\nu)}\frac{d_{sub}^{\ 2}}{d},$$

Equation 1

where E, n, and d_{sub} are Young's modulus, Poisson's ratio, and thickness of the substrate, respectively, and d is the film thickness (assuming $d << d_{sub}$). Before a deposition, the R is the radius of curvature of the reference wafer (R_1). After a deposition, the R becomes the relative substrate radius of curvature and is calculated as $R = R_1R_2/(R_1-R_2)$, where R_1 and R_2 are the radii of curvatures before and after depositions, respectively. In conventional notations, positive signs of film stress correspond to tensile and negative signs to compressive stress values. However, since all the tungsten films we investigated were in compressive stress state, in this paper positive signs will be used to represent the compressive stress. The maximum temperature of the substrate during the deposition was measured to be ~85°C. It has been previously shown that a ~50°C increase in substrate temperature during sputter

deposition of tungsten corresponded to a negligible "thermally induced" stress value of ~50 MPa [10]. Therefore, in our work the reported stress values are mostly incorporated during film growth or "growth induced" stress.

In addition, qualitative adhesion tests were made by using a scotch tape peel test. However, in cases where the film was already peeling off or flaking itself, we did not perform the peel test and considered this film as failed in adhesion.

RESULTS AND DISCUSSION

We first studied the evolution of stress and adhesion properties of W films deposited on silicon wafers at normal incidence with no compliant layer present. W film was observed to delaminate and peel off after a thickness of ~240 nm. Figure 1 shows optical microscopy topographies of the delaminated W film at various thicknesses. The delamination patterns are in the form of randomly oriented wrinkles at thickness ~240 nm (Figure 1a), parallel periodic wrinkles at ~600 nm (Figure 1b), and irregular-shaped flakes at ~1,440 nm (Figure 1c). Similar decohesion patterns for W films were observed before [5,6] and explained by the high compressive stress values in the film and followed by relaxation in the form of wrinkles. As a driving force of the wrinkle formation, the elastic energy that originates from the film stress stored in the layer/substrate system is considered [6,25].

Then, we investigated two in situ techniques in order to obtain the physically self-assembled NCL.

Nanostructured Compliant Layers by Oblique Angle Sputter Deposition

To relieve the stress, we fabricated the NCL using the OASD technique. We deposited W films on Si wafers tilted at a high oblique angle of $\theta = 85°$ with no substrate rotation. Due to the shadowing and physical self-assembly mechanisms we were able to obtain the slanted tungsten nanorods structure. The inset in Figure 2 shows an example of nanorods structure (~650 nm thick) obtained this way. The actual NCL structures for our present study were fabricated at a much smaller thickness of ~50 nm. The stress measurements on the NCL samples (~50 nm W nanorods) revealed that the compliant layer had only a negligible stress value of –3.8±5.2 MPa. Then, W films were deposited on the NCL substrate at normal incidence and at various thicknesses. W films did not delaminate up to a thickness of ~500 nm (almost twice the critical thickness compared to that without NCL), and started to display delamination features in parts of the wafer. In addition, these W films with NCL were smooth (e.g RMS = 0.87±0.05 nm for ~240 nm thick film).

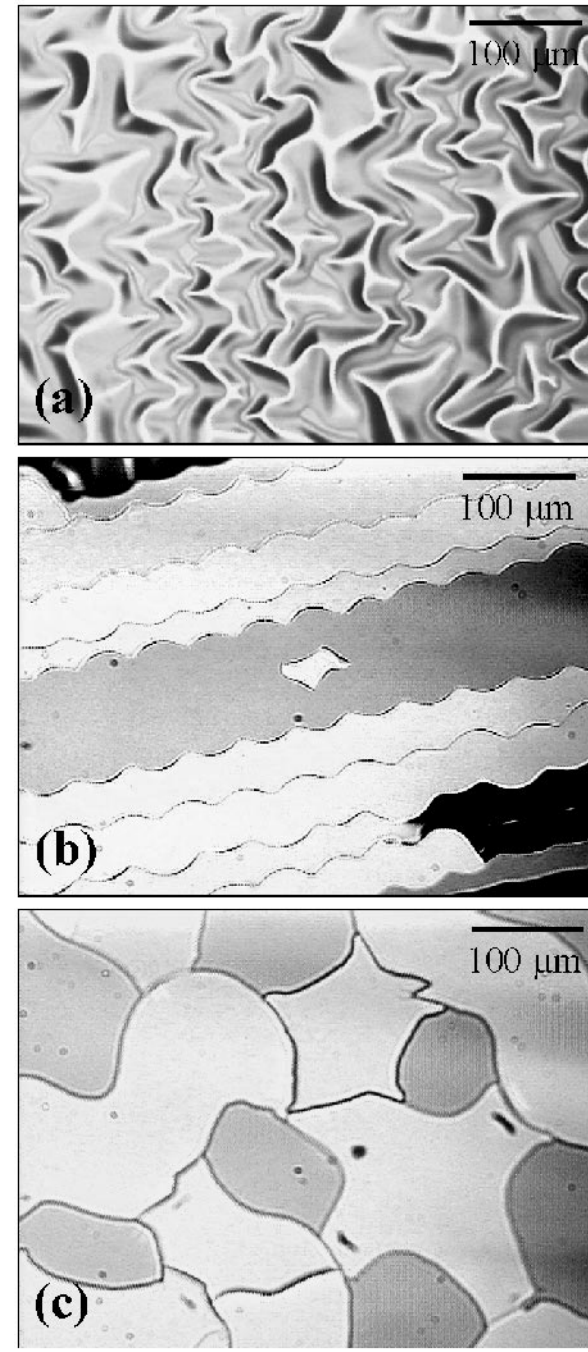

Figure 1: Optical microscopy images of tungsten morphologies: (a) ~240 nm, (b) ~600 nm, (c) ~1,440 nm thick W films deposited on bare Si substrates. Film delaminations can be seen clearly. Black color regions in (b) are the W film that delaminated and completely peeled off. Light gray parts in (b) and (c) are delaminated W films that still barely stick to the Si surface, and dark gray regions are exposed Si surface areas. The scale bars are 100 μm.

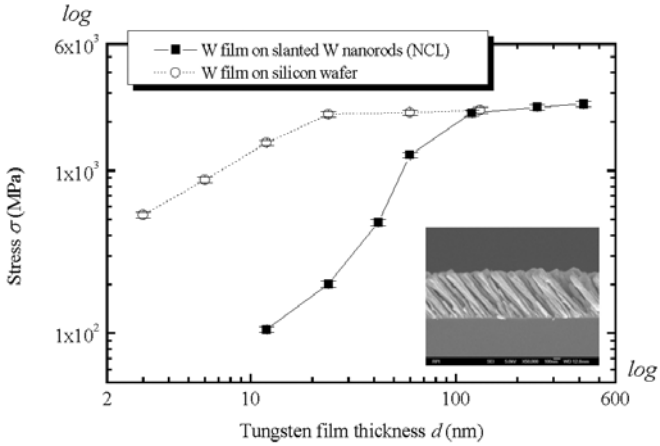

Figure 2: Measured stress values of tungsten films are plotted as a function film thickness in log-to-log scale. The open circles are from the depositions with no NCL. Filled squares represent the stress data for W films deposited on Nano-Compliant Layer (NCL) of slanted W nanorods (~50 nm thick). The inset shows a SEM image of slanted W nanorods fabricated by oblique angle sputter deposition (OASD). The thickness is ~650 nm. The actual Nano-Compliant Layer (NCL) that we used for our study is only ~50 nm thick. The scale bar is 100 nm.

Figure 2 compares the stress values of W films as a function of film thickness deposited on bare Si wafers and NCL. The stress of the W film was calculated by defining the NCL/Si-wafer structure as the reference substrate (E, n, and d_{sub} were approximated to be the Si-wafer's values due to the negligible NCL stress). All the stress data presented are compressive type. It is realized from Figure 2 that W films with no compliant layer quickly develop a high compressive stress value. On the other hand, the stress values for W films deposited on NCL are approximately one order of magnitude lower than the ones at similar thicknesses without NCL. This shows the effectiveness of NCL in stress reduction. We should also note that a continuous W film on NCL nanorods only develops after a film reaches a thickness of ~10 nm as observed from SEM images (not shown here). Before that the W film is in the form of isolated islands due to the underlying nanorods surface. In addition, all the W films deposited on NCL in Figure 2 passed the scotch tape peel test that indicates the enhancement in adhesion.

To explain the stress reduction effect of NCL we developed [26] a simple model that was inspired from the previous calculations by Luryi et al. [27] and Zubia et al. [28,29] who studied the effects of patterned surfaces on heteroepitaxial film stresses. We obtained the following representation for the final stress of a film with NCL.

$$\sigma = c\,D\left(1-e^{-\frac{\pi d}{D}}\right)\left[1+K\frac{\left(1-e^{-\frac{\pi d}{D}}\right)}{\left(1-e^{-\frac{\pi d_c}{D}}\right)}\right]^{-1},$$

Equation 2

where d (or d_c) is the thickness of the film (or NCL) and c is a material specific constant. D is the average nanorod diameter in NCL. K in Equation 2 is defined as

$$K = -\frac{E}{(1-\nu)}\frac{(1-\nu_c)}{E_c},$$

Equation 3

where E (or E_c) and n (or n_c) are the Young's modulus and Poisson's ratio of the film (or nano-compliant layer), respectively. Figure 3 shows the best-fit predicted by Equation 2 to the experimental stress values of the W films deposited on NCL (from Figure 2). The model agrees well with the experimental results and it is shown that the stress will be saturated after a critical thickness. In addition, Equation 2 also predicts that for a given film thickness the stress should decrease with the increase of NCL thickness. In fact, we performed a series of experiments where we prepared NCL for various thicknesses. As shown in Figure 4, we observed that the high stress values for ~120 nm W films decreased to negligible amounts as we increased the thickness of NCL.

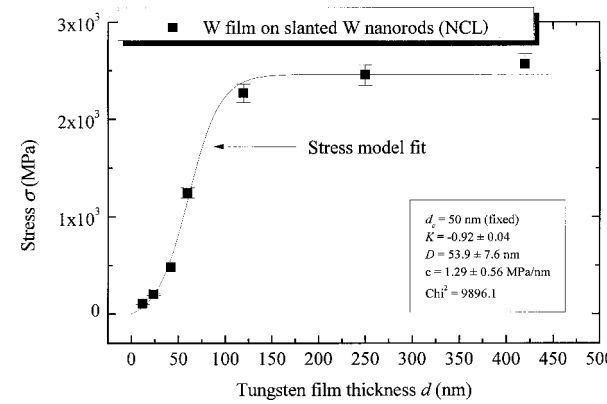

Figure 3: The evolution of stress with thickness for W films deposited on Nano-Compliant Layer (NCL) of W nanorods (~50 nm thick) is predicted with the model from Equation 2. The solid line is a best fit using this model. d_c is the thickness of the NCL and D is the average diameter of nanorods that form NCL. c and K are the material specific constants.

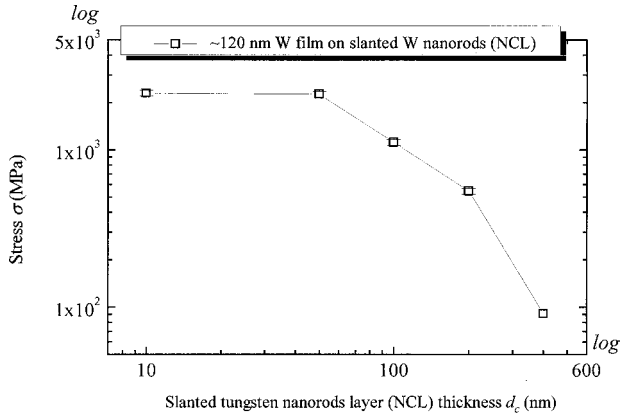

Figure 4: The reduction in the stress values for ~120 nm W films as a function of the thickness of the NCL.

In addition, we also investigated the possibility of growing very thick tungsten films successively by repeating the multilayer structure steps of NCL/W-film. For this, we used an in situ controller to change the tilt angle θ of substrate such that at high θ we got the nanorods for NCL and at low θ we obtained the continuous film. However, the angle values that were allowed by the geometry of the current setup were limited to 50°-90°. Fortunately, 50° was small enough to give continuous W films (which have similar stress and delamination behavior as the films deposited at θ = 0°) as evidenced from SEM measurements. Figure 5a shows the optical microscopy image of a continuous ~550 nm thick W film deposited at θ = 50°. The film had an extreme delamination. Then we deposited a multilayer W film obtained by successively depositing the W film in situ with the first ~50 nm at 85° (layer number n = 1), the second ~550 nm at 50° (n = 2) and so on (up to total number of layers n = 6). As can be seen from Figures 5b and 5c, the multilayer film was ~1,850 nm thick, and was relatively smooth (RMS ~ 14.0±0.5 nm). There was no delamination at all. In addition, the film passed the peel test and had a very low stress value of σ ~384.1 MPa.

Nanostructured Compliant Layers by Processing at Higher Working Gas Pressures

As described in the introduction, another and even simpler method of producing nanostructures is by working in the deposition conditions of zone-1 of SZM. Especially at high working gas pressures, the film structure is formed by the closely packed nanocolumns. Therefore, we studied the possibility of using zone-1 films as NCL. In a previous study by Shen et al., who used a similar W deposition system, it has been shown that the film stress gets close to zero at around ~15 mTorr [30]. Therefore, we set the Ar pressure to 15.0 mTorr to obtain the low stress NCL of columnar W. For the low-pressure value, we used 2.0 mTorr, which would give dense but stressed films. We performed normal incidence deposi-

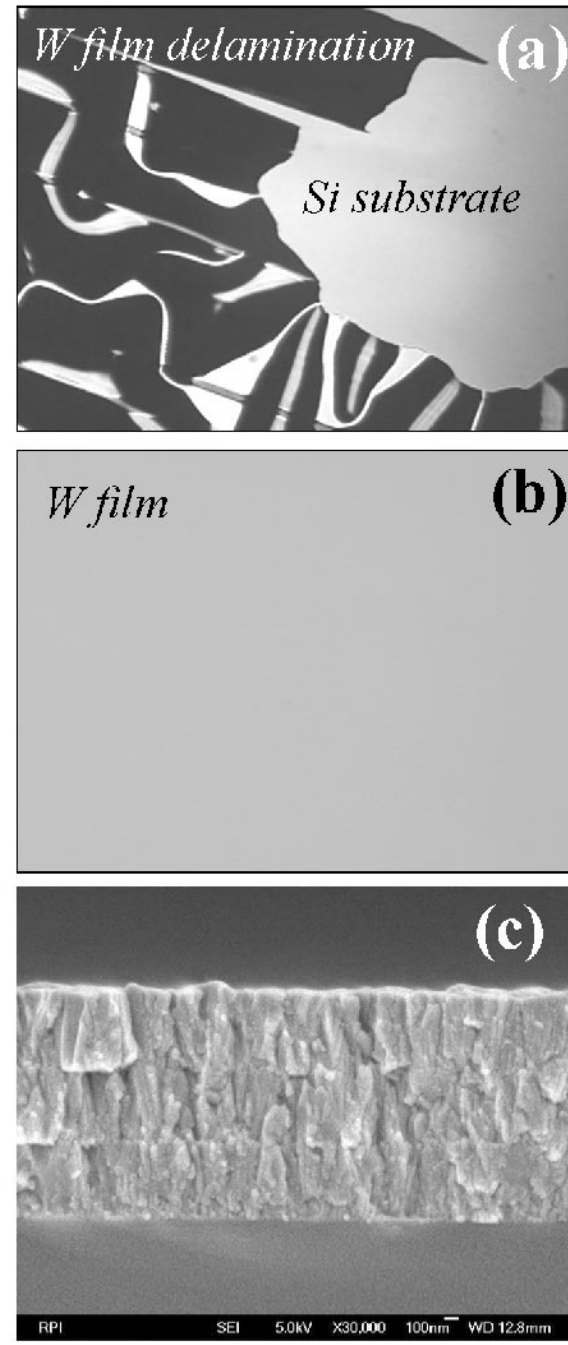

Figure 5: a) Optical microscopy image of a continuous ~550 nm thick W film deposited on a bare Si substrate at θ = 50°. Extreme peeling exists in the film. b) Optical microscopy image and c) cross-sectional SEM image of a multilayer (number of layers n = 6) W film grown by successively depositing the W film in-situ with the first ~50 nm film at 85° (n = 1), the second ~550 nm film at 50° (n = 2), and so on. The multilayer film is ~1,850 nm thick and there was no delamination. The surface RMS roughness was ~ 14.0±0.5 nm. The scale bar is 100 nm.

tions on silicon wafers starting from the high-pressure step and successively changing the pressure between high and low at the end of each layer. We set the thicknesses of the NCL and the denser film to 165 nm and 120 nm, respectively.

The multilayer NCL/dense W films of high/low Ar pressure (e.g. 15 mTorr/2 mTorr) did not delaminate for any of the thicknesses we investigated (e.g. up to ~2,300 nm formed by n = 16 individual layers). The films were smooth (e.g. RMS = 1.3±0.1 nm for ~570 nm thick multilayer W film with n = 4). In addition, all these W films deposited with NCL passed the scotch tape peel test that indicates the enhancement in adhesion.

Figure 6 shows the measured stress values of multilayer (high/low Ar pressure) tungsten films as a function of total film thickness. As shown in Figure 2, single layer W films made under low Ar pressure quickly develop very high compressive stress values (~2.35 GPa even at ~120 nm thickness). On the other hand, a single layer of high-pressure W film made by using an NCL step (~165 nm thick) has a low stress value ~50 MPa (off scale and is not shown on Figure 6). This is consistent with the previous studies on the change of stress with the working-gas pressure [14,15].

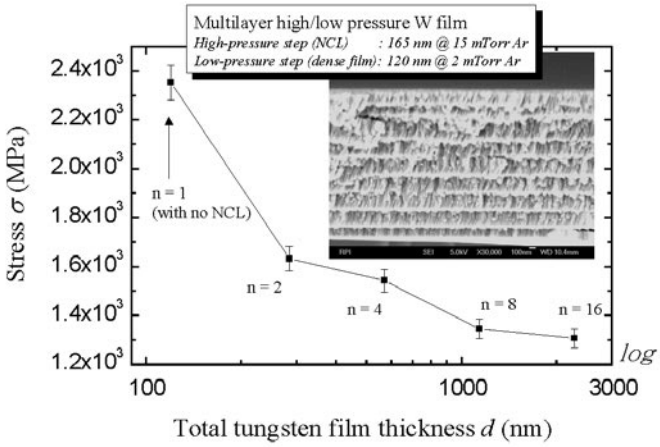

Figure 6: Measured stress values (compressive) of multilayer high/low Ar pressure tungsten films are plotted as a function of total film thickness in a semi-log scale. A multilayer structure starts first with a high-pressure step on the Si wafer. However, the first data point corresponds to a ~120 nm W film at low-pressure. The "n" represents the total number of individual layers. The high-pressure step gives rise to the formation of a nanostructured compliant layer (NCL), while for the low-pressure step we obtained a denser layer with higher stress. The inset shows a cross-sectional SEM image of a ~2,300 nm thick multilayer W film with n = 16. The scale bar is 100 nm.

The multilayer structures formed by these individual layers of high/low pressure have mild stress values (e.g. ~1.30 GPa at ~2,300 nm thickness) as shown in the Figure 6. Interestingly, unlike the single layer W films made under low-pressure, the stress of multilayer film decreases as the total thickness increases. The incorporation of each additional NCL seems to increase the efficiency of compliance in the multilayer film. In addition, the stress seems to level off at higher thicknesses of the multilayer film. This may be due to the competition between the stress buildup with the increase of total film thickness and the relaxation mechanisms associated with the NCLs. At higher thicknesses these two effects can reach an equilibrium state and the stress becomes stabilized. Therefore, NCL used in this way allows us to fabricate very thick films with reasonable low stresses. As an example, the inset in Figure 6 shows a SEM cross-section image of ~2,300 nm thick film, where the multilayer structure can also be realized.

In addition, the crystal structure of W films *with* and *without* NCL and their densities are investigated. Depending on the growth conditions and thicknesses of the films, the sputter deposition of tungsten films can give rise to either the α-phase W, which has the equilibrium bcc structure, or the metastable β-phase W, which has an A15 (cubic) structure, or a mixture of both phases [14,31]. The lattice constants are 3.16 Å and 5.04 Å for α-W and β-W, respectively. These two phases may have very different properties, for example, the measured resistivity of β-W film is an order of magnitude higher than that of the α-W film [32]. Figure 7 compares the XRD plot of a low-pressure single layer W film of ~340 nm thickness (as measured from the non-delaminated region of the wafer) to a multilayer film of high/low pressure of ~2,300 nm thickness. The XRD profiles are very similar for both types of films. The polycrystalline films consist of a mixture of α- and β-phases. However, the dominant α-phase can be realized with the existence of a strong α(110) peak for both the low-pressure and the multilayer high/low pressure W films. Moreover, the position of the XRD α(110) peaks shifted towards smaller 2θ angles from the equilibrium position at 2θ = 40.262°. For example, see the inset in Figure 7 where the peaks at ~39.945° and ~40.159° are for a single layer low pressure and the multilayer high/low pressure W film, respectively. This type of shifts indicates the existence of larger atomic plane spacings, and has been explained to originate from a compressive stress in the film [33]. The location of the α(110) peak for the low-pressure W film (~39.945°) corresponds to a lattice spacing of ~3.189 Å. This is about ~0.79% larger than the equilibrium lattice parameter of an α-W (~3.164 Å) film. On the other hand, the α(110) peak for a multilayer W film shows a smaller shift (~40.159°) that corresponds to a lattice spacing of ~3.172 Å, which is only ~0.25 % larger than the equilibrium lattice spacing. This is consistent with the smaller stress values that we observed in our multilayer W films.

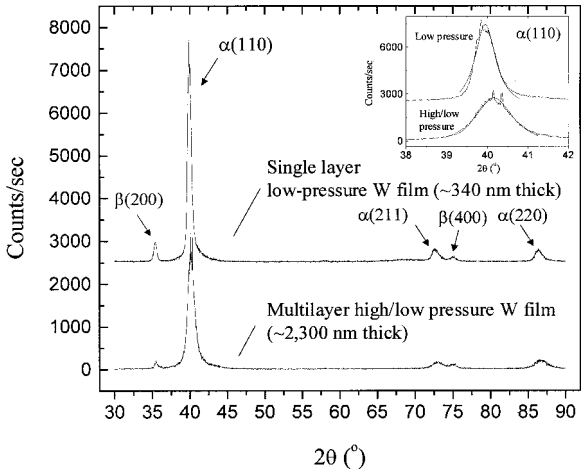

Figure 7: X-ray diffraction (XRD) spectra of a single layer W film made under low Ar pressure and a multilayer W film made under alternating high/low Ar pressures W film are shown. The intensity for the single layer W film spectrum in the y-axis is offset for clarity. The inset is the zoomed in of α(110) peak profiles. Both the experimental peaks (thick line curves) and the smooth line fits (thin line curves) show the peaks shift towards smaller 2θ values due to a compressive stress in these films.

CONCLUSION

In conclusion, it has been shown that a nano-compliant layer formed by the oblique angle sputter deposition or high working gas pressure processing technique can provide stress reduction, adhesion improvement, and a high critical thickness for thin films. The technique is all in situ and the nanostructures are made of the same material as the deposited thin film. This method does not require any lithography steps. The nanostructures have a lower material density and can act as a compliant layer to reduce the stress of the subsequent deposited continuous film. By using this approach we were able to significantly reduce stress values in sputter deposited tungsten films on Si surfaces. Our experimental results agree well with the predictions of a theoretical model that explains the stress relief through the nanostructured compliant layer. These lower stress thin films exhibit stronger adhesions to the substrates thereby avoiding delamination. In addition, by using a multilayer structure made under alternating nanostructured compliant layer and dense continuous film, we obtained very thick W with high structural integrity.

ACKNOWLEDGMENTS

This work is supported by the NSF. We thank D.-X. Ye for taking the scanning electron micrographs of the samples.

REFERENCES

1. C. Creton and E. Papon, "Material Science of Adhesives: How to Bond Things Together," MRS Bulletin, 28, 419, 2003.

2. L.-H. Lee, "Fundamentals of Adhesion", p. 363, Plenum Press, New York, 1992.

3. D.L. Smith, "Thin-Film Deposition: Principles and Practice", pp. 193-200, McGraw-Hill, New York, 1995.

4. K.-D. Lee, E.T. Ogawa, S. Yoon, X. Lu, and P.S. Ho, "Electromigration Reliability of Dual-Damascene Cu/Porous Methylsilsesquioxane Low k Interconnects," Appl. Phys. Lett., 82, 2032, 2003.

5. M.J. O'Keefe and S.E. Stutz, "Stress and Stability of Sputter Deposited A-15 and BCC Crystal Structure Tungsten Thin Films," Mat. Res. Soc. Symp. Proc., 472, 233, 1997.

6. D.C. Meyer, A. Klingner, Th. Holz, and P. Paufler, "Self-Organized Structuring of W/C Multilayers on Si Substrate," Appl. Phys. A, 69, 657, 1999.

7. M.D. Kriese and W.W. Gerberich, "Quantitative Adhesion Measures of Multilayer films: Part II. Indentation of W/Cu, W/W, Cr/W," J. Mater. Res., 14, 3019, 1999.

8. G. Zazzara and I.E. Reimanis, "Residual Stresses in the Failure of W-Pt-Ag Metallizations on Oxidized Si," Surface and Coatings Technology, 111, 92, 1999.

9. H. Maier, J. Luthin, M. Balden, J. Linke, F. Koch, and H. Bolt, "Properties of Tungsten Coatings Deposited onto the Fine Grain Graphite by Different Methods," Surface and Coatings Technology, 142, 733, 2001.

10. T.J. Vink, W. Walrave, J.L.C. Daams, A.G. Dirks, M.A.J. Somers, and K.J.A. van den Aker, "Stress, Strain, and Microstructure in Thin Tungsten Films Deposited by DC Magnetron Sputtering," J. Appl. Phys., 74, 988, 1993.

11. A. Bensaoula, J.C. Wolfe, A. Ignatiev, F.-O. Fong, and T.-S. Leung, "Direct-Current-Magnetron Deposition of Molybdenum and Tungsten with RF-Substrate Bias," J. Vac. Sci. Technol. A, 2, 389, 1984.

12. D.S. Gardner and P.A. Flinn, "Mechanical Stress as a Function of Temperature for Aluminum Alloys Films," J. Appl. Phys., 67, 1831, 1990.

13. R.R. Kola, G.K. Celler, J. Frackoviak, C.W. Jurgensen, and L.E. Trimble, "Stable Low-Stress Tungsten Absorber Technology for Sub-Half-Micron X-Ray Lithography," J. Vac. Sci. Technol. B, 9, 3301, 1991.

14. A.M. Haghiri-Gosnet, F.R. Ladan, C. Mayeux, H. Launois, and M. C. Joncour, "Stress and Microstructure in Tungsten Sputtered Thin Films," J. Vac. Sci. Technol. A, 7, 2663, 1989.

15. H. Windischmann, "Intrinsic Stress in Sputtered Thin Films," J. Vac. Sci. Technol. A, 9, 2431, 1991.

16. J.A. Thornton, "Influence of Apparatus Geometry and Deposition Conditions on the Structure and Topography of Thick Sputtered Coatings," J. Vac. Sci. Technol., 11, 666, 1974; J.A. Thornton, "Influence of Substrate Temperature and Deposition Rate on Structure of Thick Sputtered Cu Coatings," J. Vac. Sci. Technol., 12, 830, 1975; J.A. Thornton, "High Rate Thick Film Growth," Annu. Rev. Mater. Sci., 7, 239, 1977; J.A. Thornton, "The Microstructure of Sputter-Deposited Coatings," J. Vac. Sci. Technol. A, 4, 3059, 1986.

17. R. Rastogi, V. Dharmadhikari, and A. Diebold, "Stress Variation with Temperature/Time and Its Correlation to Film Structure and Deposition Parameters," J. Vac. Sci. Technol. A, 9, 2453, 1991.

18. D.L. Windt, "Low-Stress W/Cr Films for SCALPEL(R) Mask Scattering Layers," J. Vac. Sci. Technol. B, 17, 1385, 1999.

19. T. Karabacak, J.P. Singh, Y.-P. Zhao, G.-C. Wang, and T.-M. Lu, "Scaling During Shadowing Growth of Isolated Nanocolumns," Phys. Rev. B, 68, 125408, 2003.

20. Y.-P. Zhao, D.-X. Ye, G.-C. Wang, and T.-M. Lu, "Novel Nano-Column and Nano-Flower Arrays by Glancing Angle Deposition," Nano Lett., 2, 351, 2002.

21. K. Robbie, M.J. Brett, and A. Lakhtakia, "Chiral Sculptured Thin Films," Nature (London), 384, 616, 1996.

22. R. Messier, A.P. Giri, and R.A. Roy, "Revised Structure Zone Model for Thin Film Physical Structure," J. Vac. Sci. Technol. A, 2, 500, 1984.

23. H.S. Witham, P. Chindaudom, I. An, R.W. Collins, R. Messier, and K. Vedam, "Effect of Preparation Conditions on the Morphology and Electrochromic Properties of Amorphous Tungsten Oxide Films," J. Vac. Sci. Technol. A, 11, 1881, 1993.

24. G.C. Stoney, "The Tension of Metallic Films Deposited by Electrolysis," Proc. R. Soc. London, Ser. A 32, 172, 1909.

25. G. Gille and B. Rau, "Buckling Instability and Adhesion of Carbon Layers," Thin Solid Films, 120, 109 (1984).

26. T. Karabacak, J.J. Senkevich, G.-C. Wang, and T.-M. Lu, unpublished.

27. S. Luryi and E. Suhir, "New Approach to the High Quality Epitaxial Growth of Lattice-Mismatched Materials," Appl. Phys. Lett., 49, 140, 1986.

28. D. Zubia and S.D. Hersee, "Nanoheteroepitaxy: The Application of Nanostructuring and Substrate Compliance to the Heteroepitaxy of Mismatched Semiconductor Materials," J. Appl. Phys., 85, 6492, 1999.

29. D. Zubia, S.H. Zaidi, S.R.J. Brueck, and S.D. Hersee, "Nanoheteroepitaxial Growth of GaN on Si by Organometallic Vapor Phase Epitaxy," Appl. Phys. Lett., 76, 858, 2000.

30. Y.G. Shen, Y.W. Mai, Q.C. Zhang, D.R. McKenzie, W.D. McFall, and W.E. McBride, "Residual Stress, Microstructure, and Structure of Tungsten Thin Films Deposited by Magnetron Sputtering," J. Appl. Phys., 87, 177, 2000.

31. T. Karabacak, A. Mallikarjunan, J.P. Singh, D. Ye, G.-C. Wang, and T.-M. Lu, "Beta-Phase Tungsten Nanorod Formation by Oblique-Angle Sputter Deposition," Appl. Phys. Lett., 83, 3096, 2003.

32. K.Y. Ahn, "A Comparison of Tungsten Film Deposition Techniques for Very Large Scale Integration Technology," Thin Solid Films, 153, 469, 1987.

33. I.C. Noyan, T.M. Shaw, and C.C. Goldsmith, "Inhomogeneous Strain States in Sputter Deposited Tungsten Thin Films," J. Appl. Phys., 82, 4300, 1997.

Internal ICP Assisted Magnetron Sputtering for Fast Deposition at Low Pressure (10^{-4} mbar range) in Semi Industrial Coating Chamber (0.1 m^3)

C. Nouvellon, J.P. Dauchot, Y. Paint, F. Monteverde, and M. Hecq,
Materia Nova, Mons, Belgium

Key Words: Ion assisted deposition; Sputter deposition; Reactive deposition; Electronic microscopy

ABSTRACT

Adding between the magnetron source and the substrate a rectangular RF coil slightly larger than the target (450 x 150 mm^2) makes it possible to create a secondary inductively coupled plasma in front of the target. This latter raises the ionization rate and allows it to work at lower pressure (in the 10^{-4} mbar range). At this pressure the collision frequency is reduced. Therefore: i) the species ejected from the target impinge the substrate with more energy so that compact films are obtained, ii) as there is less backscattering the deposition rate increases.

Metallic Titanium and Titanium oxide have been deposited on various substrates in this range of pressure by DC sputtering of a metallic Titanium target in pure Argon for the metallic films and in a mixture of Argon-Oxygen in the reactive mode for the oxide films.

Plasma diagnostics are operated by mass spectrometry and optical emission spectrometry. The films are observed by SEM and TEM and characterized by electron diffraction.

INTRODUCTION

Magnetron sputtering is widely used because of its good film quality and the large field of applications such as ornamental, mechanical or high technological purposes. Amplified plasma are of great interest to increase the range of applications. Ionized plasma can be used to cover complex substrate and increase film homogeneity and quality. A RF coil powered at 13.56 MHz frequency can be used to create an ICP (inductively coupled plasma) secondary plasma. The ionization rate is the highest for pressure at around 30 mTorr [1]. At lower pressure, the effect on the plasma consists mainly in more excited species [2]. The RF coil are usually circular with one [3-5] or few turns [6-8], with 10 or 15 cm in diameter. The innovating aspect of our system is that we have made a bigger rectangular coil, with dimensions slightly larger than the target (450 x 150 cm^2). We have used this coil to amplify the plasma at very low pressure, in the range of 10^{-4} mbar.

EXPERIMENT SETUP

The coating chamber is an industrial system (TSD 400-CD HEF R&D) with various diagnostic facilities such as optical emission and mass spectrometers. The pumping system consists of a primary mechanical pump with 40 m^3h^{-1} pumping speed (Leybold) and a high pressure turbomolecular pump with 1000 ls^{-1} pumping speed (Varian turbonavigator) for the high vacuum pumping step. This pump is protected by baffles and a valve can be closed to keep the pumping on when venting the chamber.

The internal dimensions of the vacuum chamber are 400 x 400 mm^2 with an internal height of 600 mm leading to a volume of 0.1 m^3. The experiment setup is described in Figure 1. The cathode is placed vertically in one door of the chamber. The titanium target area is 450 x 150 mm^2 and 8 mm thick. The opposite door of the machine can be equipped with another cathode, but in this case it is replaced by a Plexiglas window in order to observe the plasma. The target is sputtered in DC mode with a ENI RPG 100 generator. The maximum power is 10 kW with a maximum voltage of 800 V.

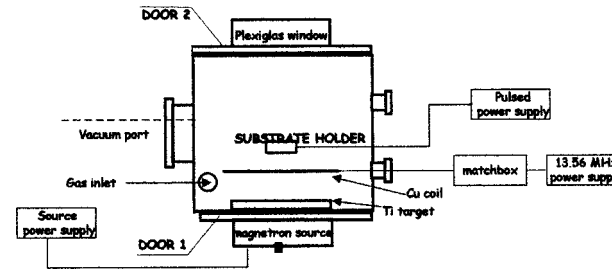

Figure 1: Experiment setup.

The induction coil, made of a copper tube (inside diameter 12 mm, 1 mm thick) is grounded and placed 7 cm away from the cathode. Two coaxial tubes are used to allow water circulation for cooling. It is powered at 1 kW by a 13.56 MHz RF generator (Huttinger PFG 250). In order to minimize the reflected power, a matching netbox (Huttinger RF matchbox PFM 3000A) is connected between the coil and the RF generator.

 505/856-7188 ISSN 0737-5921
47th Annual Technical Conference Proceedings (April 24–29, 2004) Dallas, TX USA

The substrate holder, parallel to the target, is 13 cm from the target. It is 8 cm large and 30 cm high so that four 5 x 5 cm^2 or 6 x 6 cm^2 substrates can be coated in the same conditions. It can be biased in pulsed mode (250 kHz frequency with a 1056 ns pulse positive part) with a ENI RPG 50 generator for etching and target cleaning before coating or substrate biasing during deposition. The substrates are glass or steel.

RESULTS AND DISCUSSION

Low Pressure Measurements

The working pressure is determined by the argon flow, given in sccm by the mass flow controller, calibrated for nitrogen. The TSD400 software limits the capacitance gauge pressure reading at 10^{-3} mbar, obtained with 15 sccm of argon gas. In order to determine the pressure for lower argon flow, we have extrapolated to lower values the linear relation between argon flow and pressure (Figure 2).

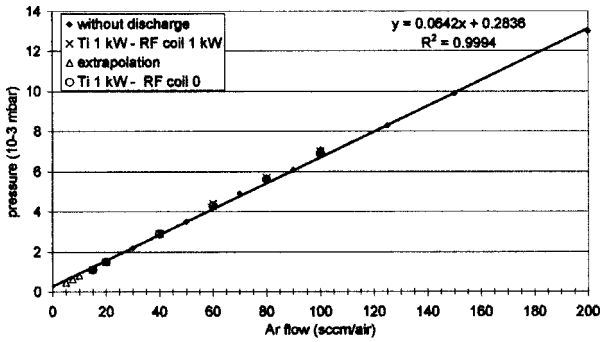

Figure 2: Pressure versus argon flow.

In this figure, we have reported the pressure measured without discharge, with DC discharge only, and both DC and RF discharges. For a fixed argon flow, the pressures obtained are the same in these three conditions, indicating that there is no Ar gas rarefaction effect as seen elsewhere [9]. Using the RF coil allows work at lower pressure. The lowest calculated pressure is 2.5 10^{-4} mbar (for 2 sccm argon gas). It is not possible to introduce lowest flow with our mass flow controller. For the same DC power on the Ti target (1 kW), the discharge breaks down below 4.2 sccm (4.2 10^{-4} mbar calculated) because the highest voltage on the target is achieved.

Plasma Potential Versus Cathode Power

The titanium target has been sputtered with 10 sccm argon gas flow (8.1 10^{-4} mbar calculated) varying the DC power applied to the cathode from 1 to 5 kW. The RF coil is powered with 1 kW. The plasma potential has been measured with the mass spectrometer, as the potential corresponding to the maximum intensity on the titanium ion energy distribution function. The plasma potential decreases from 70 V to 28 V when the DC power increases from 1 to 5 kW. When the DC power increases, the titanium sputtering rate and electronic density increases and the plasma potential decreases. The plasma potential remains higher than typical values of few V obtained for DC magnetron discharge [10].

Titanium Depositions

Various titanium depositions on glass and steel have been operated, always with the same power on the target (1 kW) and duration (30 minutes). Two coatings were realized with 5 sccm argon flow (5 10^{-4} mbar) and 0 or 1 kW on the RF coil. For comparison, the third deposition was realized at higher pressure (30 sccm Ar, 2.2 10^{-3} mbar) which are the commonly used conditions in magnetron sputtering. A pulsed bias of -50V is applied on the substrate holder. The corresponding current on the substrate holder, shown in Table 1, is an indication for the number of ions impinging on the substrate. These coatings on steel are observed by Secondary Electron Microscopy (SEM) and the coatings on glass by TEM (Transmission Electron Microscopy). These observations also allow us to measure the coating thickness, reported in Table 1.

The sputtering is operated in the power regulation mode. The power is fixed to 1 kW. The target current variations are due, with 5 sccm Ar, to the RF coil plasma influence. Without power on the RF coil, increasing the argon flow from 5 to 30 sccm induces an increase of the target current but does not change the deposition rate. Using the RF coil raises the deposition rate, which is the highest in this case. The current on the substrate holder is higher than in the other cases (0.35 A versus 0.08 A and 0.05 A). The plasma potential is also higher and the ions impinge the substrate with more energy. This induces dense films but with lots of stresses. The SEM image (Figure 3a) shows a dense coating with a smoother surface than with no RF power (Figure 3b). For comparison, the coating realized at 30 sccm with no RF has a rougher surface (Figure 3c).

Table 1: Sputtering conditions and coating thickness measurements (Ti target power 1 kW, substrate bias voltage -50 V).

Ar flow sccm	Pressure 10^{-3} mbar	Target current A	RF coil power kW	Substrate current A	Coating thickness µm
5	0.5	2.14	1	0.35	1.5
5	0.5	1.93	0	0.08	1.0
30	2.2	2.90	0	0.05	1.1

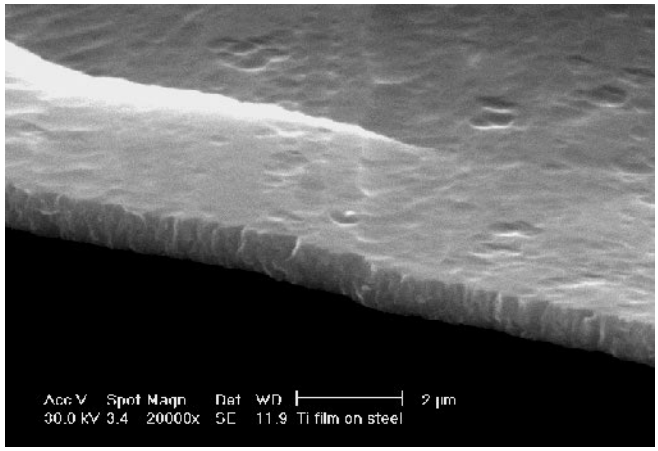

a.

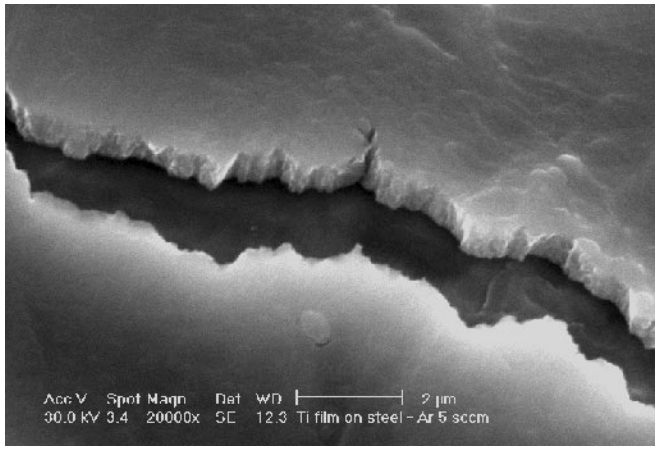

b.

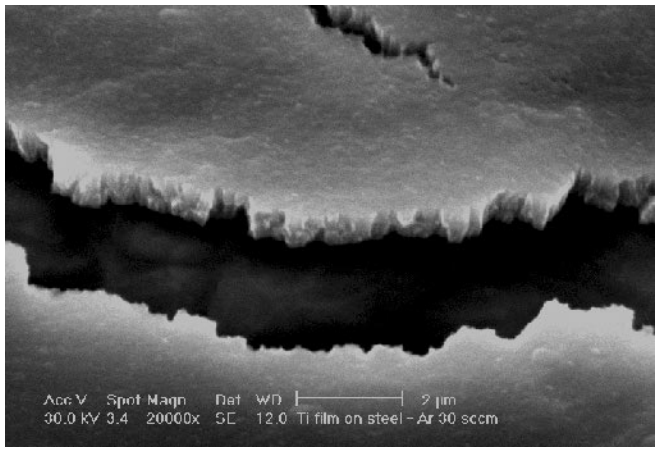

c.

Figure 3: SEM observations of Ti coating realized with: a) 5 Ar sccm with the RF coil; b) 5 Ar sccm with no RF power; and c) 30 Ar sccm with no RF power.

For TEM observations, 50 nm thick cross sections of the coated substrate (for RF coil deposition) were obtained using an ultra-microtome system. Figure 4 shows a cross section micrograph of the Ti film indicating a fibrous growth structure. As expected, the film thickness reaches 1.5 µm. The ring diffraction pattern in Figure 5 demonstrates the polycristalline structure of the Ti film. The theoretical diffraction pattern expected for a polycristalline Ti film is added to the experimentpattern. Concerning (011) and (002) rings, we can observe an inhomogeneous intensity, indicating a slight preferential orientation of the grains in the film.

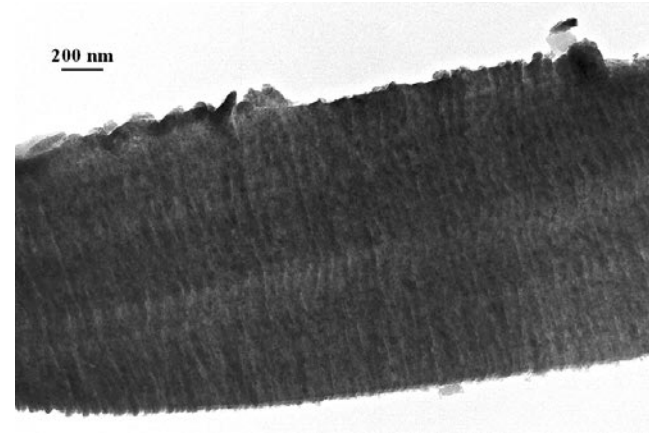

Figure 4: TEM observation of Ti coating realized with 5 Ar sccm with the RF coil.

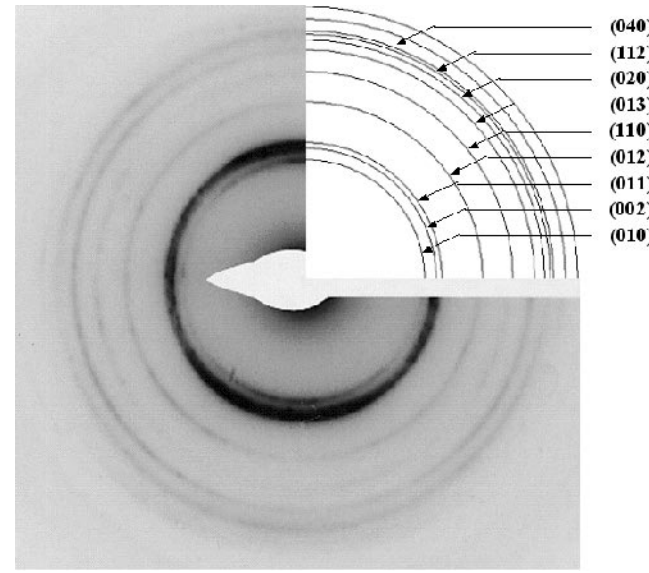

Figure 5: TEM electron diffraction pattern of Ti coating realized with 5 Ar sccm with the RF coil.

CONCLUSION

We have designed a rectangular RF coil slightly larger than the target (450 x 150 mm^2). The secondary inductively coupled plasma allows for work at lower pressure. In the same pressure and power conditions, the deposition rate is increased when using the RF coil. Observations by Electron microscopy show that the film is denser and smoother when the RF coil is powered. Films realized at higher pressure (2.2 10^{-3} mbar) without RF coil are rougher and less dense.

ACKNOWLEDGMENTS

We are very grateful for the financial support from "Region Wallonne" and European Community (FEDER) in the frame of "Pôle d'Excellence Materia Nova".

REFERENCES

1. A. Ricard, C. Nouvellon, S. Konstantinidis, J.P. Dauchot, M. Wautelet, and M. Hecq, J. Vac. Sci. Technol. A, 20 (4), 1488, 2002

2. C. Nouvellon, S. Konstantinidis, J.P. Dauchot, M. Wautelet, P.Y. Jouan , A. Ricard, and M. Hecq, J. Appl. Phys., 92-1, 32, 2002

3. M. Yamashita, Y. Setsuhara, S. Miyake, M. Kumagai, T. Shoji, and J. Musil, Jpn. J. Appl. Phys., 38, 4291, 1999

4. K. Nakamura, Y. Kuwashita, and H. Sugai, Jpn. J. Appl. Phys., 34, L1686, 1995

5. S.M. Rossnagel, Thin Solid Films, 263, 1, 1995

6. M. Yamashita, J. Vac. Sci. Technol. A, 7 , 151, 1989

7. J.E. Foster, W. Wag, A.E. Wendt, and J. Booske, J. Vac. Sci. Technol. B, 16 (2), 532, 1998

8. C. Ducros, V. Benevent, P. Juliet, and F. Sanchette, Surf. Coat. Technol., 163-164, 641, 2003

9. S.M. Rossnagel, J. Vac. Sci. Technol. B, 16(6), 3008, 1998

10. S. Konstantinidis, C. Nouvellon, J.P. Dauchot, M. Wautelet, and M. Hecq, Surf. Coat. Technol., 174-175, 100, 2003

Vacuum Deposition of Thick Multilayers on Thin Flexible Polymer Substrates

N. Magriotis, Arcotronics Nissei Group, Sasso Marconi, Italy; and G. Comini, Department of Energy and Fluid Machinery, University of Udine, Italy

Key Words: Film thickness; Thermal evaporation; Web coating thermal modeling; Sputter deposition

ABSTRACT

Vacuum coating processes are among the most efficient technologies available for the deposition of metallic layers on polymer substrates. In particular, web equipment employing thermal evaporation and sputter processes in the same line allow the deposition of two layers of very different thickness during one single passage. In this way the final quality of the product is significantly improved since the web is unwound and rewound only once. As sputter deposition requires web speeds of a few meters per minute, the in-line evaporation process deposits very large amounts of material on the substrate.

Depositing thick coating layers on thin polymer films by thermal evaporation is a very challenging task because of the extremely high thermal load induced into the substrate. This paper investigates, both experimentally and theoretically, the possibility of depositing thick copper and aluminium layers of good quality on thin plastic webs by thermal evaporation with a subsequent in-line sputter deposition. All tests have been carried on in a vacuum web coater especially designed and built for the development of new products. Prediction of substrate temperature behavior has been made possible by using a new web coating thermal model. Theoretical and experimental results have been favorably compared under different operating conditions.

INTRODUCTION

Thin substrates carrying a thick multilayer deposit of metals are products of great interest for the electronic industrial environment. The possibility of manufacturing these products in a vacuum web coater could open new opportunities in the world of vacuum metallized flexible substrates. On the other hand, this application represents a relatively difficult challenge. The key to success depends on the ability of handling thermal sensitive films during vacuum coating processes under very severe thermal conditions.

The aim of this paper is to illustrate the theoretical and experimental researches in this field that have been carried out by Arcotronics with the cooperation of the University of Udine. In particular, the critical combination of a very thin substrate with a very thick coating layer has been investigated. First an analytical model of the web has been formulated to predict the thermal behavior of the film under the very high rates of heat flow associated with metal condensation and thermal radiation. In this way, besides the clear identification of the experimental conditions, it has been possible to introduce suitable modifications to the process that have increased the overall performance of the web coater. The analytical model has then been verified by several experiments in which thermal evaporation and sputter deposition have been taking place simultaneously in a dedicated vacuum roll-to-roll web coater. Finally, the experimental web coater has been used to run some pilot pre-productions which are particularly appreciated in the industrial environment since they offer the chance of reducing financial risks involved in the acquisition of new machines for innovative products.

The products investigated have been a few micrometers thick polymer webs with copper or aluminum coating layers of some hundreds nanometers of thickness plus additional metal top-coating layers of several nanometers of thickness. Copper and aluminum have been evaporated by ceramic crucibles, while the subsequent metals have been deposited by means of sputter deposition. Several quality tests have been conducted on the final product. Among them, it is worth mentioning peel-off tests for adhesion, measurements of surface energy, measurements of the thickness of deposited layers, and microscope observations.

WEB THERMAL MODEL

Preliminary Considerations

The deposition of a metal by thermal evaporation with a web speed of a few meters per minute is a very challenging task. The thin substrate is extremely stressed by the very high heat loads associated with the deposition of the thick coating layer and the exposition to the thermal radiation from the crucibles. To predict the thermal behavior of the film during metallization processes a *zero-order* and a *first-order* analytical model have been introduced. Both models are one-dimensional since the film thickness is several orders of magnitude smaller than the other two dimensions (width and length). As a consequence, axial and transverse conduction effects are neglected. Furthermore, both models take into account the main parameters of the process such as the web speed, the deposition rate

 505/856-7188 ISSN 0737-5921
47th Annual Technical Conference Proceedings (April 24–29, 2004) Dallas, TX USA

and the radiation load. Consequently, both models could be satisfactorily used in the preliminary selection of experiments that were likely to produce coated webs of acceptably good quality. The only difference between the two models is that the *zero-order* one disregards the effect of thermal capacity of the substrate. Consequently, thermal equilibrium is assumed to be reached instantaneously and, at any position along the line, local heat transfer processes are considered steady. On the contrary, the *first-order model* takes into account the thermal capacity of the substrate, and the ensuing heat transfer processes are considered to depend on time, i.e. on position along the line.

Zero-Order Model

In the *zero-order model* the one-dimensional heat transfer processes are assumed to be steady. Additional assumptions are as follows. The drum temperature is considered to be equal to the temperature t_f of the refrigerant fluid. The total temperature difference $\Delta t = t_1 - t_f$ is unknown but is related to the total specific heat flux by the relationship:

$$q'' = \frac{\Delta t}{R''}$$

Equation 1

In the schematic shown in Figure 1, R'' is the total specific thermal resistance (sum of the two conduction resistances of the coating layer and the substrate, and the thermal resistance between web and drum). In particular, the effective heat transmission coefficient α through the gap between film and drum is obtained by suitably combining the two parallel heat flow contributions of conduction through the contact zones and of convection through the gap itself. Because of the small contact area, we have

$$\alpha \cong \alpha_s + \alpha_g$$

Equation 2

where α_s is the inverse of the specific contact resistance and α_g is the convection transmission coefficient. The contact resistance depends on the average contact pressure and, consequently, on the web tension [1]. A good fit with experimental results has been obtained by setting α_s equal to the constant value of 100 W/m^{2}K. The convection coefficient has been estimated as [2]

$$\alpha_g = \frac{\lambda_g}{s_g + 2l}$$

Equation 3

where s_g is the average gap thickness and l is the mean free path of the molecules (that depends on the saturation pressure of the vapor). Again, a good fit with the experimental results has been obtained by evaluating the pressure at the temperature t_f of the cold wall.

Finally, the total specific heat flux is computed as sum of deposition and thermal radiation contributions

$$q'' = q''_d + q''_r$$

Equation 4

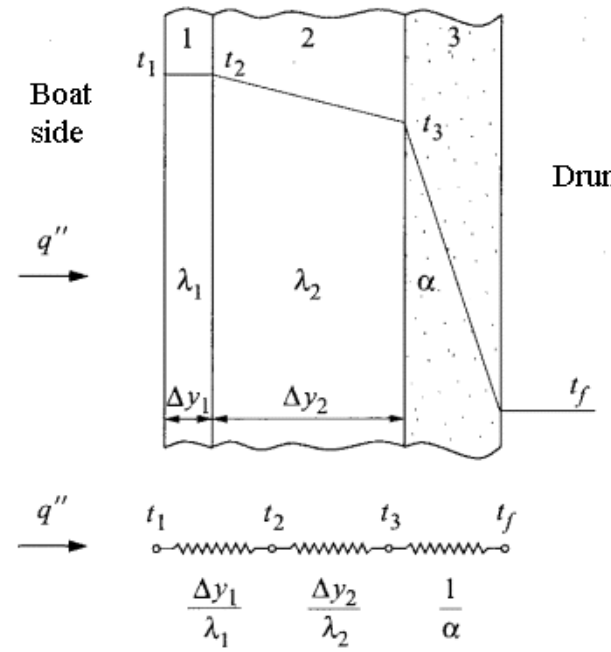

Figure 1: Heat flow model. 1: coating layer; 2: web substrate; 3: interface between web and drum.

The deposition load is evaluated as

$$q''_d = \dot{m}''_v \left(h_v - h_s \right)$$

Equation 5

where $\dot{m}''_v$ is the specific mass flow rate of vapor condensed on the web surface, h_v is the enthalpy of the vapor at the crucible temperature, and h_s is the enthalpy of the deposited metal at the web temperature. The radiation load is evaluated as

$$q''_r = \varepsilon_s \varepsilon_c F \, \sigma \left(T_c^4 - T^4 \right)$$

Equation 6

where ϵ_s is the emissivity of the deposited metal, ϵ_c is the emissivity of the crucible, F is a view factor, σ is the Stefan-Boltzmann constant, and T_c and T are the absolute temperatures of the crucible and the web respectively.

First-Order Model

In comparison to the *zero-order model*, in the *first-order model* the only additional assumption concerns the web thermal capacity which is no longer neglected. Consequently, with reference to a traveling Lagrangian frame, it is possible to say that the temperature of a web element changes with the time ϑ coordinate. Alternatively, with reference to an Eulerian frame, we can say that the local temperature depends on the space coordinate x. We have:

$$x = x_0 + u\,\vartheta$$

Equation 7

where u is the web velocity.

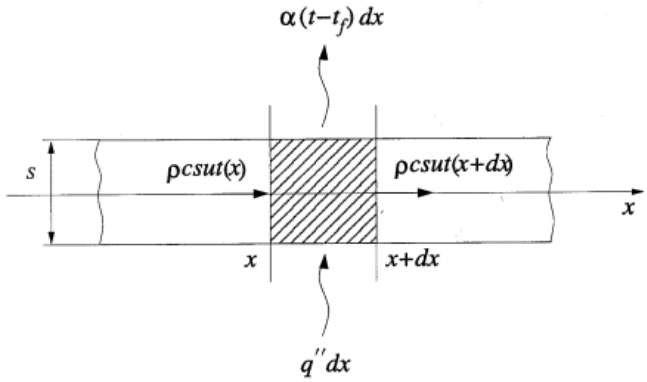

Figure 2: Schematic of the element energy balance.

As shown in Figure 2, we can write the following energy balance for the element dx at the representative temperature t (averaged across the web thickness):

$$\rho c s u t(x) + q'' dx = \rho c s u t(x+dx) + \alpha(t - t_f)dx$$

Equation 8

Since it is

$$t(x+dx) = t(x) + \frac{dt}{dx}$$

Equation 9

by simple algebraic manipulations we obtain the governing differential equation

$$\rho c s u \frac{dt}{dx} = q'' - \alpha(t - t_f)$$

Equation 10

Equation 10 is a first-order differential equation whose solution can be written in dimensionless form as

$$\frac{t - t_0}{t_0 - t_f} = \exp\left(-\frac{x}{L_0}\right)$$

Equation 11

In Equation 11, t_0 is the temperature at the coordinate x = 0, where the heating process begins, and

$$L_0 = \frac{\rho c s u}{\alpha}$$

Equation 12

is the characteristic length of the process.

EXPERIMENT VALIDATION

Experimental Apparatus

All trials have been conducted using a vacuum web coater designed and manufactured by Arcotronics with the specific purpose of developing new products in the metallization field. As shown in Figure 3, the machine is a versatile two-drum metallizer with a lot of optional flanges that can accommodate different equipment, such as pre- and post-web-treaters, an in-line pattern printing system, an oil evaporator for free-margin tracing, a coating layer thickness monitoring system, etc.

All the tests illustrated in this paper have been conducted with the following machine configuration. The four-component ceramic boats equipped with metal wire feeding systems are placed under the first process drum. A system of mechanical pumps, a diffusion pump and a cryopump, creates the vacuum in the corresponding machine area. In this way the working pressure of 4 x 10^{-4} mbar is quickly reached and safely maintained. A magnetron for sputter deposition has been located in a stainless steel chamber served by a dedicated turbomolecular pump. This configuration, having a particularly accurate vacuum separation, allows the sputtering area to reach a vacuum of the order of 10^{-6} mbar in a few minutes during the pre-cleaning phase. Process pressure is then in-

creased to the 10^{-3} - 10^{-2} mbar range by the emission of a controlled flow of argon. Both the pre-cleaning stage and the sputter deposition process can be carried on without influencing the vacuum level of the rest of the metallizer chamber. The web tension is monitored by three couples of load cells. The maximum web width is 350 mm. Five independent motors drive each process drum, the tension roller, the unwinder reel and rewinder reel. The web speed can be selected between two different ranges: a low-range (0,5-25 m/min) and a high-range (50-800 m/min). Particular care has been taken to ensure the accuracy of the rewinding process. As a matter of fact, the last roller can work in lay-on mode with contact pressure adjustment or in gap-mode. These two alternatives can be selected in order to obtain the best rewinding accuracy on the final reel.

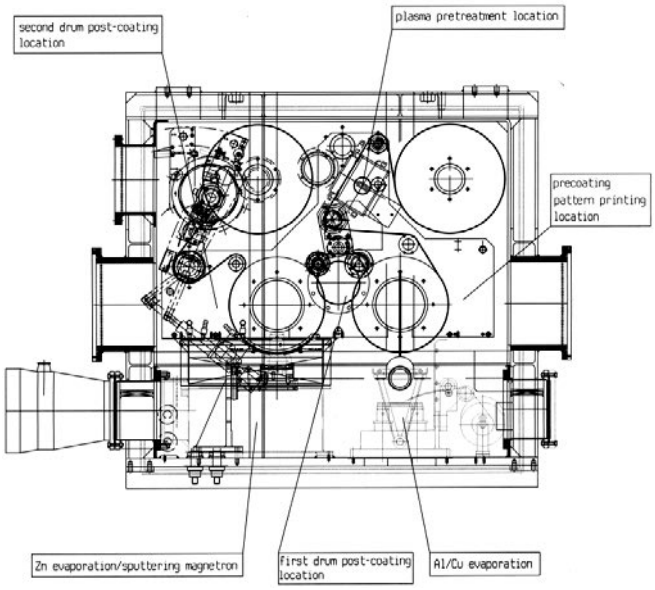

Figure 3: Layout of laboratory web coater.

Analytical and Experimental Findings

As already pointed out, the analytical model has been first used to find out which web speed should be selected in order to minimize the heat load on the substrate. Both analytical and experimental results have demonstrated that for any given thickness of the coating layer the lowest web velocity minimizes thermal stresses. You can deposit the same amount of material at different web speeds by suitably adjusting the wire speed, but the maximum temperature reached by the substrate during the metallization process increases as web speed increases. As an example, an average thickness of the coating layer of 400 nm can be obtained by using the two different combinations of wire and web speeds reported in Table 1, with suitably identical settings of all the other machine parameters.

Table 1: Comparison of two different situations modeled analytically.

Substrate	Evaporated material	Wire speed	Web speed
PET 19 μm	copper	31 cm/min	5,7 m/min
PET 19 μm	copper	22 cm/min	3,5 m/min

In such a case, the thermal model has predicted the two different temperature profiles shown in Figures 4 and 5, respectively. It must be noted that the test with higher wire speed was modeled with hotter crucibles. According to the experience of the ceramic boats manufacturer [3], hotter crucibles produce more vertically-oriented vapor flows that induce a few percent increase in the metallization efficiency.

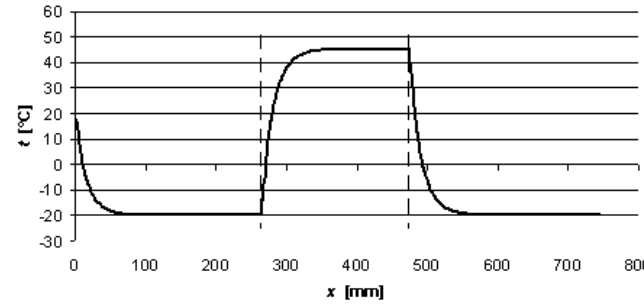

Figure 4: Test run at 5,7 m/min of web speed and 31 cm/min of wire speed.

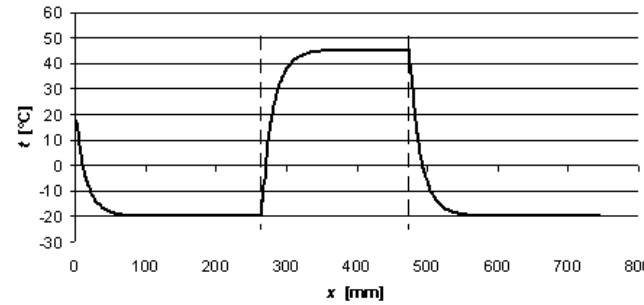

Figure 5: Test run at 3,5 m/min of web speed and 22 cm/min of wire speed.

In Figures 4 and 5, the axial coordinate x indicates web path distance around the coating drum (x = 0 at the entrance point; metallization takes place in the space interval between the two dashed vertical lines). Considering that thermal stresses increase with the difference between the maximum average temperature t of the substrate and the temperature t_f of the drum (equal to -20°C in the present case) it is evident that the substrate is subjected to lower thermal stresses when the web speed is lower.

Experimental trials have confirmed these findings. What we observed is that during tests at higher speed it was necessary to increase the web tension in order to obtain the same quality of the final product. Conversely, if trials at higher line speeds were performed using the same web tension suitable for lower speed, occasional wrinkles were observed through the metallizer window. Only by increasing the web tension did the wrinkles disappear.

The analytical model has then been used to predict the maximum temperature reached by even thinner substrates carrying the same metal coating. It has thus been found that the web temperature profile *t(x)* doesn't practically depend on the web thickness, even if the thickness is reduced to a few micrometers, provided that the equivalent heat transmission coefficient α between drum and web doesn't change. Conversely, even small variations of α induce great variations in web temperature profiles. Comparison of temperature profiles obtained for $\alpha = 100$ W/m^{2}K and $\alpha = 75$ W/m^{2}K are presented in Figures 6 and 7 respectively.

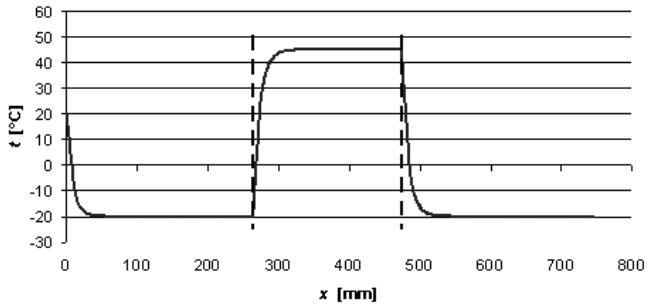

Figure 6: Substrate 10 μm thick, web speed 3,5 m/min, copper wire speed 22 cm/min, $\alpha = 100$ W/m^{2}K.

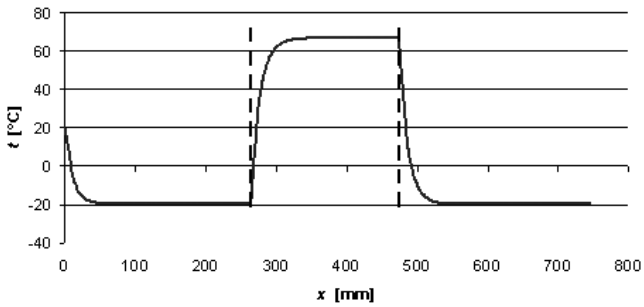

Figure 7: Substrate 10 μm thick, web speed 3,5 m/min, copper wire speed 22 cm/min, $\alpha = 75$ W/m^{2}K.

All trials have confirmed that the same final quality is obtained as long as the absolute web tension is maintained. The explanation is that α depends mainly on the gap thickness and the contact pressure, i.e. on the absolute web tension. On the other hand reasons of mechanical resistance connected with the increase of the specific tension might not permit that the same absolute tension can be maintained when the substrate thickness decreases too much. In particular, it has been verified that the same tension cannot be kept when the web thickness is decreased from 19 μm to 10 μm without changing the material type. The data in Table 2 shows that the specific tension should increase from 18 to 34,2 N/mm^2 in order to have the same absolute tension of 342 N/m. Conversely in order to have the same specific tension of 18 N/mm^2 the absolute tension should decrease from 342 to 180 N/m. In this latter case, both analytical model and experimental trials have indicated that the heat transmission coefficient α and the cooling effect of the substrate decrease significantly.

Table 2: Absolute tension and specific tension.

Substrate	Absolute tension	Specific tension
PET 19 μm	342 N/m	18 N/mm^2
PET 10 μm	342 N/m	34,2 N/mm^2
PET 10 μm	180 N/m	18 N/mm^2

Most of the trials have been performed using thermal evaporation and sputter post-deposition, one after the other, on the same line. However, it has been found that the sputter top deposition of a metal layer of up to 20 nm of thickness has a negligible influence on the thermal behavior of the substrate. It is also worth mentioning that the web quality remains good since both thermal evaporation and sputter deposition take place during a single unwinding and rewinding process.

CONCLUSIONS

The development of new processes that try to overcome the boundaries of the known or try to go beyond the standard industrial practice always requires great efforts. This paper has illustrated the steps undertaken by Arcotronics in the development of vacuum deposition of thick multilayers of metals on thin flexible polymer substrates. The experimental trials have been designed on the basis of an analytical model developed by the University of Udine. Combination of theory and practice has allowed us to reach the final objective in a relatively short time, overcoming difficulties that seemed to prevent any practical implementation. Furthermore, a great deal of additional knowledge on metallization processes that has been collected during this research will help in the design and manufacture of new vacuum web coaters.

REFERENCES

1. F.P. Incropera and D.P. Dewitt, Fundamentals of Heat and Mass Transfer, Wiley, New York, 1986.
2. R.B. Bird, W.E. Stewart, and E.N. Lightfoot, "Transport Phenomena", Wiley, New York, 1980.
3. Sintec Keramik, Technical Reports, Sintec Keramik, Halblech, Germany, 2001.

Modeling of the Film Thickness Distribution Along Transport Direction in In-line Coaters for Reactive Sputtering

A. Pflug and B. Szyszka, Fraunhofer Institute for Surface Engineering and Thin Films IST, Braunschweig, Germany; and M. Geisler, A. Kastner, C. Braatz, U. Schreiber, and J. Bruch, Applied Films GmbH & Co. KG, Alzenau, Germany

Key Words: Reactive sputtering deposition; Gas flow simulation; Vacuum system instrumentation and control; Simulation of the plasma impedance

ABSTRACT

For large area architectural coatings such as Low-E or solar control systems strong demands on color uniformity are to be fulfilled. Typically, a precision of $\Delta a^*, \Delta b^* < \pm 1$ is required. For single-Ag based Low-E coatings this implies a film thickness tolerance of about ±2%, while for double or multi-Ag low-E coatings the thickness variation should be less than ±1%.

A common problem of in-line sputter coaters is a certain film thickness deviation of about 2% along the glass transport direction. It is caused by varying flow conditions due to the glass substrate movement within the compartments. In order to solve this problem, we performed a three dimensional Monte Carlo gas flow simulation of a jumbo sized sputter compartment together with adjacent pumping compartments and glass transport slots. The sputter compartment comprises two 3.83 m sized twin rotatable magnetrons equipped with Zn-targets.

Based on the Monte Carlo simulation, a heuristic model of the reactive ZnO sputtering process has been implemented. Experimental verification shows that this model properly describes (i) the pressure with respect to substrate position, (ii) the ZnO target voltage vs. oxygen flow characteristics at different conditions as well as (iii) the film thickness profile on a substrate after dynamic deposition. This model is a starting point towards novel controlling algorithms which allow for film thickness homogeneity better than 1% within jumbo sized in-line sputtering coaters.

INTRODUCTION

Reactive sputtering of coatings for architectural glass on jumbo sized substrates is a challenging task due to strong demands on the throughput and the color uniformity of the resulting products. While a film thickness homogeneity of about ±1% is required, the reactive sputter process is influenced by multiple quantities: (i) the gas pressure deviation along target axis, (ii) the magnetic field distribution of the cathodes, (iii) the interaction of the discharge zone with anodes, (iv) the surface oxidation distribution along the target axis, and (v) time-dependent process modulations due to substrate movement.

The quantities (i)-(iv) influence the film thickness profile in y-direction, i.e. along the target axis, while time-dependent process fluctuations (v) lead to thickness deviations in x-direction, i.e. the transport axis.

Thickness variations in y-direction are usually compensated with multifold gas inlet systems. In some cases, an additional controlling cycle is required, e.g. if the target oxidation profile along y-direction is not stable. For a flat film thickness profile along target axis, only a certain stationary profile of the gas pressure has to be maintained which thus can be determined empirically.

However, process fluctuations induced by substrate movement are time-dependent and thus a time-dependent compensation will be required to maintain a flat film thickness profile along x-direction. This compensation will further be dependent on the material and working point of the sputtering process, the geometry of the substrate and the substrate transport system as well as on conditions within neighboring sputtering compartments. Hence it is not feasible to empirically determine time-dependent compensation schemes for the film thickness profile in x-direction.

For this reason, in a cooperation between Applied Films and Fraunhofer IST, a simulation model of the dynamic deposition process in jumbo sized in-line sputter coaters has been implemented. This model is able to predict the film thickness profile in x-direction and will be subsequently used to design time-dependent compensation algorithms. This paper shows the implementation details of this model as well as experimental verification with regard (i) to pressure fluctuations due to substrate movement, (ii) reproduction of characteristic target voltage vs. gas flow curves of the reactive ZnO process and (iii) the resulting thickness profile in x-direction after dynamic deposition.

MODEL OF AN IN-LINE SPUTTER COATER

Experiment Setup

The experiments and simulations reported in this paper are related to an in-line coater installed at Applied Films called "BigMag". This multi-pass coater comprises eleven compartments M1...M11 of 4.35 m width and is mainly used for

 505/856-7188 ISSN 0737-5921

47th Annual Technical Conference Proceedings (April 24–29, 2004) Dallas, TX USA

testing of novel sputtering sources. Due to the limited number of compartments the maximum substrate size is 3.21 x 1.0 m^2, i.e. the full width of jumbo sized glass sheets but only a length of 1 m instead of 6 m in transport direction.

Figure 1 shows a cross section view of modules M5-M11, whereof module M9 contains two Twin rotatable Zn targets which are connected to an MF power supply "Advanced Energy Crystal™". The load lock is located on the right side near M1, while M11 is an empty compartment where the transport direction of the substrate is changed. The gas inlets in M9 are located beneath two shieldings on both sides of the targets. On each side is a uniform "main gas" inlet and a seven-fold segmented "tuning gas" tube.

Each compartment comprises two transport rolls shown in the lower region of Figure 1. These rolls are massive cylinders, a small gap between the rolls and the glass substrate is maintained by rubber belts mounted on distinct locations on the rolls. The rolls are separated from the bottom by a small gap. To avoid deposition on the compartment bottom, shieldings are installed between each pair of transport rolls. The connections between the compartments below the substrate plane are narrowed by T profiles, however a considerable gas exchange remains.

Modules M8 and M10 act as pumping compartments which are equipped with three Leybold 1600 turbo pumps, respectively. The connection between M9 and M8/M10 is via 20 rectangular orifices on either side in the upper region, while the connection between the pumping and the glass transport slot in the lower region is completely blocked in M8 and M10. The upper volume of M10 is, however, indirectly connected to the transport slot via module M11 while the upper right side of module M8 is closed.

Gas Flow Simulation

The gas flow simulation software developed at Fraunhofer IST is based on the "Direct Simulation Monte Carlo" (DSMC) algorithm of Bird [1]. This software operates in three-dimensional recipient geometries which can be assembled from an arbitrary number of rectangular boxes. It uses multiple tasks for parallel computation, a load balancing step assigns the rectangular boxes to the parallel tasks in a manner that (i) an almost homogeneous load distribution is established and (ii) the number of flow connections over the network switch is minimized.

The DSMC calculations for the "BigMag" coater were performed on a Linux-Cluster at Fraunhofer IST consisting of 16 dual-Pentium-III PCs operating at 800 MHz. As the substrate movement leads to quite complex gas flow interactions between the compartments, a rather big part of the "BigMag" coater is contained in the DSMC simulation consisting of modules M5-M11 (see Figure 1), which is a total volume of approx. 7.5 m^3.

Each compartment in the DSMC model has a seven-fold segmentation in y-direction (i.e. along target axis) according to the seven-fold tuning gas inlet. For modules M8-M10, each transport roll and the twin rotatables are approximated by numerous rectangular boxes, furthermore, the shieldings and the T profiles are considered. For each compartment connection in the upper region, all of the 20 rectangular slots are contained in the model.

The substrate volume in modules M8-M10 is constructed of multiple rectangular segments sized 5 cm in x-direction, i.e. 14 segments per compartment. The connections of each segment with the adjacent volume can be individually "switched" on or off, thus allowing the simulation of substrate movement in a resolution of five cm steps. A total amount of 1005 rectangular boxes is used to form the whole geometry sketched in Figure 1.

For the substrate movement, the convention for the x-coordinate sketched in Figure 2 will be used throughout this paper. The origin x=0 is defined at the position where the glass front

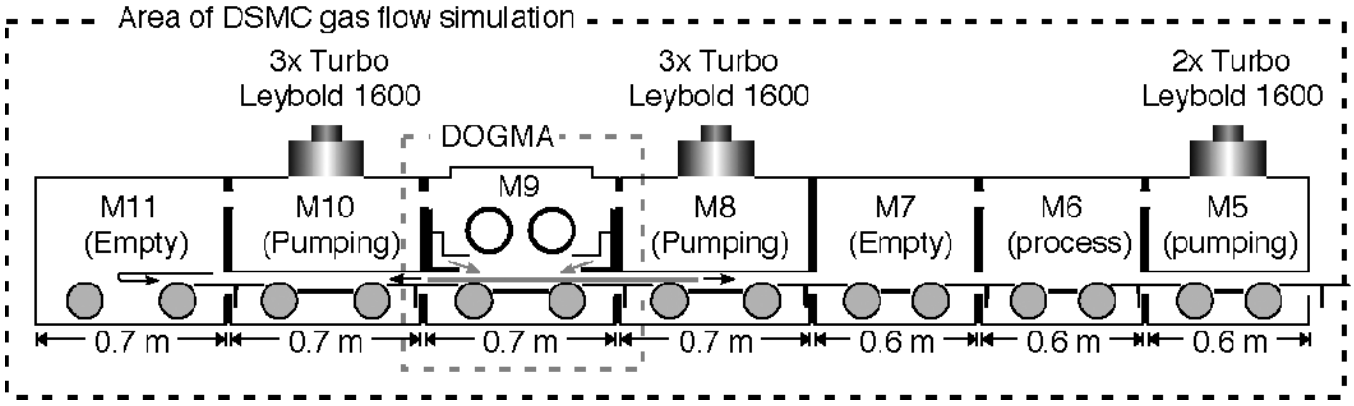

Figure 1: Cross section of modules M5-M11 of the "BigMag" in-line coater at Applied Films. The sputtering process is located in module M9 comprising two jumbo-sized rotatable magnetrons with metallic Zn targets.

edge enters the transport slot in module M8. The deposition chamber M9 is entered at x=0.7 and left by the rear edge at x=2.4. The shieldings beneath the targets limit the range where the glass is being coated to x=0.8...2.3. For the substrate movement, all positions between x=0 and 2.8 m have been considered with a resolution of five cm leading to 57 different DSMC simulation scenarios. The first scenario has been calculated using 150,000 DSMC time steps of 2.5×10^{-5} s and 10,000 time averaging steps which has been found sufficient to yield a stationary flow field. For each subsequent substrate propagation of Δx=5 cm, 25000 additional DSMC steps were applied, which corresponds to a substrate speed of 4.8 m/min.

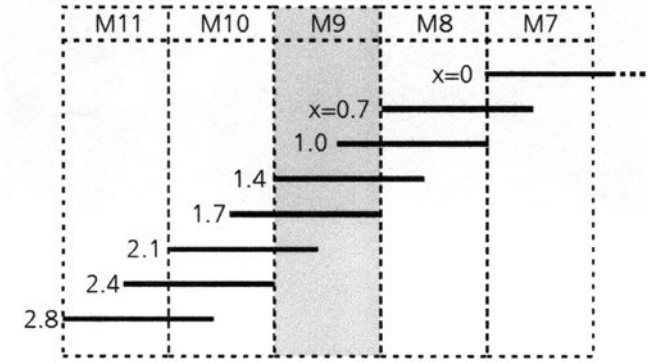

Figure 2: Coordinate definition for the substrate movement. The origin x=0 is defined where the glass front edge enters module M8 from M7.

Complete sets of DSMC simulations for all 57 substrate positions were performed for an Ar inlet of 300 sccm and 600 sccm via the main gas line. On the Linux-Cluster at Fraunhofer IST, one complete set takes about 12 days and produces about 1 GB of data files where the time averaged particle densities and velocity components are stored.

The DSMC simulations are found to agree well with experimental data from the "BigMag" coater. Figure 3, for example shows the total pressure variation in module M10 measured during a dynamic deposition process in oxide mode (black symbols) in comparison with DSMC simulations (light symbols). It should be mentioned that the pressure measurements by the used "Ionivac" gauges does not yield accurate absolute values. The shape of the pressure versus position function agrees well with the DSMC simulation showing that the gas flow model of the "BigMag" coater is highly realistic.

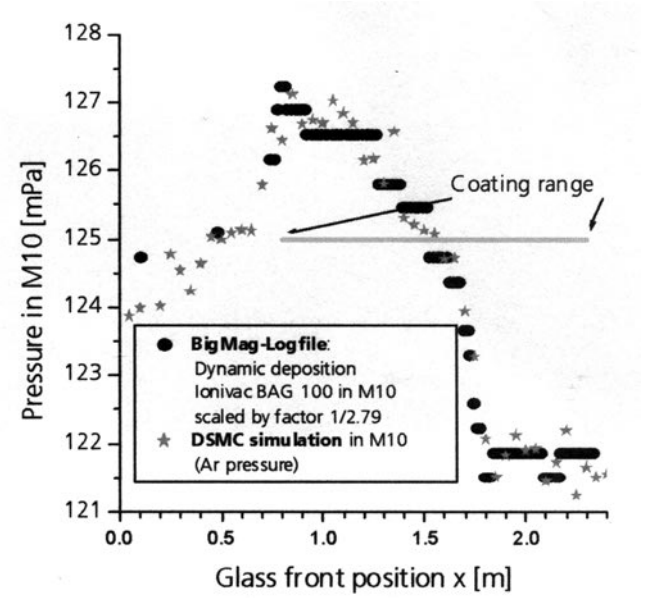

Figure 3: Comparison of total pressure variation measured in M10 due to substrate movement during dynamic deposition with the Ar pressure variation obtained from DSMC simulation.

Heuristic Sputter Model of the "BigMag" Coater

In order to be able to model the reactive ZnO sputtering process in module M9 at real-time speed, a heuristic model based on the "DOGMA" concept presented in [2] has been constructed. As shown in Figure 1, this approach only contains the sputtering compartment M9, while the gas flow connections to the adjacent compartments are attached to this model as effective pumping speeds.

In this two-dimensional model, the volume of M9 is divided into sub-cells as shown in Figure 4. Along transport direction, the volume comprises a left, middle and right zone while in z-direction the volume is divided into five zones leading to a total of 15 volume cells. In each cell a rate model of the reactive sputtering process similar to the Berg model [3] is operating, while the gas and particle transport between targets and cells is given by flow conductances and sputter particle distribution coefficients. For modeling the target voltage, the secondary electron emission approach [4] is also included into the formalism.

The effective pumping speed $S_{p.eff}$ is calculated from the net gas flow ϕ and the pressure p at the inner side of each connection via

$$S_{p.eff} = kT \times \phi / p$$

Equation 1

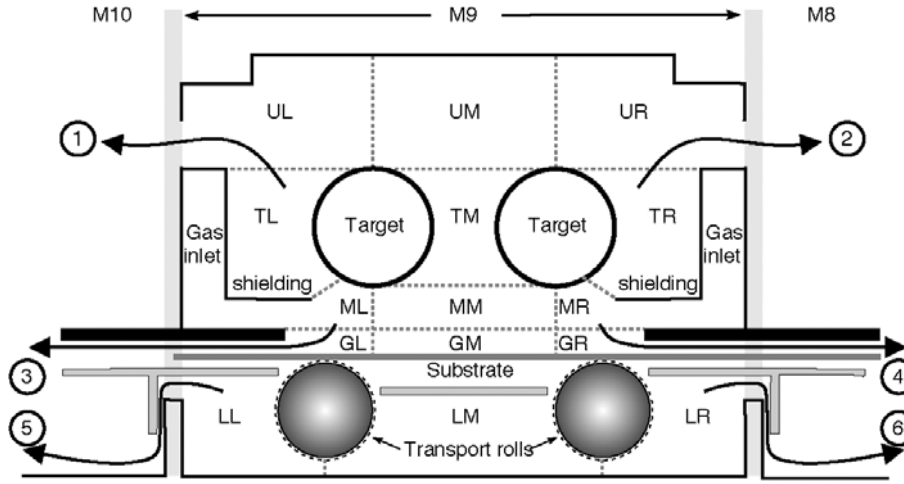

Figure 4: Segmentation of the sputtering compartment M9 for the heuristic model of reactive sputtering. The gas flow connections to the adjacent compartments are equivalent to six effective pumping speeds at the positions labeled 1–6.

Connections to adjacent compartments are found at six different locations labeled "1–6" in Figure 4. The connections 1 and 2 are the flow paths to the upper pumping regions in M8 and M10 via 20 rectangular orifices on each side. The glass transport slots on either side are represented by connections 3 and 4 while connections 5 and 6 are in the lower region of the coater at the T profiles between the compartment junctions.

As shown in Figure 5, the dependency of the six effective pumping speeds from substrate position is quite complex. The pumping speed of connection 1 to the upper pumping region in M10 e.g., is raised by 5% if the substrate enters the left transport slot. The reason is that gas leaving via connection 3 also enters the pumping compartment in M10 via M11 increasing the total pressure in M10. Thus the effective pumping speed at connection 1 is lower for an open transport slot at the left side.

Modeling of the Reactive ZnO Sputter Process

In order to tune the heuristic model to the real sputter compartment, target voltage curves with respect to oxygen flow have been recorded for different process conditions. Without substrate, the total sputter power was 60 kW while two different Argon inlet conditions, 400 and 800 sccm, were investigated.

As shown in Figure 6, an increase of the Ar flow by a factor of two leads to a strong shift of the voltage curves towards higher oxygen flows and lower voltage. This behavior can not be understood in terms of the previously reported models in [2-4]. A solution to this problem is given by a new physical approach—the so-called "ion-loss" mechanism of the plasma discharge. As shown in Figure 4, shieldings are located quite close to the twin rotatable targets. Especially at low pressure, where the cathode fall regime is known to be widened, a certain fraction of the generated Ar^+ ions could get attracted by the shielding surfaces instead of the targets.

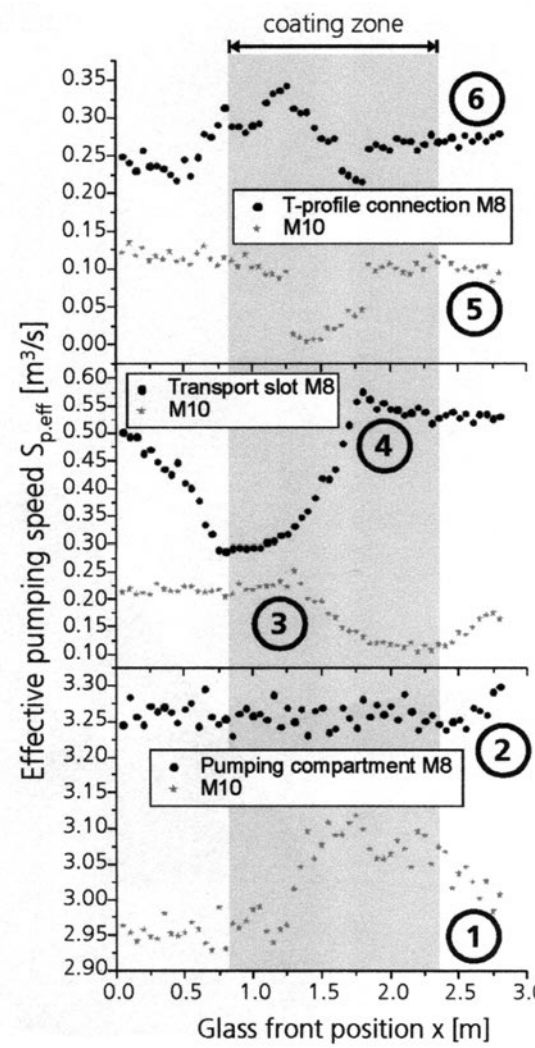

Figure 5: Effective pumping speeds calculated by DSMC simulations at the six connections between sputter compartment M9 to the adjacent compartments with respect to substrate position.

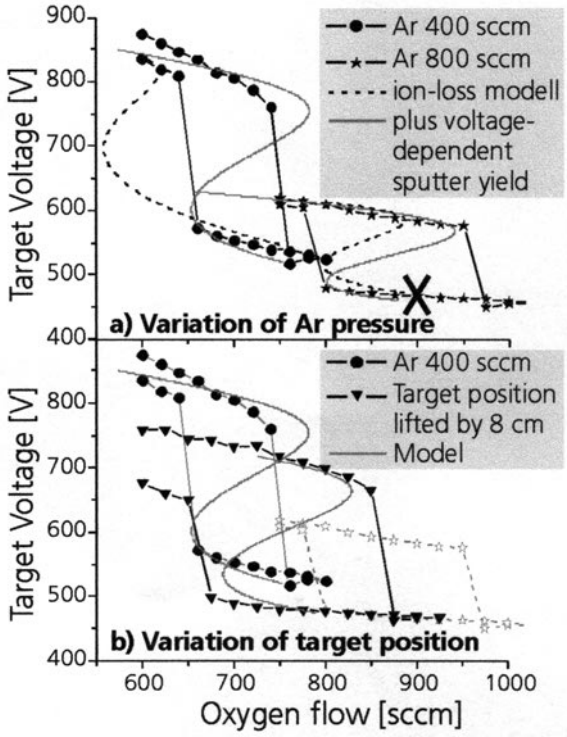

Figure 6: Simultaneous fit of measured target voltage versus oxygen flow hysteresis curves for original and modified target position.

This effect is reduced at higher pressure, where the cathode fall is narrowed and the mean free path of the Ar^+ ions is reduced. To quantify this relation, the secondary electron model [4] has to be modified. Originally the time development of the ion current j_+ was assumed to depend on the secondary electron coefficient γ and an ion loss coefficient β via

$$\frac{\partial j_+}{\partial t} = \frac{j_+}{\tau}(\gamma - \beta)$$

Equation 2

In [4] was argued that the ion loss factor β should be close to one as long as the majority of Ar^+ ions generated by secondary electrons return to the target surface. If an additional ion loss mechanism is assumed the ion loss coefficient β has to be modified. We suggest β to be dependent from a pressure-dependent Knudsen number $Kn(p)$ of the generated Ar^+ ions, i.e. the ration between their mean free path and the effective distance between targets and shielding. For the coefficient β, this leads to

$$\beta(p) = 1 + \tilde{\beta}\exp\left(-\frac{1}{Kn(p)}\right)$$

Equation 3

This approach yields the mentioned shift of the target voltage characteristics at increased Argon flow. However, at this stage the model fit is still not satisfying as shown by the dashed lines in Figure 6a. It is impossible to fit both target voltage curves simultaneously with a common parameter set.

It turned out that a good fit is only possible with an additional voltage dependency of the sputter yield. This is already reported [5] but has not yet been considered, in previous literature regarding reactive sputtering simulation. If Y_{Berg} is the sputtering yield taken from the Berg model [3], we suggest the following modification:

$$Y(U) = Y_{Berg}\left(\frac{U - U_a}{U_{ref} - U_a}\right)^{\alpha}$$

Equation 4

with the target voltage U, the work function U_a and a reference voltage Uref where $Y(U)=Y_{Berg}$. The sputter yield data reported in [5] indicate that the dependency of Y from target voltage should be either linear or like a square root. In our experiments we found an exponent of α=0.4 leading to the straight lines shown in Figure 6a and 6b which well reproduce the experimentally recorded hysteresis curves.

The new ion-loss mechanism is further supported by an experiment where the targets are moved several cm upwards leading to an increased effective distance between targets and shieldings. As shown in Figure 6b, the modified target position strongly influences the voltage versus oxygen flow characteristics. This behavior could be well described by the simulation by just modifying the effective diameter between targets and shieldings in the model.

Dynamic Deposition Simulation

A dynamic ZnO deposition experiment was performed at 60 kW sputter power, high Ar flow of 800 sccm and an O_2 flow of 900 sccm. This corresponds to a working point in oxide mode but within the turning regime of the process indicated by a cross in Figure 6a.

The substrate movement is introduced into the simulation by applying the six time-dependent effective pumping speeds as shown in Figure 5 leading to time-dependent process fluctuations. In the three coating regions labeled “GL, GM, GR” in Figure 4, the time-dependent deposition rates are subsequently calculated. For a given location on the glass substrate, these deposition rates are integrated with respect to the residence time of the location in the three coating regimes during dynamic deposition. This is repeated for an array of equally spaced locations on the glass substrate resulting in the relative thickness profile indicated by the light symbols in Figure 7.

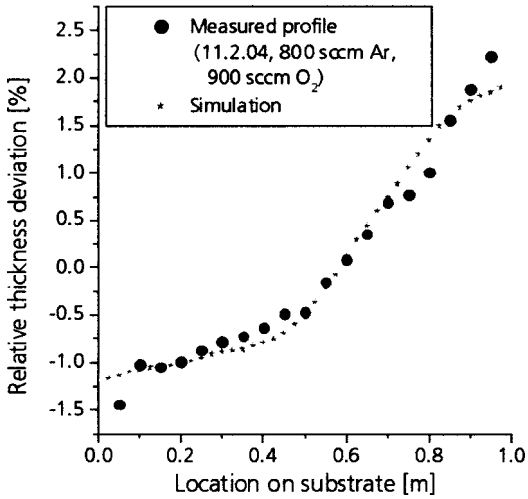

Figure 7: Measured and simulated relative film thickness profile on a substrate coated at 800 sccm Ar, 900 sccm O_2 and 60 kW target power.

As can be seen, this agrees well with an experimentally obtained film thickness profile measured by photo-reflectometry. Thus it is demonstrated that the simulation model is suited for the design of compensation algorithms for the film thickness deviations in x-direction.

CONCLUSION AND OUTLOOK

A quantitative model of large area reactive magnetron sputtering has been developed and implemented for the quantitative prediction of film thickness distribution for the first time. The DOGMA code used allows for the simulation of gas flow distribution and process parameters, such as discharge power and plasma impedance as well as for the simulation of the growth rate of the deposition process. The spatial characteristics of the plasma discharge are not incorporated within our model at the present time. This is a subject of ongoing work.

For the layout of advanced in-line coaters, the utilization of process simulation techniques will allow for achieving superior precision in terms of coating homogeneity and process reproducibility as well as for very fast and reliable switching periods from one coater configuration to another.

REFERENCES

1. G.A. Bird, Molecular dynamics and the direct simulation of gas flows, Oxford Engineering Science Series, 42, 1994.

2. A. Pflug, N. Malkomes, V. Sittinger, and B. Szyszka, 45th Annual Technical Conference Proceedings of the Society of Vacuum Coaters, p. 16, 2002.

3. S. Berg, H.-O. Blohm, T. Larsson, and C. Nender, J. Vac. Sci. Technol., A5 (2), 202, 1987.

4. A. Pflug, B. Szyszka, V. Sittinger, and J. Niemann, 46th Annual Technical Conference Proceedings of the Society of Vacuum Coaters, p. 241, 2003.

5. General Mills Inc., General Mills Report, 2309, 196.

Sputtering of Very Thin Pd-alloy Hydrogen Separation Membranes

H. Klette and R. Bredesen, Sintef Materials Technology, Oslo, Norway

Key Words: Sputter deposition; Palladium film; Free standing and supported membranes; Hydrogen separation

ABSTRACT

Three types of hydrogen separation membranes were developed in this work, based on the patent "Method of Manufacturing Metal Membranes" [1]. Tubular and flat hydrogen separation membranes with a 316L sintered porous stainless steel (PSS) support covered with a very thin palladium (Pd)-silver (Ag) foil (1-5 mm thick) and a flat free-standing Pd/Ag foil, fixed in a frame of two 316L-plates. The manufacturing method for the membrane is unique [1], as the Pd/Ag layer is prepared as a foil by DC-magnetron sputtering on a substrate with polished surface, then removed, transferred, and placed onto a membrane support. This freedom to choose the membrane support independently from the membrane material in a two stage preparation process opens up for the use of various PSS and other types of supports.

This novel technique produces highly selective thin layers with a high hydrogen flux, making their use for hydrogen separation economically attractive.

INTRODUCTION

Palladium and its alloys have the property of being impermeable to all gases except hydrogen. From a hydrogen gas mixture, ultra pure hydrogen can be extracted by the use of Pd-membranes, provided that a hydrogen partial pressure difference exists across the membrane. The typical operating temperature range for this membrane type is about 250-600°C. A potentially important application is the production and the purification of hydrogen for PEM fuel cells. The current availability of hydrogen selective membranes and their utilization are very much limited due to high cost and a low hydrogen flux. A reduction in the thickness would contribute significantly to both factors, this as palladium is very expensive and the hydrogen flux is inversely proportional to the thickness of the membrane. The production technology of SINTEF enables a membrane thickness in the range of 1-5 μm, which is an important reduction compared to the commercial available membranes that utilize Pd-layers of 20-70 μm.

There are several ways to manufacture Pd-alloy membranes, the most simple and reliable is just to drill a hole in a rod of Pd or Pd-alloy, which of course is costly but provides high durability. Most of the work around the world today is dedicated to find a method for deposition thin (1-10 mm thick) layers of Pd-alloy on porous supports [2]. The most common methods for coating are sputtering, CVD, and electroless deposition, all of which are facing the inherent problem of covering the pores of the support. The SINTEF method overcomes this by having a separate support for the growth of the film. This method of manufacturing thin free standing films can also be extended to other materials. It also opens up for a broader use, for example, in scientific experiments where there is a need for vacuum barriers of very thin metal films.

EXAMPLES OF APPLICATIONS

Pd-alloy membranes for hydrogen separation and purification have a wide range of possible applications [2]. Particularly interesting is the proposed clean energy society, where hydrogen technology would play a key role. Some areas where hydrogen selective membranes have technological relevance are:

H_2-generation, reforming of fuel, fuel cells
- Automotive, on board and refueling stations
- Mobile units, Portable Computers and military applications

H_2-purification
- Purification of H_2 for the semiconductor industry
- Isotope separation for the nuclear industry

Chemical industry
- Production and adjustment of syngas composition
- Dehydrogenation and hydrogenation reactions
- H_2 recovery from e.g. ammonia recycle streams

Carbon sequestration
- H_2 separation from gases containing CO_2 ($CO/H_2O/CH_4/H_2/CO_2$) in precombustion decarbonization processes

GROWTH OF PALLADIUM ALLOY FILMS

The method of manufacturing free standing films by the use of evaporation deposition process for foils thicker then 25 mm has been described in the patents of Hugh R. Smith [3,4]. The particular magnetron sputter process presented for growing Pd/Ag23% uses silicon mono crystalline wafer as substrate. It is generally known that metallic foils may, in some cases, be pulled off their substrate after deposition due to bad adhesion, also named deadhesion [5]. Normally, efforts prior to and/or

 505/856-7188 ISSN 0737-5921

47th Annual Technical Conference Proceedings (April 24–29, 2004) Dallas, TX USA

under sputtering are to increase the adhesion; however, in our case the objective is the opposite. The DC-magnetron sputtering results in a continuous and ductile film free of pinholes. In addition, the stress in the freestanding film after release from the substrate is very low. For the particular substrate in use (silicon wafers) we utilize the known poor adhesion of noble metals to oxygen rich surfaces. As the adhesion is very low, one can assume that only physical bonds are created between the Pd/Ag film and the substrate. The Pd/Ag film, which copies the topography of the surface of the highly polished and smooth silicon wafer, has on a macro scale an extreme uniform and homogeneous morphology. However, on a microscale we have observed a slight difference in the grain structure between the two sides of the film after sputtering. Films down to 200 nm have been prepared, though for permeation experiments, films in the range of 0.8 to 5 μm were used.

INTEGRATION OF FILM AND SUPPORT

The following two photos illustrate the capabilities of the thin Pd/Ag-foil to integrate with various porous supports. Figure 1 shows the capability of the foil to shape according to the underlying surface topography of a woven stainless steel mesh. Figure 2 shows the foil attached to a porous stainless steel support suggesting no intrusion of the film into the pores.

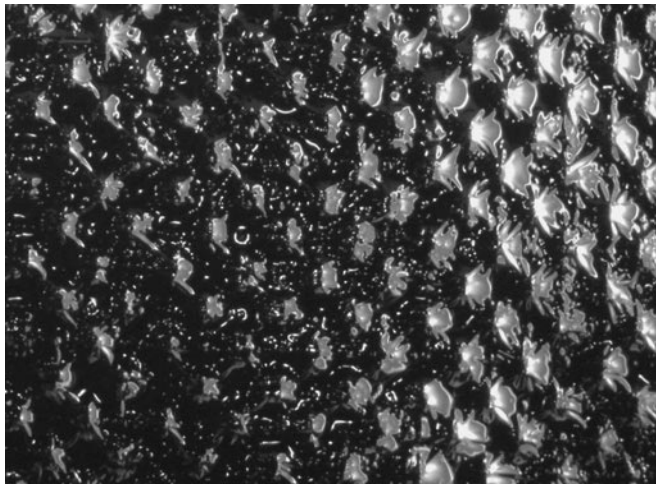

Figure 1: A flat supported Pd/Ag membrane after H_2-permeation test.

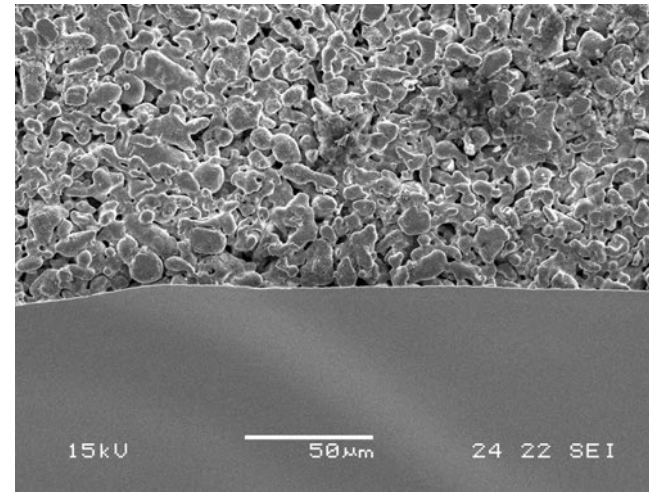

Figure 2: SEM-photo, showing the edge of the Pd/Ag foil and the underlying PSS support.

HYDROGEN SEPARATION ASSEMBLIES

The thin Pd/Ag alloy film has been utilized in three types of membrane assemblies, non-supported flat, supported flat and supported tubular. Figure 3 shows the nonsupported membrane assembly, which can sustain differential pressures in the range of 0-0.5 bar at 300°C. Figure 4 shows the flat supported version, similar to the flat nonsupported, with the exception of the porous support. Figure 5 shows the tubular assembly, consisting of a porous stainless steel tube covered on the outside with the Pd/Ag foil.

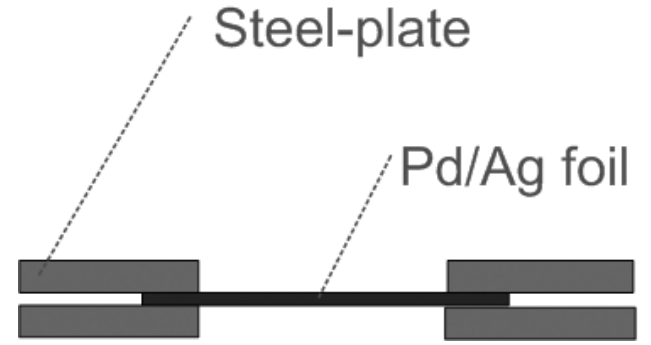

Figure 3: Schematic illustration of a flat nonsupported membrane.

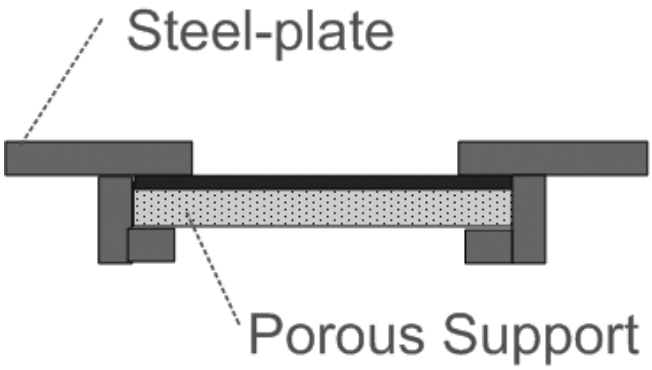

Figure 4: Schematic illustration of a flat supported membrane.

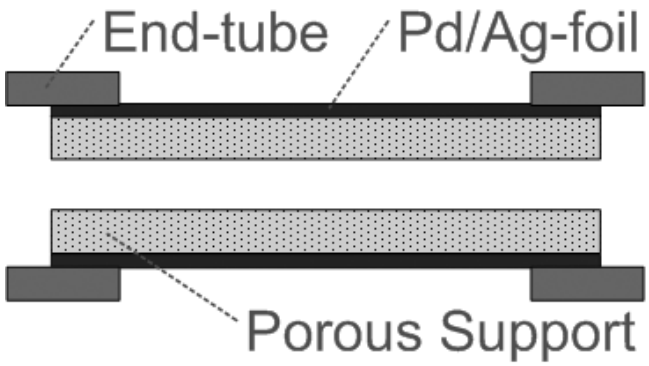

Figure 5: Schematic illustration of a supported tubular membrane.

EXPERIMENT

The sputtering was carried out in a CVC-601 using 4" silicon wafers as substrates.

The Pd/Ag membranes were tested for permeation under different partial pressure gradients, all measurements were carried out at 300°C. The permeation was measured in pure H_2 or in mixtures of H_2+N_2. In some experiments the membrane was treated in air ("activated") before the permeation measurements.

RESULTS

The tubular membranes were tested up to 15 bar pressure difference and their upper H_2-permeance was 3e-6 mol/(m2*s*Pa).

For flat non-supported membranes, a H_2-permeance of 6e-6mol/(m2*s*Pa) was achieved. If the membrane was "activated" an increase to 2e-5 mol/(m2*s*Pa) could be obtained, one of the highest values ever reported.

CONCLUSION

Very thin freestanding foils (0.8-5μm) of Pd/Ag-alloys have been manufactured and integrated in H_2-separation modules. The H_2-flux was found to be high, as predicted for these thicknesses [6]. The use of freestanding films for hydrogen separation membranes has shown to be successful and further development in upscaling is foreseen.

ACKNOWLEDGMENTS

The research is financed by the Norwegian Research council, the European Commission and the Carbon Capture Project (CCP).

REFERENCES

1. R. Bredesen and H. Klette, "Method of Manufacturing Thin Metal Membranes", US Patent No. 6086729A, 2000.

2. S.N. Paglieri and J.D. Way, "Innovations in Palladium Membrane Research," Separation and Purification Methods, 31(1), 1-169, 2002.

3. H.R. Smith, "Production of Ductile Foil," US Patent No. 3270381, 1965.

4. H.R. Smith, "Apparatus for Continuos Foil Production by Vapor Deposition," US Patent No. 3183563, 1965.

5. D.M. Mattox, "Handbook of Physical Vapor Depsoition (PVD) Processing", pp. 588-635, Noyes Publications, 1998.

6. R. Dittmeyer, V. Hollein, and K. Daub, "Membrane Reactors for Hydrogenation and Dehydrogenation Processes Based on Supported Palladium," Journal of Molecular Catalyst, A: Chemical (173), 135-134, 2001.

Recent Developments in Measuring Permeation Through Barrier Films and Understanding of Permeation Processes

H. Nörenberg, Technolox Ltd., Oxford, United Kingdom; and V.M. Burlakov, Department of Materials, University of Oxford, Oxford, United Kingdom

Key Words: Permeation barrier coatings, Gas permeation, Moisture permeation, Modeling

ABSTRACT

A novel permeation measurement system with a mass spectrometer as detector has been set up. Test measurements on barrier layers gave a lower detection limit for WVTR of about $5x10^{-5}$ g/m^2/day. The advantage of the mass spectrometric method is that it can be used to study the permeation of a wide range of gases or vapors. Proof of principle measurements have been carried out for position resolved permeation studies. The method could be used to measure the rate of permeation through samples other than films, such as electronic components (batteries), and through the edges of samples. Theoretical studies of the pressure dependence of the rate of permeation of gases through polymer films (example: OPP), showed that the pressure dependence of gas transport through these layers is caused by an effective decrease in the diffusion activation energy after gas sorption. The mechanism causing this decrease is related to saturation of deep traps so that fast-diffusion channels possessing lower activation energy are created. This confines mass transport to a network of shallow traps.

INTRODUCTION

The implementation of experiments to measure rates of permeation at an extremely low level and the understanding of the permeation process itself are the key to the future progress in the area of barrier layers. OLED development and quality control, for instance, require a "magic rate" of water vapor transmission (WVTR) of about 10^{-6} g/m^2/day or less [1]. The calcium test is widely used to estimate the WVTR. However, the calcium test is restricted to chemically reacting permeants such as water vapor and oxygen. Permeation measurements based on a mass spectrometer as detector have been reported for permeation of a variety of gases and water vapor through polymers [2,3]. Permeation of gases and vapors through barrier layers may be influenced by a number of parameters. Experimental observations showed that even permeation of inert gases through simple polymers is pressure-dependent [3,4].

EXPERIMENTS

Figure 1 shows a schematic view of the experimental setup. The ultra-high vacuum (UHV) system consists of two chambers, which allows the conditioning of the sample S in the preparation chamber P before introducing it into the investigation chamber I. The investigation chamber I is equipped with a quadrupole mass spectrometer MS to detect the partial pressure and a xyz-stage for sample manipulation. A gas container is filled with water vapor similar to the procedure described in [1]. After introduction of the gas container with the sample into the preparation chamber P and evacuating to a sufficiently low vacuum level, the sample is then transferred into the investigation chamber I by means of a transfer arm and positioned to face the mass spectrometer MS. The partial pressure of water vapor of the unknown test sample is measured. With the known values for the partial pressure of water vapor and the WVTR of a calibration sample, the WVTR of the test sample can be calculated.

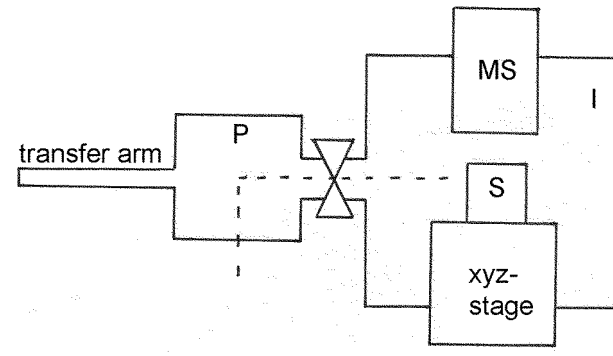

Figure 1: Schematic view of experimental set up with preparation chamber P and investigation chamber I, S: sample, MS: mass spectrometer.

505/856-7188 ISSN 0737-5921
47th Annual Technical Conference Proceedings (April 24–29, 2004) Dallas, TX USA

RESULTS AND DISCUSSION

Sensitive WVTR Measurements

Figure 2 illustrates the capability of the mass spectrometric method. The partial pressure of a calibration sample and a barrier sample is shown as function of time. The calibration sample was 0.1 mm thick foil of PEN with a WVTR of 1.25 g/m²/day (at 40°C).

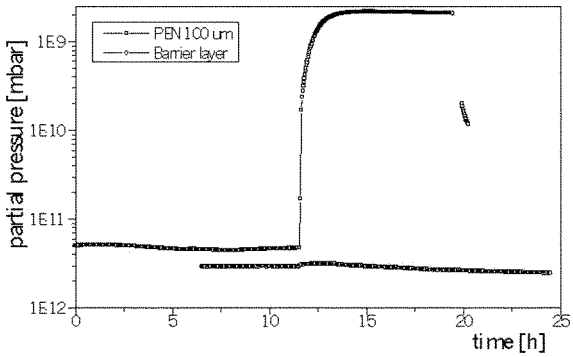

Figure 2: Partial pressure as function of time for a barrier sample and a calibration sample (PEN).

At about t=12 h (Figure 2) the sample mounted on the gas container was introduced into the investigation chamber. The water vapor coming from the gas container leads to an increase of the partial pressure of the water vapor signal. There is a pronounced increase of the water vapor partial pressure for the PEN sample. As Figure 2 shows, the partial pressure settles around 2.5×10^{-9} mbar, which corresponds to a WVTR of 1.25 g/m²/day. For the barrier layer, the increase of the water vapor partial pressure is less pronounced. Figure 2 shows that the increase in the partial pressure of the water vapor of the barrier layer is less than 10^{-4} g/m²/day. This means that the current experimental setup has a dynamic range of at least six orders of magnitude [3] and a lower detection limit of about 5×10^{-5} g/m²/day is estimated. The lower detection limit may depend on the nature of the sample (i.e. whether outgasing occurs). In order to obtain the high dynamic range of sensitivity for water vapor, $H_2{}^{18}O$ was used [2].

Position-Resolved Permeation Measurements

To study the permeation position-resolved, the gas container with the sample was positioned very close to the mass spectrometer. The sample was of a piece of PEN film of about 1mm exposed diameter. Outside this exposed area the sample was covered with impermeable material. The sample was moved across the mass spectrometer by means of the xyz-stage (see Figure 1), so that different areas of the sample were exposed to the ionizing region of the mass spectrometer at each point of measurement. Figure 3 shows the partial pressure as function of lateral replacement. As the sample moves across the mass spectrometer, the partial pressure shows a clear maximum at x=0 and decreases to both sides. The variation of partial pressure, which is the contrast of the permeation, is about 1×10^{-9} mbar or 30% between the center and 1 mm off center. This variation is the proof of principle for position resolved permeation measurements.

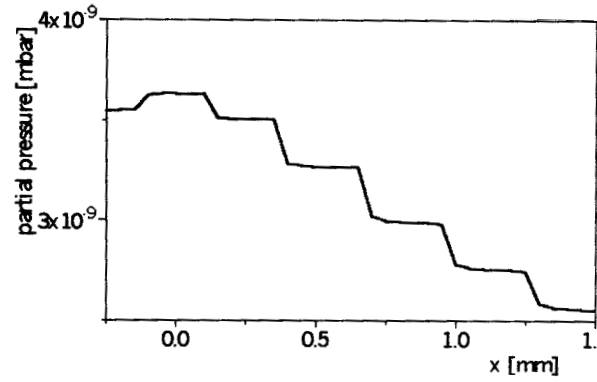

Figure 3: Partial pressure as function of lateral displacement (sample: PEN).

Theoretical Calculations

A phenomenological model for diffusion of molecules through polymer substrates has been developed [5]. The diffusion is modeled as random hopping over a potential barrier of the diffusion activation energy E_{act} between sites. These sites have random sorption site energies. At t=0 the polymer is free of the permeant gas. The gas then enters and diffuses through the polymer. Figure 4 shows the situation at t>0. Some gas atoms are already inside the polymer occupying sorption sites that had a low enough energy to trap these atoms (black spots in Figure 1, unoccupied sorption sites are shown as circles). Once the site is occupied, the pathway through this site is blocked. The gas atoms take pathways, which do not contain such deep trap sites and can therefore diffuse faster.

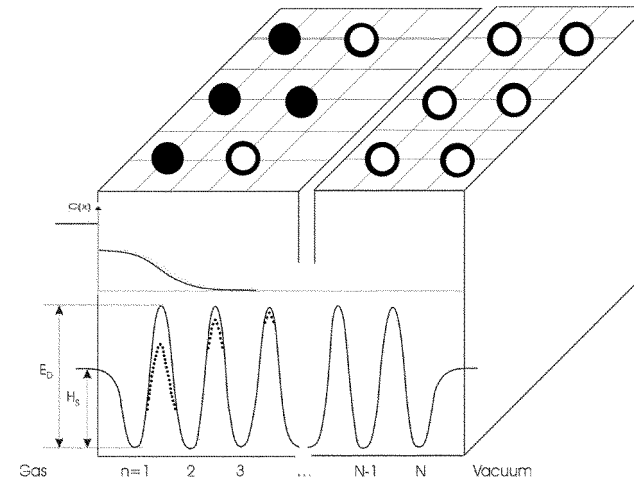

Figure 4: Model of diffusion of small molecules through a polymer. The sample is divided into N slices perpendicular to the concentration gradient. Molecules enter from the left side.

The concentration of the gas inside the polymer is shown as c(x). The solid sinusoidal profile in the lower part of Figure 4 shows the initial energy in the polymer. At t>0 the energy is lowered in the regions, where gas is dissolved (dotted line). Formally, the dependence of permeation upon the gas ambient pressure is taken into account via the dependence of the activation energy for gas diffusion E_{act} upon the gas concentration $n(x,t)$

$$E_{act}(x,t) = E^0_{act} \cdot \left(1 - \alpha \cdot n(x,t)\right)$$

Equation 1

where E^o_{act} and α are constants. Solving numerically the diffusion equation with a space- and time-dependent activation energy given by Equation 2.

$$\frac{\partial n(x,t)}{\partial t} = D_0 \cdot \exp\left(-\frac{E_{act}(x,t)}{kT}\right) \times \left[\frac{\partial^2 n(x,t)}{\partial x^2} + \alpha \cdot E^0_{act} \cdot \left(\frac{\partial n(x,t)}{\partial x}\right)^2\right],$$

Equation 2

and taking into account the gas solubility through the boundary conditions, we simulated the permeation process as a function of time. The consequence of having such fast channels is that, at a high pressure on the feeding side, a higher rate of permeation is achieved. At a low pressure, there is a higher probability that gas atoms become trapped at unoccupied deep trap sites, which slows down mass transport. The model is used to study the transient behavior of the rate of permeation.

Figure 5 compares experimental data and the results from the calculations. Experimental data were used from Xenon permeation through an OPP sample [3]. Input parameters are the solubility, the diameter of the permeating gas atoms, and the activation energy for diffusion. Figure 5 shows that the model is capable of reproducing experimental results with good accuracy. Hence, the random distribution of sorption site energies is indeed responsible for the pressure dependence of the rate of permeation. A further advantage of the method is that the results obtained for one gas can be used as input to predict the transient behavior P=P(t) of other gases through the polymer.

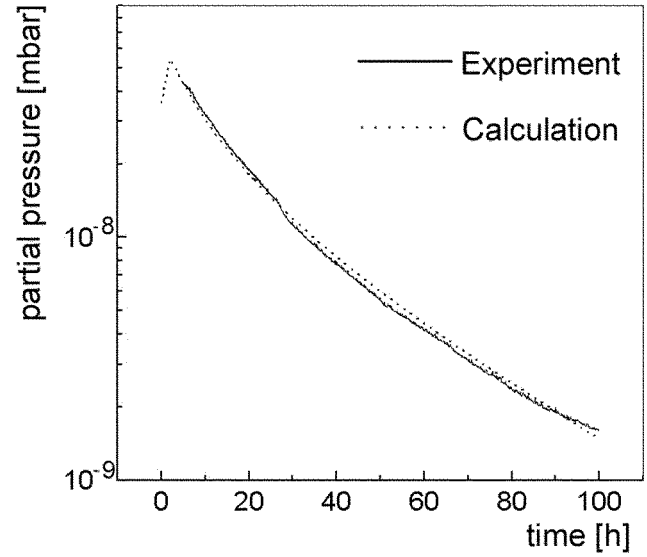

Figure 5: Comparison of experimental data with calculations.

CONCLUSION

A method to measure WVTR with a mass spectrometer as detector was set up. Test measurements gave a lower detection limit of about 5×10^{-5} g/m²/day WVTR. As the mass spectrometer can detect a wide range of gases and vapors, the application method is not restricted to measure WVTR. It has potential for the study of permeation in other applications, such as vacuum insulating panels, where the permeation of all gases from the environment is of great interest.

Proof of principle for position-resolved permeation measurements has been obtained. In this mode, the sample is moved with respect to the mass spectrometer giving the rate of permeation along a line or as a two-dimensional pattern on the sample.

A phenomenological model has been developed to describe the transient permeation of gas through a polymer membrane. The distribution of the trap site energies accounts for the observed pressure-dependent permeation of heavy noble gases through OPP.

REFERENCES

1. H.-C. Langowski, A. Melzer, and D. Schubert, "Ultra High Barrier Layers for Technical Applications," 45th Annual Technical Conference Proceedings of the Society of Vacuum Coaters, 45, 471, 2002.

2. H. Nörenberg, T. Miyamoto, G.D.W. Smith, G.A.D. Briggs, and Y. Tsukahara, "Mass spectrometric estimation of gas permeation coefficients for thin polymer membranes," Rev. Sci. Instruments, 70, 2414, 1999.

3. H. Nörenberg, V.M. Burlakov, H.-J. Kosmella, G.D.W. Smith, G.A.D. Briggs, and Y. Tsukahara, "Permeation of noble gases (He, Ne, Ar, Kr, Xe) through thin membranes of OPP studied by mass spectroscopy," Polymer 42, 10021, 2001.

4. Y. Naito, K. Mizoguchi, K. Terada, and Y. Kamiya, "The Effect of Pressure on Gas Permeation Through Semicrystalline Polymers above the Glass Transition Temperature," Journal of Polymer Science: Part B: Polymer Physics, 29, 457, 1991.

5. V.M. Burlakov, H. Nörenberg, G.A.D. Briggs, and Y. Tsukahara, "Model for the Pressure-Dependent Permeation of Small Molecules through a Polymer Membrane," Journal of Polymer Science: Part B: Polymer Physics, 41, 1308, 2003.

Aluminum Soldering Performance Testing of H13 Steel as Boron Coated by the Cathodic Arc Technique

G. Mackiewicz Ludtka and V.K. Sikka, Oak Ridge National Laboratory, Oak Ridge, TN;
and J.M. Williams, C.C. Klepper, R.C. Hazelton, and E.J. Yadlowsky,
HY-Tech Research Corporation, Radford, VA

Key Words: Cathodic arc deposition; Corrosion resistant coating; H13 steel; Soldering

ABSTRACT

A unique, cathodic (or vacuum) arc-based technique for boron (B) and boron-rich plasma generation has been developed for use as a coatings technology and other applications. Boron would make an excellent coating for dies for Al-alloy casting because it has a repulsive chemical interaction with aluminum but a highly attractive interaction for steel. Other properties such as hardness, abrasion resistance, corrosion resistance and refractive qualities also appear favorable. In this case, owing to the attractive chemical forces, the coating was partially in-diffused into the H13 steel coupons. The high ion energies inherent in cathodic arc deposition may have also contributed to this effect. An automated test cycle consisting of immersion of coated coupons in pure molten Al at ~700°C, followed by removal and quenching was used. Failure was indicated by soldering to the extent that removal from the melt through a wiping aperture of 1/16 inch larger in diameter than the coupon could not be accomplished. The control sample was completely wetted after the first cycle. It was possible to obtain 50 cycles on the B-coated sample, with about half the sample area being soldered and about half remaining unwetted. Soldering, where it occurred, was attributed to weak areas in this particular coating. It is concluded that boron shows promise as a life-extension coating for aluminum casting steel dies.

INTRODUCTION

Liquid aluminum is extremely reactive and easily alloys with alloy constituents of H13 die steels. Researchers have investigated various protective coatings and coating methodologies to prevent the erosion-corrosion in die casting dies. Most of the research and development efforts have concentrated on developing and evaluating thin coatings typically applied by physical vapor deposition techniques (PVD), chemical vapor deposition (CVD), and nitriding techniques. Coatings typically deposited by these techniques include CrN, CrC, B_4C, VC, CrN_2, and Ion Nitriding. The materials have been chosen due to their resistance to soldering in the presence of liquid aluminum. The primary failure mechanism of these coatings is spalling due to differences in the coefficient of thermal expansion (CTE) between the coating and the substrate. The CTE of H13 steel is approximately 12 x 10^{-6}/K, while the CTE of CrN is 0.7 - 3.1 x 10^{-6}, that of VC is 6.5 x 10^{-6}, B_4C is 4.5 x 10^{-6}, TiN is 8 x 10^{-6}, and Cr_2C_3 is 10.3 x 10^{-6}. With typical temperature cycles in excess of 500°C, the expansion and contraction of the steel make the survivability of these ceramic type coatings difficult to impossible. Therefore, even if a material is solder resistant, the ability to coat it on a die surface and keep it on a die surface is a technical challenge.

Residual stress control and the prevention of fatigue cracks due to thermal cycling of these dies are two additional and important objectives in coating development. Some coatings offer some resistance to soldering but the results are often qualitative and strongly depend on the die, die location, melt temperature, and many other variables. Various types of PVD, CVD, and nitriding approaches have been attempted [1-7]. Multiple layer approaches to help accommodate stresses and diffusion barriers are also being considered [4]. However, these approaches are often very expensive. Other recent investigators [8] are utilizing cermet coatings which offer the potential solder resistance of the low CTE ceramic materials and the stress accommodating properties of metals. The key in depositing these coatings is the ability to fuse the cermet to the steel without dissolving the steel and not allowing iron to be present at the coating surface. Testing of these coatings by the industry has had mixed reviews due to the complex environment experienced in the die casting industry.

This paper describes the recent results and promising die solder resistance of a H13 steel pin coated with boron utilizing a cathodic arc plasma generation process.

COATING TECHNOLOGY

Coating Process

HY-Tech Research Corporation has developed and patented a unique coating technology which allows the deposition of boron in an economically viable way. Typically, boron is extremely difficult to work with and deposit onto a substrate. It does not sputter well and it cannot be electroplated. Typically, gaseous compounds for use in CVD are toxic and/or explosive. However, HY-Tech's method produces a supersonic plume of boron plasma (fully ionized gas) out of solid feedstock. The latter, made of consolidated boron powders, is the cathode in a type of electrical discharge referred to as a vacuum (or cathodic) arc [9, 10]. Figure 1 shows a typical

 505/856-7188 ISSN 0737-5921
47th Annual Technical Conference Proceedings (April 24–29, 2004) Dallas, TX USA

cathodic arc setup. This technology has lately become a very common type of PVD because of its superior rate of deposition over magnetron sputtering. However, its application is limited to metal cathodes for the production of metal nitride coatings or graphite cathodes for the deposition of amorphous carbon coatings.

One of the key elements of successful development of a cathodic arc with a non-metal boron cathode has been in the sintering technology for the consolidation of boron cathodes from powder. Since the vacuum arc is a very intense electrical discharge, it produces immense stresses on the cathode, where the footprint of the discharge is anchored. Similar to metal-cathode vacuum arcs, the footprint is usually in the form of one or more non-stationary spots of about 10μm in diameter. These spots carry current densities as high as 100,000,000 amperes per square centimeter. They are extremely bright. This is where solid is directly converted to the plasma state. The specially processed boron cathodes are able to withstand the stresses induced on them by this process. Even these robust cathodes must be heated to over 800°C to make the boron cathode conductive [11]. Compared to previous attempts at a dc arc with a B cathode [11], these special cathodes allow for uniform erosion without transition to a diffuse (non-spot) mode.

In this new technique, the arc is struck from an anode to the pure boron cathode, producing a dense plasma plume of boron ions with 100% ionization, and a rather high energy. Polarization of the target can increase the energy as the ions approach the target. Because of the density of the plasma, the resulting thin plasma sheath, and the polarization, the ability to treat intricate shapes helps make this a unique and useful coating technique. Although the cathodic arc is not unique to boron, the boron and boron carbide cathodes are unique. Other coating materials of interest for dies, such as chrome nitride, are also best generated by cathodic arc. In fact, good results have been reported by a number of researchers using metal cathodic arc in a nitrogen background to reactively deposit CrN and TiN, sometimes doped with other materials [2, 6].

COATING EQUIPMENT

Since the plume produced is fully ionized, it can be guided with the aid of a magnetic solenoid. Proper control of the electrical biasing of the substrate can not only help with the adhesion of the coating, but also can allow for conformal coating of non-planar substrates (as illustrated in Figure 1).

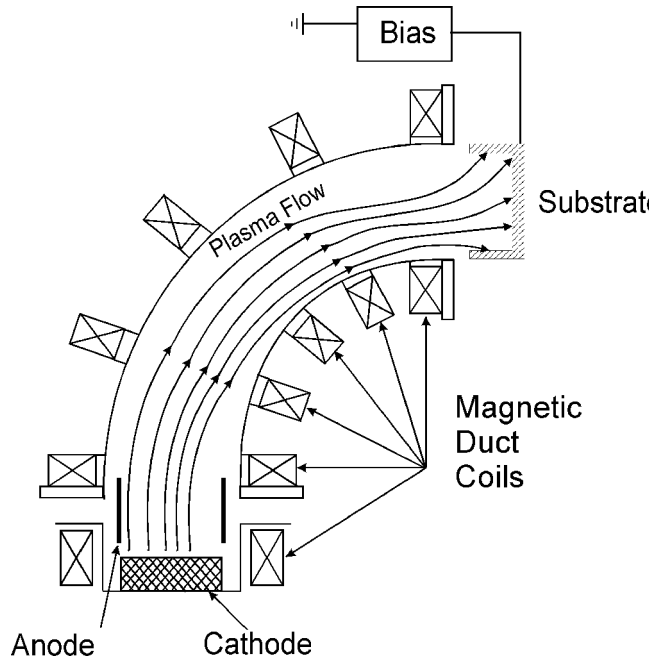

Figure 1: Illustration of typical cathodic (vacuum) arc deposition with a 90° bend magnetic duct to filter out solid or liquid particle debris from the solid cathode, which is also the source of the material converted into fully-ionized plasma guided by the duct.

Typically a curved solenoid is used to take the substrate out of the line-of-site of the source. This prevents any debris that can also come from the cathode (small fragments or molten material) from depositing onto the substrate. This debris, usually referred to in the literature as macro-particles, is the main drawback of the vacuum arc as a thin film deposition process. However, the deposition rates obtained with this technique far exceed those of other plasma-discharge deposition methods; even after substantial plume attenuation in a filter (simple curved solenoids transmit only about 10% per turn). The setup at HY-Tech used for the studies reported here did not have an optimized filter and the coatings incorporated a significant number of macro particles in most regions of cylindrical samples coated. However, there were some particle free regions and this provided an opportunity to study the effect of the macro particles on soldering by molten Al.

Two important advantages for the vacuum arc deposition process for this application stem from the fully ionized nature

of the plasma stream: (1) the effective use of substrate biasing to guide the ions to surfaces that may be at various angles with respect to the stream—an important benefit for die-casting dies whose shapes tend to have complex (non-planar) surfaces (often including crevices hard to reach with line-of-site deposition techniques); (2) the potential for control of the energies with which the ions impinge onto the surface, allowing variations of the degree and nature of atomistic mixing that will occur at the coating-substrate interface. This mixing is expected to determine the adhesion of the coating, an important property. In the case of boron, the primary effect of the energetic ions has appeared to be enhanced diffusion into the steel substrate, as discussed in this paper.

Coating Material Selection

Thermodynamic calculations suggested that boron would be an excellent candidate for a non-wetting coating that would also bond well to an iron-based substrate (e.g., H13 steel). A short explanation behind this hypothesis is described in the Results and Discussion Section below. Figure 2 shows the results of a Rutherford backscattering (RBS) analysis of an area for which the entire boron deposition had in-diffused over a depth of 0.5 microns.

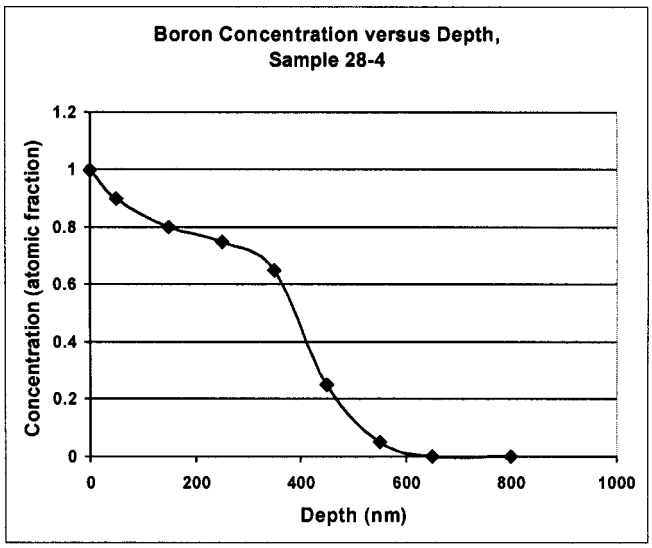

Figure 2: Boron concentration versus depth for sample 28-4 derived for the RBS data. Almost all the boron has reacted/ diffused inward to yield a reaction layer ~0.5 microns thick.

Thus, there was not actually a coating, but a surface alloy. Such results were not consistent from one area to the next. Differences probably depend on temperatures reached during coating. This result confirms the expected tendency for strong bonding, as was predicted from the thermodynamics calculations.

EXPERIMENTAL TESTING

Sample Preparation

The H13 substrate samples were 1/2 inch diameter x 1 inch long cylinders coated using the HYBron™ process of HY-Tech Research Corporation. This process is based on the cathodic arc technique. This technique evaporates boron from a solid cathode and converts the vapor into a supersonic, fully ionized boron plasma. The resulting coating is primarily pure boron, a naturally hard amorphous material. A small oxygen concentration improves the coating properties, e.g. improved adhesion and a low modulus of elasticity [12]. The samples were mounted with the cylindrical axis perpendicular to the plasma plume. Some rotation of the sample about its axis of symmetry was used to attempt uniform deposition. This was not achieved because of insufficient control of the deposition rate in the present system. The free end of the cylindrical substrate, which was at 90° with respect to plasma plume, was coated as well. This region of the coating was entirely free of macro particle contamination.

Bench Testing

Using a bench-scale soldering test apparatus (referred to as the dipper) (Figure 3) designed and built at Oak Ridge National Laboratory (ORNL), dip tests were conducted in molten aluminum to evaluate the soldering and thermal fatigue resistance of H13 die casting pins that were coated with boron utilizing the cathodic arc technique. Using this coating for automotive die applications seemed ideal based on previous thermodynamic calculations that indicated a positive, i.e. repulsive heat of formation, interaction between B-Al (Figure 4). The test was designed for testing the compatibility of coatings for H13 steel die-casting components, e.g. die pins. In order to simulate the die casting operational process steps, three stations were incorporated into the dipper testing apparatus: a die lubrication station, an air blast station, and the furnace containing molten aluminum. Programmable computer controls enable the control of each process step, the dipping times in the die lubricant in the air spray, and in the molten aluminum. The temperatures are set based on the selected liquid metal aluminum alloy. Prior to starting the trial cycles, the sample is first brought to the required molten alloy temperature, and then dipping trials are initiated. A testing cycle consists of first dipping the pin into the die lubricant, followed by an air blast, then a dip into the (~650°C - 700°C) molten aluminum alloy, followed by quenching in the cooled liquid lubrication.

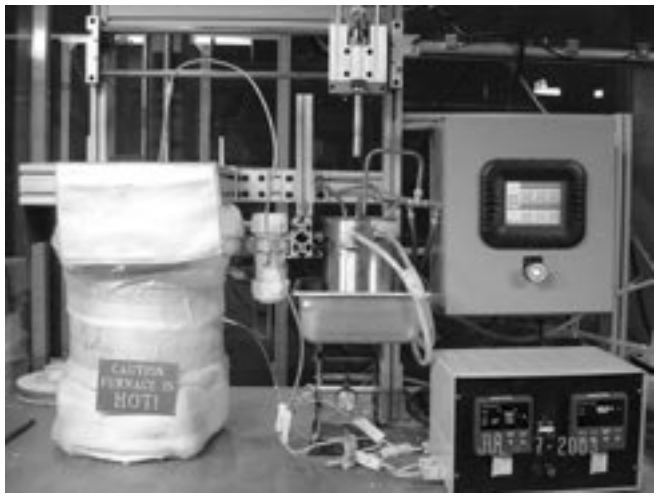

Figure 3: Schematic illustration of automated dipper test apparatus set-up.

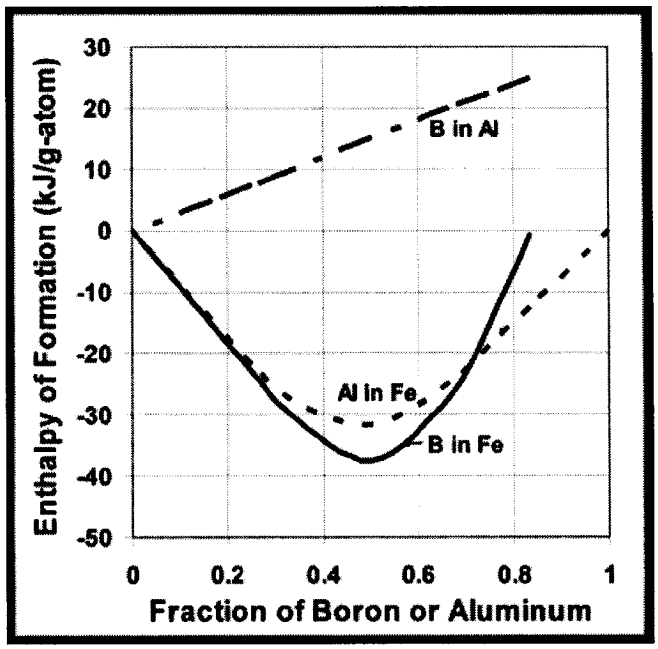

Figure 4: Illustration of thermodynamics of relevant alloy systems.

EXPERIMENTAL RESULTS

Preliminary baseline soldering trials and analyses had previously been completed on uncoated H13 pins, with results demonstrating that soldering occurred on uncoated H13 pins after only eight dipper cycles. After only eight dipper cycles, the uncoated H13 pin exhibited soldering along its surface, and on the bottom of the pin. However, experimental dipper tests conducted on the B coated pins, under the same experimental dipper test conditions, confirmed that the molten aluminum did not wet the B coating, as predicted by the thermodynamic calculations. The B-coated pin exhibited no soldering where the B coating was free of macro particles. In particular, no macro particles formed on the end of the pin during the cathodic arc process. Figure 5 shows the appearance of the end of a boron-coated steel pin sample after 50 dipper cycles demonstrating the resistance of the boron coating to wetting by the molten aluminum, as predicted by thermodynamic data.

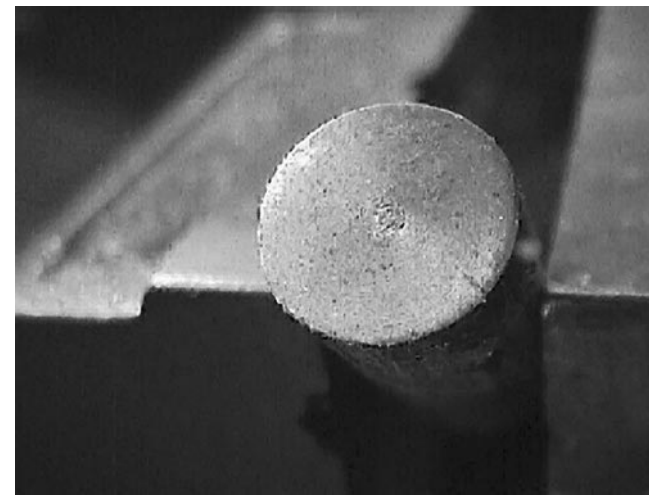

Figure 5: Macro-particle-free end of a boron coated steel pin exhibiting no apparent soldering after 50 dipper cycles in molten aluminum. Typical cylindrical pin dimensions are 2" long x 0.75" in diameter.

Subsequent Rutherford Backscattering Spectroscopy (RBS) of the sample analyzed demonstrated the most dramatic effect. This test sample had more boron than the coated samples, and virtually all of it had diffused into a reaction layer ~ 0.5 microns thick. The original data, together with a fit by simulation, used six layers in the composition grade. Figure 2 is a transposition of this data to boron concentration versus depth. These data are for the cylinder wall. This reaction effect is assumed to be kinetically facilitated by heating during deposition, although the tendency to react is intrinsic (see below).

This reaction result illustrates part of the original theory hypothesized, i.e. that the boron will have a strong tendency to bond to the steel substrate. The thickness of this reaction layer suggests that the interstitial B diffuses readily, but since the solid solubility is low, the diffusion mechanism may also involve some successive bonding, perhaps as a compound, then release of the B, further diffusion and, re-precipitation. The phase diagram for the Fe-B system exhibits a eutectic at 1174°C. Boron does not lower the austenite transition temperature. Experimental results demonstrated that the boron was highly adhesive during testing in the molten aluminum. This reaction bonding tendency appears to eliminate the need for a separate bonding layer, contrary to compounds like CrN

or TiAlN [1]. Although one could argue that much of the chemical potential is used in forming the compounds, and so little reactivity would be left over for bonding to the substrate, this appears not to be true for B. This argument appears to be true for an element that is protected against a rapid reaction (oxidation) on the outside by a passive oxide, e.g. Ti and Al. Also, although boron is attractively bonded to steel, it has a repulsive chemical interaction with Al. Figure 3 illustrates the thermodynamic calculations for the heats of formation of three pertinent alloy systems over a composition range. The exothermic reaction with Fe-based systems is predicted for B and Al, thus supporting the bonding of B to steel and the wetting of Al. In addition, the heat of formation in the B-Al system is positive, indicating little tendency to react. Moreover, the terminal heats of solution were very favorable for no wetting of B by Al. The value for B in Al was 30 kJ/g-atom, indicating a possibility for slight solubility of B in Al at high temperature. The eutectic composition is at 0.055 at. % B at 660°C. At the opposite composition extreme, there is no possibility for reactivity of Al in solid B. Thus, it was anticipated that the B coating would be highly adherent to steel, but would also be resistant to wetting by Al.

DISCUSSION

The fact that the sample was non-uniform over the area in soldering performance is probably explained by the macro particles. Many of these particles bounce off of a hard material such as H13 steel, but some stick for a while and then fall off during handling, etc. If a particle is sticking during coating it screens the area and when it falls off it leaves an unprotected area. A similar result was observed with 52100 steel. Failures start in the pores left by macro particles. In the present case, the first sign of failure was a mechanical clinging, e.g. a "Velcro"-like effect due to apparent roughness of the surface for the areas that (hypothetically) contained pores. Upon solidification the aluminum fell off as a solid, leaving the coated surface as-new. Apparently, wetting finally occurred for these areas.

This same idea may explain why the end of the sample never became wetted. As was described above, during coating, the cylinder wall was more or less perpendicular to the plume propagation direction. Because of polarization and sheath effects, the end could still be exposed to plasma, but the macro particles passed the end at grazing angles and would have tended to have been reflected from this hard substrate. Thus the end may not have had pores. The remedy in all cases under these ideas is an adequate filter. The coating on the end was highly in-diffused after the test. Although the number of cycles was small, heat checking (cracking) was also not observed.

In that regard, there is room for speculation on known atomic mechanisms in all aspects of performance. The in-diffusion of boron has been mentioned. Adhesion would definitely not be an issue. The fact that the in-diffusion was much greater after the tests than before confirms the high mobility of the boron at the test temperature. Such a mobile agent in the lattice in the near-surface region could move to ameliorate stresses in accordance with text book metallurgical mechanisms, such as the Snoek effect or the Cottrell-Bilby mechanism, wherein regions of high compressive stress are vacated by the mobile solute and precipitation occurs in regions of tension.

Finally, it might be noted that the interaction of the melt may be mainly with the boron oxide at the interface, rather than the elemental boron. Boron has a strong passivating oxide which is reducible by elemental aluminum. If some oxide is somehow removed by a combination of chemical and wear effects due to impact of the molten Al, and if no boron is available for new oxidation except that which has diffused in, a new oxide will form from the most accessible boron near the surface. This denuded zone will create a Fick's law or entropic chemical force, which will tend to make some of the boron come back out to fill it. Thus the in-diffused boron could become a reservoir for reformation of surface oxide.

CONCLUSIONS

1. Experimental results have confirmed the primary goal and hypothesis of this work, i.e. based on thermodynamic-based predictions, cathodic arc vacuum deposited boron coatings would resist wetting by aluminum.
2. The cathodic vacuum deposited boron coating strongly adheres to the substrate, while simultaneously resisting wetting by aluminum as predicted/hypothesized from thermodynamic calculations.
3. Despite the developmental state of this processing technology, all surface areas where the boron was deposited uniformly (i.e. without boron particle inclusions) demonstrated that the aluminum did not wet the H13 pin.
4. No cracking occurred in the coating or the substrate during or after the soldering/dipper bench tests.
5. Macro-particle management is the biggest challenge for the implementation of this technology, but preliminary conceptual equipment designs indicate that this is a solvable issue.
6. Boron shows promise as a life extension coating for die casting applications.
7. Further research and development would catapult this process technology into an industrially robust coating solution for the prevention of soldering and thermal fatigue of aluminum casting dies.

ACKNOWLEDGMENTS

Work at ORNL was sponsored by US DOE, Office of Energy Efficiency and Renewable Energy, Industrial Technologies Program, Industrial Materials for the Future, under contract No. DE AC05-00OR22725 with UT-Battelle, LLC. Research at HY-Tech Research Corporation was sponsored by the National Science Foundation under SBIR Award Number 0078385.

REFERENCES

1. Y. Wang, "A Study of PVD Coatings and Die Materials for Extended Die-Casting Die Life", Surface and Coatings Tech., 95-95, (1-3), 60, 1997.

2. C. Mitterer, F. Holler, F. Ustel, and D. Heim, Surface and Coatings Tech., "Application of Hard Coatings in Aluminum Die Castings – Soldering, Erosion, and Thermal Fatigue Behavior", 125 (1-3), 1999.

3. M.J. Mirtich, N. Cuo-Yo, and J.F. Wallace, "Sputtered Protective Coatings for Die-casting Dies", Thin Films, 84 (3), 295, 1981.

4. V.I. Gorokhovsky, D.G. Bhat, R. Shivpuri, K. Kulkarni, R. Bhattacharya, and A.K. Rai, "Characterization of Large Area Filtered Arc Deposition Technology", Surface and Coatings Tech., 140 (3), 121, 2001.

5. R. Shivpuri, Y-L. Chu, K. Venkatesan, J.R. Conrad, K. Sridharan, M. Shamim, and R.P. Fetherson, "An Evaluation of Metallic Coatings for Erosive Wear in Die Casting Applications", Wear, 192 (1-2), 49, 1996.

6. R.S. Aharonov, S. Chellapilla, B. Janoss, R. Shivpuri, and A. Lakare, "An Investigation of the Corrosion of H13 Steel Coated CrN in Molten Aluminum Alloys: Effect of Steel Surface Preparation and Coating Thickness", NADCA, 1999.

7. M. Nastasi, X-M. He, K.C. Walter, M. Hakovirta, and M. Trkula, Surface and Coatings Tech., 136, 162, 2001.

8. G. Mackiewicz Ludtka, C.A. Blue, R. Smith, et al., private communication (2001).

9. P.J. Martin, D.M. Sanders, and R.L. Boxman, eds., "Handbook of Vacuum Arc Science and Technology: Fundamentals and Applications", Noyes Publications, Park Ridge, N.J., 1995.

10. I.G. Brown, "Cathodic Arc Deposition of Films", Ann. Rev. Mater. Sci.,28, 243, 1998.

11. F. Richter, S. Peter, V.B. Filippov, et al., "Characteristics of the cathode arc discharge with a hot boron cathode," IEEE Transactions on Plasma Science, 27, No. 4, pp. 1079-83, 1999.

12. C.C. Klepper, R.C. Hazelton, J.M. Williams, et al., "Amorphous boron coatings produced with vacuum arc deposition technology", J. Vac. Sci. Technol. A20 (3), 725, 2002.

New Modular Roll-to-Roll PVD Web Coater For Clean Room Production

R. Kukla, H.G. Lotz, R. Ludwig, and P. Sauer,
Applied Films GmbH & Co. KG, Alzenau, Germany

Key Words: Web equipment design and construction; Web coating applications; Sputter deposition; Thermal evaporation

ABSTRACT

Roll-to-roll sputter web coaters for ITO deposition and for window films have been built since the late 1970's. They are designed for large volume production, with web widths up to 2m. State of the art sputter web coaters are large, heavy, and not designed to be integrated into clean rooms.

Growing products like flexible displays, flexible printed circuit boards with high line density, flexible solar cells, etc. require low particle generation, low background pressure and the possibility to integrate the coater into a clean room. Load locks for the unwinder and rewinder are often required to keep the process sources under vacuum during roll exchange. High process flexibility is necessary, particularly the possibility to integrate different coating technologies like sputtering and evaporation in one web coater. In-line process control is mandatory to guarantee high yield.

We present a new PVD roll coater design, which is optimized for the above-mentioned requirements and is modularly built, similar to in-line coaters for glass sheets.

INTRODUCTION

Since the late 1970's, roll-to-roll sputter web coaters have been built for large volume production of ITO and of window films [1,2]. Typical web widths were in the range of 1.6 m to 2.1 m. All functions (unwinding, pre-treatment, coating, post-treatment and rewinding) were installed in one common vacuum vessel. These coaters are large and heavy with a height of up to 5 m, a footprint in the range of 15 m x 20 m, and total weight, including power supplies and cabinets, of up to 80t. These machines could not be integrated in clean rooms of standard sizes.

NEW PRODUCTS AND THEIR REQUIREMENTS

In the last three to five years, new products have been developed in the laboratories which put unknown requirements on mass production roll coaters:

The line density of Flexible Printed Circuit Boards (FPCB) has been increased. The line width of the copper structures decreased correspondingly. This enhances the requirement on the adhesion strength of the sputter deposited copper layers. Thus, improved pre-treatment processes and pre-treatment tools are needed. Furthermore, with smaller lines, each dust particle on the flexible substrate film may result in an interruption of the latter on etched path of current. The same is true for ITO top-electrodes on touch screen displays. This reduced tolerance against dust particles requires a change of the coater design. There should be no moving parts and no dust generating operations positioned above the coating drum and above the deposition sources and the coater should be small enough to be integrated into a clean room.

Flexible displays with Organic Light Emitting Devices (OLED) [3] require metal evaporator sources for the cathodes, evaporators for the organic polymers, and super barrier layers [4] for in-line encapsulation of the highly water-sensible OLED layers. That means next generation PVD web coaters must be flexible with regard to the deposition technology, e.g. they should be capable of incorporating sputter-sources as well as evaporation- and PECVD-sources.

Load locks for the unwinder and rewinder are often required to keep the process sources under vacuum during roll exchange. In-line process control is mandatory to guarantee high-yield.

MACHINE CONCEPT

Modular Design

In the new modular roll coater design of the SMARTWEB™, schematically shown in Figure 1, each function is installed in a separate vacuum vessel containing the unwinder module, process module and rewinder module. Each process module can be equipped with a maximum of three deposition sources in separately pumped process compartments.

 505/856-7188 ISSN 0737-5921
47th Annual Technical Conference Proceedings (April 24–29, 2004) Dallas, TX USA

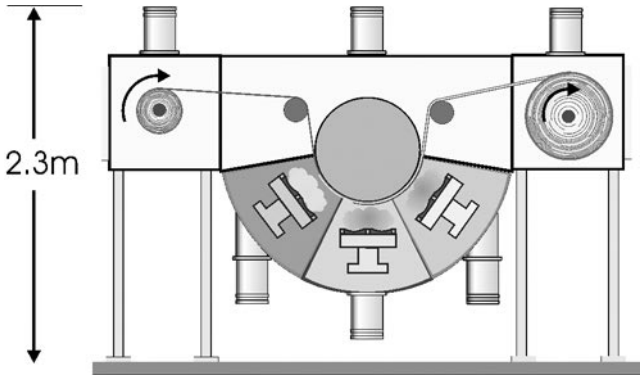

Figure 1: Schematic cross section of a SMARTWEB™ with three deposition sources.

In the case of more than three required deposition sources, a second process module will be added (see Figure 2).

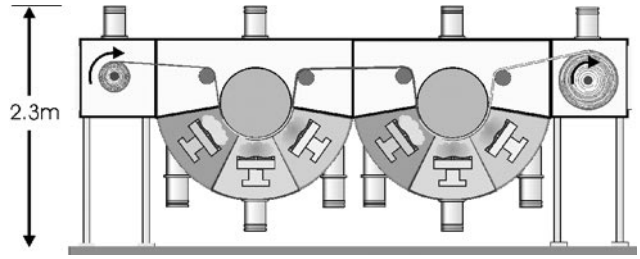

Figure 2: Schematic cross section of a SMARTWEB™ with six deposition sources.

For service of the coating tools, e.g. replacement of targets, the front wall of the process vessel is driven aside by a motor drive, as shown in Figure 3. Now the deposition sources are easy accessible and the coating drum shields can be replaced for cleaning. For the exchange of unwinder roll and rewinder roll, the clamps that fix the winders in their position during operation are opened by a pneumatic cylinder and the winders are moved out on rails. For processes where the deposition sources (e.g. sputter targets or evaporation crucibles) are sensitive to contamination by air, load locks are available in extra chambers, which are positioned between the winder chambers and the process chambers. Patents for the load locks are pending.

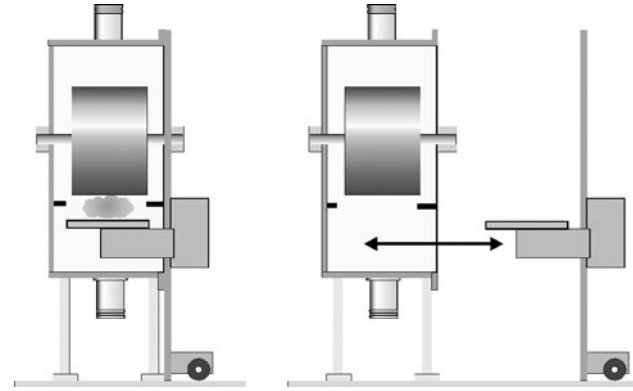

Figure 3: Side views of a SMARTWEB™, left side: in sputter operation, right side: opened for target exchange.

Vacuum System

Every single compartment (unwinder module, winding section of the process module, each process compartment and rewinder module) is pumped by turbomolecular pumps plus cryogenic pumps. Thus a base pressure in the 10^{-7} mbar range can be reached.

In contrast to the standard design of roll coaters, where the winding system is driven out of the vessel for roll exchange, the SMARTWEB™ coating drum is fixed in the process module. There is no relative motion between coating drum and chamber separation walls, other than rotation of the drum. Thus, the slits between the chamber separation walls and the coating drum can be adjusted to very small height. This results in a pressure separation factor of 200:1 from winding section to process section and between two neighboring process sections. This extremely good chamber separation allows for performing processes with very different gas composition in neighboring chambers without the need of intermediate pumping sections. One example is a reactive sputter process in an argon-oxygen atmosphere in one subchamber, and a non-reactive process like the sputtering of silver in the neighboring chamber.

Table 1: Machine Data

Web width	400, 600 or 800	mm
Web thickness	10 – 200	µm
Web speed	0.5 - 10	m/min
No of coating sources	1-6	
Max. Height	2.5	m
Footprint (with 3 sources)	7 x 5	m^2

DEPOSITION SOURCES

Each process compartment of the SMARTWEB™ can be equipped with a variety of coating sources, like

- Planar DC magnetron
- Rotatable DC magnetron
- TwinMag™ AC magnetrons
- Linear organic material evaporator
- Linear metal evaporator
- PECVD source: RF Hollow Anode

Three of these sources are described in detail below.

Planar DC Magnetron ToraMag™

A new small DC magnetron has been developed with a target width of 160 mm. It realizes a target utilization of >35% with an optimized arrangement of permanent magnets. The magnets are not in contact with cooling water (patent pending). The maximum deposition rate for copper is 250 nm at a web speed of 1m/min. Figure 4 shows the measured erosion profile of a copper target with a thickness of 18 mm.

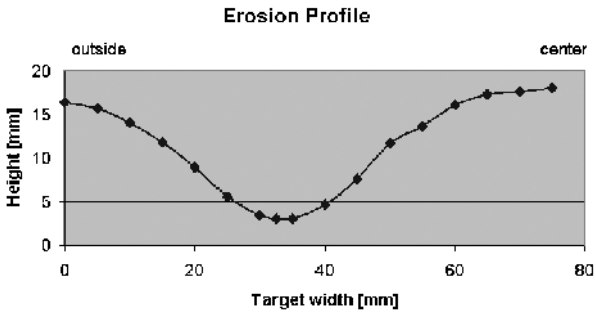

Figure 4: Erosion profile of SMARTWEB™ cathode target utilization, measured by weighing, is 35%.

Linear Organic Material Evaporator

A new evaporator (Figure 5) [5] has been developed for the deposition of organic materials for OLED displays. After heating up the OLED material inside a crucible, the vaporized material spreads out through a heated pipe, which ends in a column with a row of nozzles. This ensures a uniform thickness distribution across the web width of up to 800 mm.

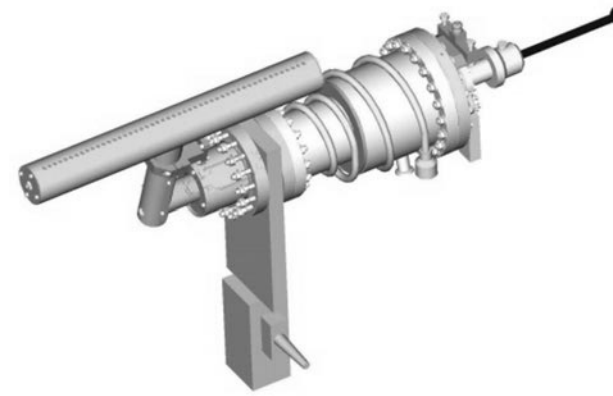

Figure 5: Schematic of the linear evaporator for organic materials.

A valve between crucible and evaporator column allows for easy refilling of the crucible without venting the process chamber. Temperature of crucible and column can be controlled independently. The organic material is only in contact with inert material (quartz), so it is prevented from contamination.

Plasma CVD Source "Hollow Anode"

For Plasma Enhanced Chemical Vapor Deposition processes with high ionization density of the vapor and with high ion energies, the RF-Hollow Anode has been adapted to the SMARTWEB™ geometry. The capabilities of the Hollow Anode have been demonstrated in electron beam web coaters TOPBEAM™, as well as in sputter web coaters and in-line coaters. Set-up and performance of the Hollow Anode have been described in detail [6]. With an asymmetrical 13.56 MHz glow discharge and a plasma confinement in a hollow electrode, the Hollow Anode works in a pressure range of $5x10^{-3}$ to $5x10^{-2}$ mbar. The achievable bias voltages of the web range up to 1100V, creating ion impact energies on the web of several 100 eV.

Figure 6 shows a 1.46 m wide Hollow Anode, installed in an electron beam evaporation roll coater for pre-treatment and/or pre-deposition of base layers. For use in the SMARTWEB™, the Hollow Anode was scaled down in length and width.

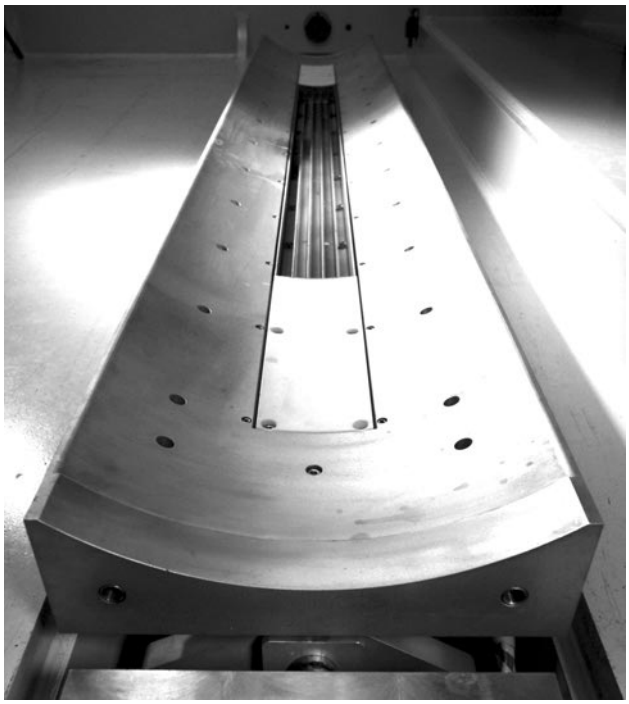

Figure 6: Example of a Hollow Anode in an electron beam evaporation roll coater.

PRE- AND POST-TREATMENT

In-line pre-treatment of the substrate web is often necessary to remove surface layers of water or to remove weakly bound layers of low molecular weight components of the polymeric web. Another reason to use pre-treatment is to improve the adhesion of the deposited film by increasing the free surface energy of the substrate film. Post-treatment of the freshly deposited film may be used to densify the layers and to improve the adhesion properties, e.g. for lamination to another film that is to take place in the next production step of compound films.

In order to provide optimum pre-treatment for different types of web-substrate materials and for various kinds of coating processes and coating materials, the SMARTWEB™ can be equipped with three different pre-treatment tools.

Magnetically Enhanced Glow Discharge: TreatMag™
Pre-treatment of the web with a magnetically enhanced glow discharge is standard for most high performance products with sputtered layers. Because of the proven increase of adhesion, it also is used in many evaporation coaters, where aluminum is evaporated from resistance-heated boats for packaging applications. The ion energies of a magnetically enhanced DC glow discharge are typically less than 70 eV.

Linear Ion Sources
Linear ion sources are available from a variety of sub-suppliers. They deliver higher ion energies of >70 eV, but are limited in the ion-flux, they can provide.

RF-Hollow Anode
The RF-Hollow Anode, mentioned already as a possible deposition source, can also be used as a tool for pre-treatment and post-treatment when run in an argon-atmosphere or with a mixture of argon and oxygen. This source delivers the highest ion-energies (several 100 eV) together with higher plasma density, when compared to the previous tools.

INLINE MEASUREMENT

In-line measurement tools for the following physical properties are available for the SMARTWEB™:

- Optical Density
- Optical Transmission / Reflection as function of wavelength (380 nm - 780 nm)
- Sheet Resistivity: Roll to roll (measurement in contact with the as-deposited layer, averaged over web width)
- Sheet Resistivity: Eddy current (contactless, locally)

CONCLUSION

New products that are on the way to mass production, like flexible displays, FPCBs with high line density and flexible solar cells, pose new requirements to mass production roll coaters, including bringing a combination of different deposition technologies in one single coater, low particle generation, and clean room compatibility.

In order to fulfill these requirements, the established design of roll-coaters had to be changed. We have developed a modular PVD roll-to-roll coater with a high flexibility regarding the possible coating technologies, pre- and post-treatment tools and in-line measuring devices. With the “linear” arrangement of the vacuum chambers for the different functions, two requirements are fulfilled at the same time, specifically low particle generation in the coating zone by a minimum number of moving parts on top of the coating drum, and small size, especially low height, which enables the coater to be installed in a clean room.

REFERENCES

1. R.L. Cormia, J.B. Fenn Jr., H. Memarian, and G. Ringer, "Roll-to-Roll Coating of Indium Tin Oxide – A Status Report," 41st Annual Technical Conference Proceedings of the Society of Vacuum Coaters, 452, 1998.

2. J. Fenn Jr., W. Kittler Jr., D. Lievens, R. Ludwig, G. Philips, and A. Taylor, "Roll-to-Roll Sputter Web Coater - A Status Report," 41st Annual Technical Conference Proceedings of the Society of Vacuum Coaters, 463, 1998.

3. E.H. Webster, "Better Displays with Organic Films," Scientific American, February 2004.

4. N.M. Rutherford, "Plastic Barrier Substrate and Thin Film Encapsulation: Progress toward Manufacturability," USDC Flexible Displays & Microelectronics Conf. Proc., CD, Chapter 6.3, 2003.

5. U. Hoffmann, P. Netuschil, P. Sauer, H.-G Lotz, A. Klöppel, M. Bender, and J. Trube, "New In-Line machine concept for OLED manufacturing," SID 32, Boston Digest of Technical Paper, 891, 2002.

6. M. Geisler, R. Kukla, J. Bartella, G. Hoffmann, R. Ludwig, and D. Wagner, "Large Scale RF-Plasma Tool for Ion Assisted Pre-Treatment and Deposition," Proc. of 14th Int. Conf. On Vacuum Web Coating, Reno, Nevada, 119, 2000.

Innovative Production of High Quality Optical Coatings for Applications in Optics and Optoelectronics

M. Scherer, J. Pistner, and W. Lehnert, Leybold Optics GmbH, Alzenau, Germany

Key Words: Sputter deposition; Optically variable coatings; Optical coating equipment; Monitoring (in situ)

ABSTRACT

Future production of high quality optical coatings for applications in laser optics, emerging optoelectronic devices, and wafer type substrates, asks for both the precise preparation of low loss multilayer stacks and a clean-room compatible innovative deposition process. In addition, a cost-effective thin film filter production is required in order to transfer new developments, like ultra fast pulse laser techniques, from research to economical products and applications. One of the most promising candidates is magnetron sputtering due to the potential of excellent film properties, a fully automated clean-room compatible manufacturing process and a high productivity. The paper reports on a sputtering tool with load lock and cassette substrate handling system, which combines reactive mid-frequency sputtering with dual magnetrons and an inductively coupled RF plasma source. This combination together with an in situ optical monitoring system (OMS 4000), optical multilayer coatings with outstanding properties and reproducibility are achieved at high deposition rates.

INTRODUCTION

State-of-the-art in precision optics are box coaters with plasma ion assisted e-beam evaporation with high throughput, high flexibility, and excellent film properties, but has limitations in a fully automated cleanroom compatible manufacturing process.

In the fields of precision optics, especially laser optics and micro-optical devices, and optoelectronics with increasing miniaturization and integration of optical and electronic functions, there is an increasing demand for production processes with low particle/defects generation. Consequently, a cleanroom compatible coating solution is needed with automated substrate handling under high vacuum conditions. The trend is toward a small coating system for flexible small to medium batch production with a very high yield and precision, and a stable oxide deposition process with high rates for a high throughput. From the production point of view, a long maintenance-free operation time and easy production integration are required.

It is well known that highest optical quality coatings for laser applications are achieved with ion beam sputtering tools, but with limitations in throughput due to very small deposition rates, even on relatively small substrate areas.

On the other hand, magnetron sputtering can offer similar film properties, but with a much higher productivity and easier process control. Magnetron sputtering is a well established technique for silicon wafer processing in semiconductor chip manufacturing. Load lock systems with integrated cassette substrate handling are working fully automatic at an extreme low particle and defect level.

INNOVATIVE SPUTTERING TECHNOLOGY

Basic Tool Concept

For the innovative production of high quality optical coatings, we have combined a cassette substrate handling system, according to semiconductor standard, with a newly designed sputtering chamber optimized for the dynamic deposition of low loss multilayer stacks of low and high index materials with a high throughput.

The sputtering tool, as shown in Figure 1, consists of a cassette module, a transfer module with vacuum robot, and the sputtering module.

Figure 1: Sputtering tool for the fully automated cleanroom production of optical coatings.

 505/856-7188 ISN 0737-5921

47th Annual Technical Conference Proceedings (April 24–29, 2004) Dallas, TX USA

The modules are separated by high vacuum valves and individually pumped by turbo-molecular pumps. Typically, only the cassette module is integrated in the cleanroom area. In order to process substrates, only the cassette module has to be vented to atmosphere to exchange the substrate cassette. After the door is closed, a fully automated production cycle is started, including the substrate transfer from and to the sputtering chamber. As a result, an extreme clean production process can be realized due to minimum manual handling and stable high vacuum conditions in the sputtering chamber (E-7 mbar range). Furthermore, stable and reproducible conditions can be maintained for a full week, a three shift operation due to the lifetime of the sputtering material.

Sputtering Module for Precise Optical Coatings

The sputtering module is equipped with a high speed substrate turntable with a maximum speed of up to 250 rpm. This high speed guarantees an extreme uniformity from substrate to substrate within one batch. In the standard configuration, 16 substrate/holder positions are available on the turntable for flat or slightly curved substrates with a diameter of up to 100mm (other customized substrate dimensions and a diameter of up to 150mm optional). Basically, the sputtering module consists of two sputtering units (MF TwinMag), one for low and one for high index materials and a RF plasma source. For pre-sputtering and stabilization of the reactive process, the tool is equipped with a central stutter.

In Situ Optical Thickness Monitoring

A direct on-substrate optical monitoring is performed in an intermittent mode on an arbitrarily selected substrate position on the rotating turntable. Depending on the application, single wavelength and multi-wavelength optical monitoring are available. This results in superior precision and reproducibility, since tooling factors—as used in monitoring on witness glasses—are not involved. As a consequence, optical designs can be directly and fast transferred into production. Details of the in situ monitoring are given in Reference 1.

Reactive Sputtering Process

In 1992 we introduced reactive MF dual magnetron sputtering for the industrial production of dielectric materials [2]. This technique became very popular, especially for applications in large area coating of architectural glass and LCD displays. In spite of this success there is still a demand for an economic sputtering solution for high quality optical multilayer coatings with low loss. Solutions which are dealing with the deposition of thin metal layers followed by a separate oxidation process are discussed in Reference 3.

Our solution is reactive MF dual magnetron sputtering (MF TwinMag) combined with a separated inductively coupled RF plasma source (ECWR). By depositing a layer with optimized composition during reactive MF sputtering, both high deposition rates and low loss coatings with excellent properties are achieved with the combined process. While the reactive MF sputtering process is typically partial pressure controlled by a so called lambda-probe technique, the following reactive plasma ion assist process is working at constant power and constant gas flow. These conditions lead to a stable sputtering process free of μ-arcing.

RESULTS

Single Layers

Single layers of SiO_2, Ta_2O_5 and Nb_2O_5 with a thickness of 500nm were deposited on B270 glass substrates and on silicon wafer to measure the optical properties n and k by a spectral photometer and by ellipsometry and the surface roughness on silicon wafer by AFM. The dispersive refractive indices of these layers obtained by ellipsometry and shown in Figure 2 are higher than the one achievable using plasma ion assisted electron beam evaporation, indicating very dense layers. As a consequence, the layers are extremely shift-free.

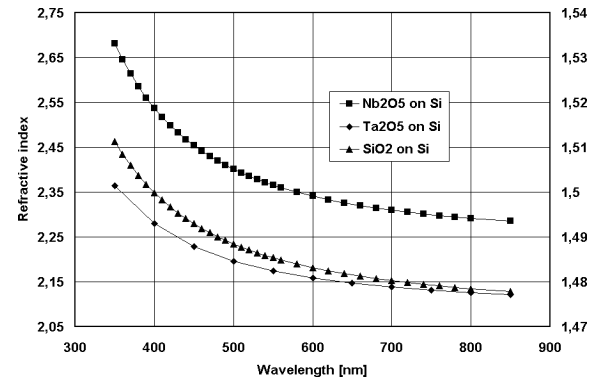

Figure 2: Dispersive refractive index of SiO_2, Ta_2O_5 and Nb_2O_5 measured by ellipsometry on silicon wafer.

In Table 1 the optical properties, the surface roughness, and the dynamic deposition rate are summarized. At a wavelength of 550nm the measured losses on 500nm thick single layers on B270 glass substrates were always below the detection limit of 0.1% of the photometer corresponding to k values < 1 E-4. The refractive index of Nb_2O_5 is pretty high, with 2,37 at 550nm, and the absorption edge is as low as 350nm. This makes Nb_2O_5 very attractive as high index material for VIS/NIR applications. The spectral transmission of SiO_2 on quartz glass follows the uncoated quartz substrate indicating no extra absorption down to a wavelength of 200nm. The smooth surface of the investigated materials between 0.2 and 0.4nm RMS on silicon wafer are related to the enhanced ion bombardment of the MF dual magnetron sputtering process. SiO_2 and Nb_2O_5 films exhibit medium compressive stress values between 200 and 400 MPa. The stress level could be altered by varying the employed sputter gas pressure. All materials show a high deposition rate between 0.45 and 0.7nm/s which is comparable to electron beam evaporation. The achieved

thickness uniformity on 100mm diameter substrates is better than ± 0.4%.

Table 1: Optical properties, surface roughness and dynamic deposition rate of 500nm thick single layers.

Material	Ref. index n @550nm	Loss K @ 550nm	Roughness RMS nm/s	Rate
SiO_2	1.485	< 1 E-4	0.36	0.45
Ta_2O_5	2.17	< 1 E-4	0.21	0.7
Nb_2O_5	2.37	< 1 E-4	0.25	0.55

Multilayer Coatings

The true performance of a deposition system for optical applications can only be judged by the quality of multilayer stacks. In order to demonstrate both the low loss performance and the stability of the system, we deposited a dichroic green filter, based on a 46 layer design of SiO_2 and Nb_2O_5, as shown in Figure 3.

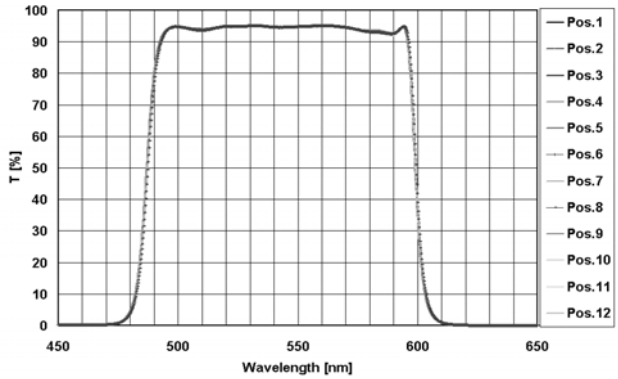

Figure 3: Dichroic green filter without backside AR.

All layers were purely time controlled. The rate during the deposition was kept constant by the lambda probe control loop. We measured transmittance values above 95% indicating very low losses. We further measured the wavelength position of the 50% transmittance point and achieved a full batch uniformity of better than ± 0.06% as shown in Figure 4.

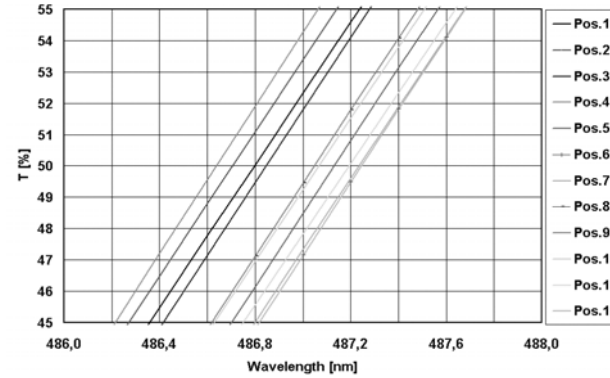

Figure 4: Full batch uniformity demonstrated with dichroic green filter.

For further investigations we deposited a simple 2-cavity band pass filter at 589nm (Figure 5). Controlled only by time, there is a slight deviation of the center wavelength position and a clear deviation of the shape, showing the limits of this control mode. However, using the OMS 4000 for optical monitoring, one receives a nearly perfect transmittance curve.

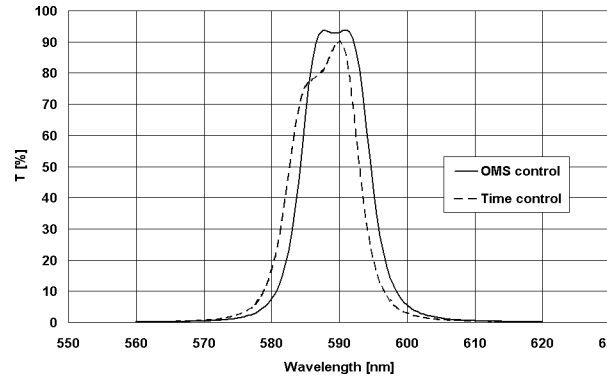

Figure 5: 2-cavity band pass filter (HL)^2 6H (LH)^2 L (HL)^2 6H (LH)^2 based on SiO_2 and Nb_2O_5.

For more demanding layer systems it is possible to combine the time control mode with the optical monitoring. We deposited a 5-cavity band pass filter and monitored all layers except the coupling layers at the design wavelength of 550nm. This is the same technique as applied in our DWDM machines [4]. The result in Figure 6 was the outcome of the first run to produce this filter, which highlights the possibility of rapid prototyping of even more demanding interference filters.

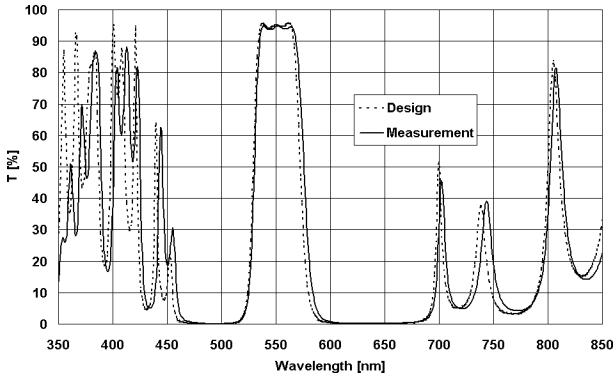

Figure 6: 5-cavity band pass filter based on SiO_2 and Nb_2O_5.

In order to demonstrate the run-to-run uniformity of the system, we carried out three successive wideband AR coating runs. The wideband AR coating is a 4 layer design based on SiO_2 and Nb_2O_5 with layer thicknesses between 12 and 110 nm. The excellent reproducibility of the combined control mode, time and optical monitoring, is shown in Figure 7.

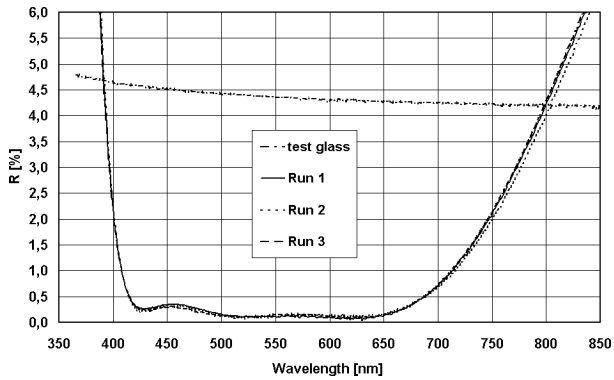

Figure 7: Run-to-run uniformity of a wideband AR coating.

Very demanding layer systems are thin film laser components especially for femtosecond pulse laser applications. In the fs regime it is essential to control the group velocity dispersion (GVD) of each optical element within the laser system. Femtosecond laser optics must be specially designed in order to control the phase characteristic of the optical system over the extremely wide bandwidth of fs lasers. Figure 8 shows the spectral transmittance of such a high reflecting "chirped" wideband mirror combined with a pump laser window at 532nm. The 65 layer design based on SiO_2 and Nb_2O_5 was made by the group of Professor Krausz from the Technical University of Vienna. The comparison of the theoretical spectrum with the measured spectrum of the deposited mirror shows an outstanding conformity.

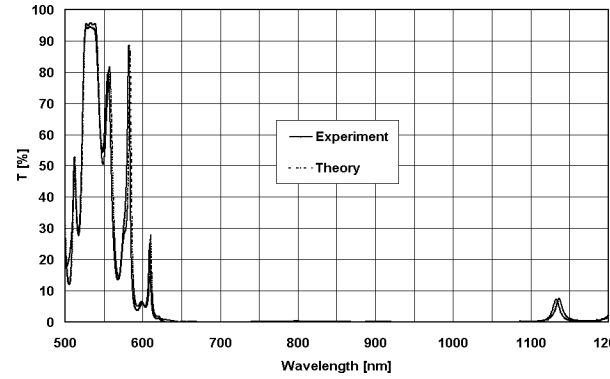

Figure 8: Spectral transmittance of a wideband GVD-mirror with pump laser window.

CONCLUSION

Plasma ion assisted reactive MF dual magnetron sputtering can produce high quality optical thin film layer systems stable and reproducible with a high throughput and a high yield. Direct on-substrate optical thickness control can significantly improve the performance and the time needed to set up new processes. The newly designed sputtering system permits us to deposit layers with excellent optical properties at outstanding high rates under fully automated conditions, including the substrate transfer from and to the sputtering chamber out of a cassette module.

REFERENCES

1. A. Zoeller, M. Boos, H. Hagedorn, W. Klug, and C. Schmitt, "High accurate in-situ optical thickness monitoring for multilayer coatings," 47th Annual Technical Conference Proceedings of the Society of Vacuum Coaters Technical Conference, AGP-2, 2004.

2. M. Scherer, J. Schmitt, R. Latz, and M. Schanz, "Reactive alternating current magnetron sputtering of dielectric layers," J. Vac. Sci. Technol., A 10(4), 1772, 1992.

3. J.M. Walls, D.R. Gibson, I. Brinkley, D.G. Teer, and J. Hampshire, "Closed field magnetron sputtering: a new strategy for multilayer optical coatings," 46th Annual Technical Conference Proceedings of the Society of Vacuum Coaters, 387, 2003.

4. H. Hagedorn, A. Lotz, P. Pecher, and O. Treichel, "Ultra narrow band pass filters produced by plasma ion assisted deposition," Optical Interference Coatings, OSA Technical Digest, WA4 -1, 2001.

High Power Pulsed Reactive Sputtering of Zirconium Oxide and Tantalum Oxide

D.A. Glocker and M.M. Romach, Isoflux Incorporated, Rochester, NY; and D.J. Christie and W.D. Sproul, Advanced Energy Industries, Fort Collins, CO

Key Words: Sputter deposition, Reactive sputtering, Dielectric coatings, High power pulsed magnetron sputtering

ABSTRACT

Zirconium oxide and tantalum oxide films were deposited in an inverted cylindrical magnetron cathode using high power pulsed sputtering. Average power densities were between 5 and 7 W/cm^2 and peak power densities were in the range of 0.5 kW/cm^2. In all of the experiments the oxygen was introduced using flow control, and the current and voltage waveforms of the HPPMS supply changed in a reproducible manner as the targets went from the metallic to the poisoned mode. Coatings were done with the targets in the poisoned mode and for both materials high index films were deposited with very little evidence of arcing. The maximum deposition rate achieved for zirconium oxide was 1.9 nm/min, while tantalum oxide was deposited at 18 nm/min. Comparisons are made with coatings deposited using mid frequency AC sputtering in the same system. The specific deposition rate for zirconium oxide made using the HPPMS power supply was 25% of that when using the AC power supply. In contrast, the specific deposition rates for tantalum oxide were very similar for the two power supplies. X-ray diffraction revealed that the zirconium oxide grew in the monoclinic phase.

INTRODUCTION

High power pulsed magnetron sputtering (HPPMS), which uses peak power densities on the order of kW/cm^2 with duty cycles of 1-2%, has emerged as a promising new technique for producing high levels of ionization in sputtering plasmas [1-5]. With the development of HPPMS power supplies that are capable of arc handling [6,7], titanium oxide and aluminum oxide have recently been deposited using this method [8,9].

There were two purposes for the work reported here. The first was to study the use of HPPMS in an inverted cylindrical magnetron cathode. Inverted cylindrical magnetrons produce unique geometrical confinement of the sputtering plasma. This provides an interesting comparison with previous HPPMS work, which has been done on planar and rotating magnetrons. The second purpose was to study the reactive deposition of zirconium oxide and tantalum oxide using HPPMS with this geometry. Both are high index materials that are important in applications ranging from optical devices to thermal barriers on turbine blades.

EXPERIMENT

The inverted cylindrical magnetron used in these experiments is shown in Figure 1 and has been described elsewhere [10].

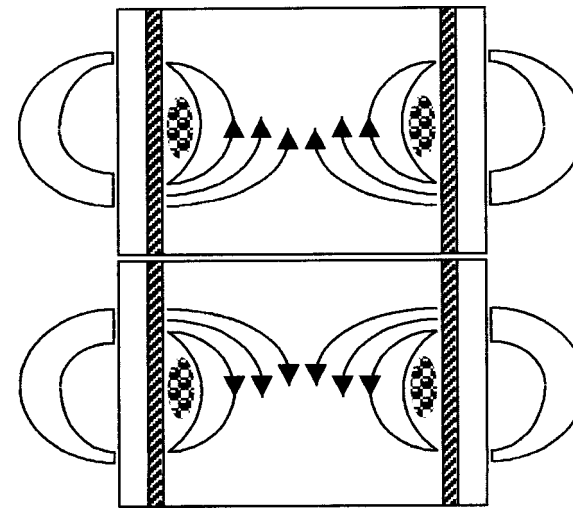

Figure 1: Geometry of the inverted cylindrical magnetron cathode used in these experiments.

Briefly, it consists of two independently driven coaxial cylindrical magnetrons, both of which can use either balanced or unbalanced magnets. Each magnetron is 19 cm in diameter by 10 cm high. The racetracks typically cover approximately one half of the target area, so the power densities we report are calculated assuming an eroded area of 300 cm^2 for each target.

When the HPPMS power supply was used, it was connected to only the top cathode. The peak powers were typically on the order of 0.5 kW/cm^2. The reported average powers were calculated using 1/2 CV^{2}f, where 1/2 CV^2 is the energy stored in the power supply capacitor bank on each pulse and f is the pulse frequency.

The coatings deposited using HPPMS were compared to those made by driving both cathodes simultaneously using 40 kHz AC power [11]. Optical emission spectroscopy is normally used to control the reactive gas flow in this system. However,

 505/856-7188 ISSN 0737-5921

47th Annual Technical Conference Proceedings (April 24–29, 2004) Dallas, TX USA

fluctuations in the plasma intensity prevented the use of optical emission control in the case of HPPMS. Therefore, all of the coatings reported here (both AC and HPPMS) were deposited with the oxygen introduced in flow control and the targets fully poisoned. This should result in a worst-case situation with respect to arcing.

Commercially pure (99.5%) zirconium and tantalum targets were used. The argon flow was 75 sccm for all of the experiments. The system is pumped with a turbomolecular pump and the pressure is maintained through downstream control using a pendulum gate valve.

In all of the experiments the substrates were located in the center of the upper racetrack. The reported deposition rates were calculated from thicknesses measured with an Alpha Step 250 profilometer on silicon wafers. A Gaertner L116B ellipsometer was used to determine the optical constants for coatings on silicon at a wavelength of 632.8 nm.

RESULTS AND DISCUSSION

Zirconium Oxide

Using the HPPMS power supply, the transition from the metallic to the poisoned mode of the target was easy to determine from the output voltage and current waveforms. Figure 2 shows the voltage, current, and power as functions of time for a single pulse with the zirconium target sputtering in the metallic mode. Figure 3 shows the same parameters with the zirconium target sputtering in the poisoned mode.

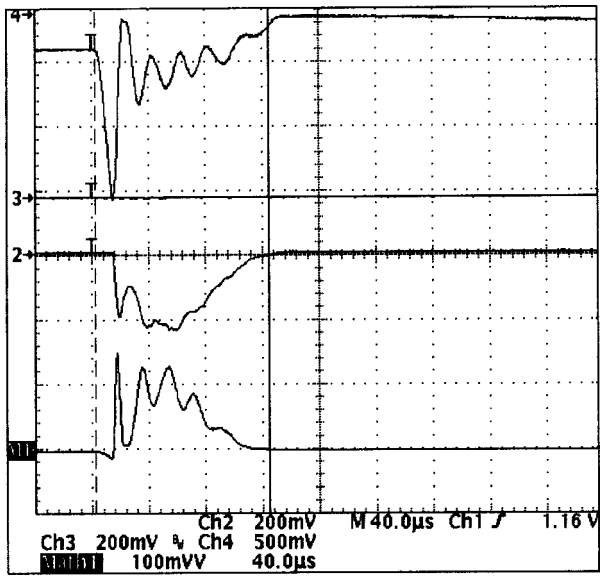

Figure 2: The voltage (channel 4, 500 V/div), current (channel 2, 200 A/div) and power (channel M1, 100 kW/div) as functions of time for a single pulse from the HPPMS power supply with the zirconium target in the metallic mode.

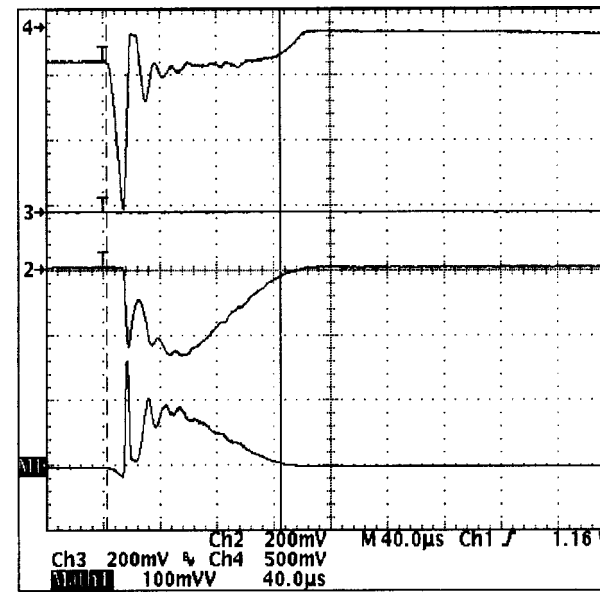

Figure 3: The voltage (channel 4, 500 V/div), current (channel 2, 200 A/div) and power (channel M1, 100 kW/div) as functions of time for a single pulse from the HPPMS power supply with the zirconium target in the poisoned mode.

These qualitative differences in the waveforms were very reproducible and proved to be a reliable indicator of the target condition. We also noticed that the magnitude of the initial large voltage spike (approximately 1400 V) did not change as the target poisoned, but the magnitude of the associated initial current spike did. We were able to use the value of this initial current to map out a hysteresis curve for the process and the results are shown in Figure 4.

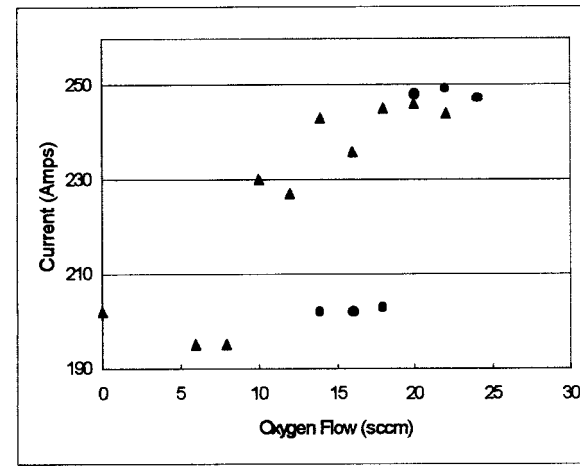

Figure 4: The magnitude of the initial current spike as a function of oxygen flow for increasing (circles) and decreasing (triangles) flows while sputtering zirconium oxide.

The data shown in Figure 4 were taken at an average power density of 8 W/cm^2, a peak power of 0.5 kW/cm^2, a pulse frequency of 400 Hz and a pressure of 5 mTorr. It is possible that these changes in current could provide a signal with which to control the reactive gas flow in an HPPMS process.

As the waveforms show, there was virtually no indication of arcing at any oxygen flow during the deposition of zirconium oxide. Furthermore, the racetrack was open with very few arc tracks after the deposition of high index films.

Table 1 summarizes the power density, deposition rate and optical constants for zirconium oxide coatings deposited using both HPPMS and AC sputtering. The total pressure during the HPPMS process was 3.1 mTorr and during the AC process it was 4.0 mTorr. In both cases the coating time was 100 minutes.

Table 1: Power density, deposition rate, and optical constants for zirconium oxide sputtered in the poisoned mode using both HPPMS and 40 kHz AC power.

Mode	Power Density (W/cm^2)	Rate (nm/min)	n	k
HPPMS	7.0	1.9	2.03	-.0002
40 kHz	4.3	4.7	2.26	-.0005

Even though the average power density for the HPPMS process was 60% greater than for the AC process, the deposition rate was only 40% that of the AC process. Normalizing the two processes to the same power density, the specific HPPMS rate is approximately 25% of the AC rate. This agrees very well with the relative rates for aluminum oxide and titanium oxide reported by others at this conference [8,9].

X-ray diffraction measurements determined that the zirconium oxide deposited using HPPMS grew in the monoclinic phase. This is typical of what is found in single layer sputtered zirconia films [12].

Tantalum Oxide

The waveforms for tantalum oxide sputtered in the metallic and poisoned modes by HPPMS also went through a transition very much like the one shown in Figures 2 and 3. There was also very little arcing or evidence of arc tracks on the target in the case of tantalum oxide sputtered over a range of conditions using HPPMS.

Table 2 summarizes the power density, deposition rate and optical constants for tantalum oxide coatings deposited using both HPPMS and AC sputtering. The total pressure during both processes was 5 mTorr. The HPPMS coating time was 20 minutes and the AC coating time was five minutes.

Table 2: Power density, deposition rate and optical constants for tantalum oxide sputtered in the poisoned mode using both HPPMS and 40 kHz AC power.

Mode	Power Density (W/cm^2)	Rate (nm/min)	n	k
HPPMS	4.8	17.9	2.11	-.002
40 kHz	4.8	16.8	2.17	-.0008

The striking result here is that with comparable power densities the deposition rates are also comparable for the two processes, unlike the case for other materials.

For the coatings reported in Table 2, the average power and oxygen flow for the HPPMS process were 1440 W and 50 sccm respectively and for the AC process they were 2875 W and 100 sccm. Measurements made on a number of films using both processes showed that the targets were fully poisoned under these conditions. Moreover, two cathodes were running at the indicated power density in proximity to the substrate in the AC case and only one in the HPPMS case. If anything, the additional material from the bottom cathode should have resulted in a thicker coating in the AC case than in the HPPMS case. An explanation for the similarity in rates for HPPMS and AC deposition of tantalum oxide is still open.

CONCLUSION

High power pulsed magnetron sputtering has been used to deposit zirconium oxide and tantalum oxide in an inverted cylindrical magnetron cathode. In both cases high index films were made with the targets in the poisoned mode with very little evidence of arcing. The specific deposition rate for zirconium oxide using the HPPMS power supply was approximately 25% of the rate when using a 40 kHz AC supply. In contrast, the specific deposition rate for tantalum oxide was very similar for the two supplies.

ACKNOWLEDGMENTS

The authors would like to thank Karen Peterson for the thickness and ellipsometer measurements and Vinnie Gupta for the X-ray diffraction results.

REFERENCES

1. V. Kouznetsov, K. Macák, J.M. Schneider, U. Helmersson, and I. Petrov, "A Novel Pulsed Magnetron Sputter Technique Utilizing Very High Target Power Densities," Surf. Coat. Technol., 122, 290, 1999.

2. K. Macák, V. Kouznetsov, J. Schneider, and U. Helmersson, "Ionized Sputter Deposition Using an Extremely High Plasma Density Pulsed Magnetron Discharge," J. Vac. Sci. Technol. A, 18, 1533, 2000.

3. A.P. Ehiasarian, R. New, W.-D. Munz, L. Hultman, U. Helmersson, and V. Kouznetsov, "Influence of High Power Densities on The Composition of Pulsed Magnetron Plasmas," Vacuum 65, 147, 2002.

4. A.P. Ehiasarian, W.-D. Munz, L. Hultman, U. Helmersson, and I. Petrov, "High Power Pulsed Magnetron Sputtered CrN Films," Surf. Coat. Technol., 163-164, 267, 2003.

5. B. DeKoven, R. Weiss, P. Ward, B. Kakimoto, C. Marion, J. Xie, D. Devir, D.J. Christie, W.D. Sproul, R.A. Scholl, and A. Anders, "Carbon Thin Film Deposition Using High Power Pulsed Magnetron Sputtering," 46th Annual Technical Conference Proceedings of the Society of Vacuum Coaters, San Francisco, CA, May 3-8, 2003, p. 158-165.

6. W.D. Sproul, D.J. Christie, D.C. Carter, F. Tomasel, and T. Linz, "Pulsed Plasmas for Sputtering Applications," Surface Engineering, 20, No. 3, 1, 2004.

7. D.J. Christie, W.D. Sproul, D.C. Carter, and F. Tomasel, "A Novel Pulsed Power Supply with Arc Handling and Leading Edge Control as Enabling Technology for High Power Pulsed Magnetron Sputtering (HPPMS)," 47th Annual Technical Conference Proceedings of the Society of Vacuum Coaters, Dallas, Texas, April 26-29, 2004.

8. J.A. Davis, W.D. Sproul, D.J. Christie, and M. Geisler, "High Power Pulse Reactive Sputtering of TiO_2," 47th Annual Technical Conference Proceedings of the Society of Vacuum Coaters, Dallas, Texas, April 26-29, 2004.

9. W.D. Sproul, D.J. Christie, and D.C. Carter, "The Reactive Sputter Deposition of Aluminum Oxide Coatings Using High Power Pulsed Magnetron Sputtering (HPPMS)," 47th Annual Technical Conference Proceedings of the Society of Vacuum Coaters, Dallas, Texas, April 26-29, 2004.

10. D.A. Glocker, M.M. Romach, and V.W. Lindberg, "Recent Developments in Inverted Cylindrical Magnetron Sputtering," Surf. Coat. Technol., 146-147 (2001), 457-462.

11. D.A. Glocker, V.W. Lindberg, and A. R. Woodard, "AC Reactive Sputtering with Inverted Cylindrical Mangetrons," 43rd Annual Technical Conference Proceedings of the Society of Vacuum Coaters, Denver, Colorado, April 15-20, 2000.

12. C.R. Aita, "Nanostructured Ceramic Coatings: Zirconia Single Layers and Nanolaminates," Processing and Fabrication of Advanced Ceramic Coatings, T.S. Srivatsan and J.J. Moore, ed., The Minerals, Metals & Materials Society, 1996.